

**Search for new physics in the mono-electron
channel with the CMS experiment in pp
collision data at $\sqrt{s} = 13$ TeV**

VON
VIKTOR KUTZNER

MASTERARBEIT IN PHYSIK

VORGELEGT
DER FAKULTÄT FÜR MATHEMATIK, INFORMATIK UND
NATURWISSENSCHAFTEN DER RWTH AACHEN

IM JUNI 2016

ANGEFERTIGT IM
III. PHYSIKALISCHEN INSTITUT A

BEI
PROF. DR. THOMAS HEBBEKER

ZWEITGUTACHTER
PROF. DR. CHRISTOPHER WIEBUSCH

Abstract

This thesis presents the search for new physics in the mono-electron channel using proton-proton collision data with a center-of-mass energy of $\sqrt{s} = 13$ TeV recorded at the LHC in 2015 by the CMS experiment. The recorded data is compared to the Standard Model prediction in the transverse mass distribution. The deviations between data and the Standard Model prediction are analyzed in terms of interpretations beyond the Standard Model. The interpretations include the production of a heavy W' vector boson and the production of dark matter through simplified models.

The data is interpreted as 95% CL exclusion limits. The production of a W' boson can be excluded for masses up to 3.75 TeV. Simplified models are used to model the dark matter production mechanism. The sensitivity of this study is presented in terms of excluded mediator masses M_{med} and dark matter masses m_{DM} for axial-vector, vector, scalar and pseudoscalar coupling mediator models.

The influence of the future High-Luminosity LHC upgrade on the dark matter search in the mono-electron channel is investigated, along with CMS detector upgrades. The increased sensitivity is evaluated for a simplified model with an axial-vector coupling mediator.

Zusammenfassung

Diese Arbeit beschreibt die Suche nach neuer Physik im Mono-Elektronkanal in Proton-Proton-Kollisionsdaten bei einer Schwerpunktsenergie von $\sqrt{s} = 13$ TeV, aufgezeichnet 2015 mit dem CMS-Experiment am LHC-Beschleuniger. Die Daten werden im transversalen Massenspektrum mit Standardmodell-Simulationen verglichen. Unterschiede zwischen Daten und Standardmodell-Simulation werden in Hinblick auf neue Physik interpretiert, wobei zum Einen die Produktion eines schweren W' -Vektorbosons und zum Anderen die Produktion von dunkler Materie in sogenannten *simplified models* berücksichtigt wurde.

Die Daten werden als 95%-CL-Ausschlussgrenzen interpretiert. Die Produktion eines W' -Vektorbosons kann im Mono-Elektronkanal bis zu einer Masse von 3.75 TeV ausgeschlossen werden. Für die Suche nach dunkler Materie werden obere Ausschlussgrenzen für die Modellparameter der Mediatormasse M_{med} und der Masse dunkler Materie m_{DM} bestimmt. Hierbei werden *simplified models* mit Axialvektor-, Vektor-, Skalar- und Pseudoskalarkopplung berücksichtigt.

Der Einfluss des geplanten High-Luminosity-LHC-Projektes auf die Suche nach dunkler Materie im Mono-Elektronkanal wird in einer Extrapolationsstudie untersucht, wobei auch Modernisierungen des CMS-Detektors berücksichtigt werden. Die Sensitivität der Suche nach dunkler Materie wird für ein *simplified model* mit Axialvektor-kopplung untersucht.

Contents

1	Introduction	1
2	Theory	3
2.1	The Standard Model	3
2.1.1	Elementary particles	3
2.1.2	Physics beyond the Standard model	4
2.2	The Sequential Standard Model	4
2.3	Dark matter	5
2.3.1	Astrophysical evidence	5
2.3.2	Particle candidates for dark matter	7
2.3.3	WIMP dark matter detection methods	8
2.4	Dark matter production in the mono-W channel	12
2.4.1	Effective field theory approach	12
2.4.2	Simplified models	14
2.4.3	Comparison of dark matter production mechanisms	18
2.4.4	Conclusion	22
3	The Compact Muon Solenoid	23
4	Simulation tools	27
4.1	Monte Carlo sample generation	27
4.1.1	Madgraph5 aMC@NLO	27
4.1.2	POWHEG BOX	28
4.1.3	Pythia	28
4.1.4	JHU generator	28
4.2	CMS detector simulation	28
4.2.1	GEANT4	28
4.2.2	DELPHES	29

CONTENTS

5	Search for new physics with LHC Run-2 at $\sqrt{s} = 13$ TeV	31
5.1	Analysis method	31
5.2	Data	31
5.3	Standard model background	32
5.3.1	Higher order corrections for the W Standard Model background	33
5.4	Physics objects	35
5.4.1	Electron	35
5.4.2	Missing transverse energy	37
5.5	Event selection	38
5.6	Pile-up reweighting	38
5.7	Multijet background estimation	38
5.8	Systematic uncertainties	40
5.9	Final M_T distribution	41
5.10	Limit determination	43
5.11	Sequential Standard Model W' interpretation	43
5.11.1	SSM W' signal generation	43
5.11.2	Exclusion limits	44
5.12	Dark matter interpretation	45
5.12.1	Dark matter signal generation	45
5.12.2	Selection of parameter sets for full detector simulation	47
5.12.3	Event reweighting	47
5.12.4	Reconstructed dark matter signals	48
5.12.5	Optimization strategies	48
5.12.6	Exclusion limits in the simplified model parameter space	49
5.12.7	Comparison with direct- and indirect-detection searches	55
5.13	Results	57
6	Impact of the High-Luminosity LHC and upgraded CMS detector on dark matter searches	59
6.1	The High-Luminosity LHC project	59
6.2	CMS detector upgrades	60
6.3	Simulation of Phase-II conditions	61
6.4	Dark matter exclusion limits	62
6.4.1	Effective field approach	62
6.4.2	Simplified models	62
6.4.3	Sensitivity to detector performance	65

6.4.4	Conclusion	65
7	Unitarity violation in quark interference models	67
8	Conclusion	69
9	Appendix	71
9.1	Event displays	71
9.2	DELPHES data cards	71
9.3	Impact of the HL-LHC on dark matter searches	73
10	References	75

CONTENTS

Chapter 1

Introduction

This thesis presents the search for new physics in the mono-electron channel using proton-proton collision data with a center-of-mass energy of $\sqrt{s} = 13$ TeV recorded at the Large Hadron Collider (LHC) in 2015 by the Compact Muon Solenoid (CMS) experiment. The Standard Model provides a consistent theoretical description of the discoveries in particle physics so far, however it cannot account for all observations and many open questions remain. The thesis provides a dedicated search for new physics beyond the Standard Model, in which a new vector boson and dark matter (DM) is investigated. While new vector bosons have been postulated in the Sequential Standard Model, the search for dark matter is motivated by the abundance of astrophysical evidence, which triggered the conception of diverse dark matter detection experiments.

Evidence for dark matter originates among others from the observation of galaxy rotation curves, which suggest the presence of a dark halo in order to explain the discrepancy of the measured rotational velocity dependent on the distance from the galaxy's center and the Keplerian prediction [1]. The Bullet cluster presents another hint for dark matter, as do fluctuations in cosmic radiation [2,3]. Cosmological determinations estimate the visible baryonic matter to encompass only $\Omega_b \approx 4.6\%$ of the overall energy distribution in the universe, with dark matter contributing by a much larger extent of $\Omega_{DM} \approx 22.4\%$ and dark energy by $\Omega_{DE} \approx 73\%$ [4]. This glaring lack of understanding of most of the universe's content drives the many different searches for dark matter, whose explanation lies beyond the Standard Model of particle physics.

The search for dark matter using particle collisions is non-intuitive at first, as the potentially produced dark matter is not expected to leave any trace in the detector, thus hindering any detection effort. Assuming dark matter to be of weakly interacting massive nature, it may however recoil against another "tagging" particle. Such imbalanced collider signatures with distinct particles and a large missing transverse energy are promising candidates for searches beyond the Standard Model. The search is performed by analyzing the transverse mass spectra in the respective search channels. While this thesis uses a leptonically decaying W boson as the tagging particle, other searches use among others a Z boson, one or several jets or one photon. Each search channel offers its own advantages, and exclusion limits on specific dark matter parameters can be refined by the combination of multiple channels.

This analysis continues the search for a Sequential Standard Model W' boson and dark

CHAPTER 1. INTRODUCTION

matter performed with data recorded by the CMS experiment until 2012 at a center-of-mass energy of up to $\sqrt{s} = 8$ TeV [5]. With the center-of-mass energy significantly increased in Run-2 of the LHC, new dark matter production mechanisms are considered, which introduce specific mediator particles between matter and dark matter within the framework of simplified models. This approach allows a more detailed study of the interaction compared to Run-1, in which the dark matter production has been studied in a model-independent effective field approach. However, this approach cannot be used once the mediating particle can potentially be produced directly as in Run-2. Collider searches in particular are sensitive to the mediating interaction of the dark matter production process compared to other dark matter searches, such as direct detection experiments.

The thesis is structured in five chapters. The theoretical aspects of the Standard Model as well as the Sequential Standard Model and dark matter are discussed, followed by an overview of the experimental setup and numerical simulation tools used in this study. The proton-proton collision data at $\sqrt{s} = 13$ TeV recorded by CMS are analyzed and interpreted in terms of a new vector boson and dark matter in Ch. 5. A study of the impact of the High-Luminosity LHC upgrade on the dark matter search is presented in Ch. 6.

Chapter 2

Theory

In this chapter the Standard Model is discussed and extensions for physics beyond the Standard Model are motivated. The considered extensions include a new vector boson described within the Sequential Standard Model, as well as dark matter. Different dark matter production mechanisms in the mono-electron channel with their respective parameter space are discussed.

2.1 The Standard Model

The Standard Model (SM) provides a comprehensive theory of elementary particles and their interactions between each other. The underlying local gauge symmetries are $SU(3)$ for quantum chromodynamics and $SU(2) \times U(1)$ for the unified electroweak interaction, which define the Standard Model in terms of particles and the interacting forces. The elementary particles are grouped into quarks, leptons and gauge bosons, of which the gauge bosons act as force carriers. The discovery of the Higgs gauge boson, which has been postulated within the framework, further confirmed the Standard Model. Fig. 2.1 shows the elementary particles described by the Standard Model.

2.1.1 Elementary particles

Quarks and leptons are fermionic particles with a spin of $\frac{1}{2}$ and are grouped in three *generations*, with increasing particle masses for each generation excluding lepton neutrinos. The three generations of charged leptons are comprised of the electron, muon and tau lepton, differing only in their respective mass. Each lepton generation is accompanied by a nearly massless lepton neutrino with zero charge. Considering quarks, each single generation is comprised of two quarks with either electric charge $q = +\frac{2}{3}e$ (the *up, charm and top* quarks) and $q = -\frac{1}{3}e$ (the *down, strange and bottom* antiquarks). Quarks have a color charge of *red, green and blue*, while antiquarks have an anticolor charge.

Forces are mediated through spin-1 gauge boson exchange. While the photon, Z and W bosons are carriers of the electroweak force, the gluon is the carrier of the strong force.

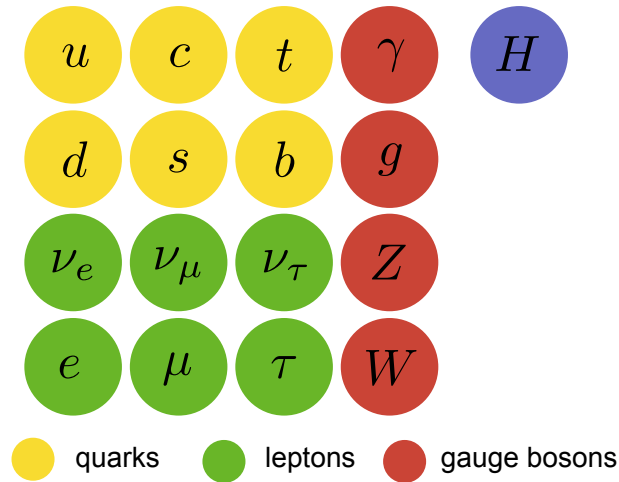


Figure 2.1: Elementary particles described by the Standard Model. Shown are the three families of quarks and leptons as well as the gauge and Higgs bosons.

Force carriers can be electrically charged in the case of W^\pm bosons, color charged in the case of the gluon or carry no charge of any kind, as in the case of the photon.

2.1.2 Physics beyond the Standard model

The Standard Model is able to provide a consistent theoretical description of the discoveries in particle physics up to this point, but many questions remain unanswered. The fundamental force of gravitation is not included in the model and it thus cannot address the hierarchy problem, which refers to the large discrepancy of the electroweak and gravitational energy scales. The lack of unification of the interactions for large energies poses another unsolved problem, as does the origin of the number of the fermion families. Astrophysical observations indicating the presence of dark matter can also not be explained within the Standard Model.

Many different extensions to the Standard Model have been proposed, of which two specific extensions - a new vector boson and dark matter - will be explored in this thesis.

2.2 The Sequential Standard Model

A possible extension to the Standard Model is a new heavy vector boson, such as a heavy analogue of the W boson referred to as a W' boson. Such a boson has been proposed in the Sequential Standard Model (SSM) among other additional heavy gauge bosons, such as a Z' boson [6]. It is of special interest, as its presence could help to address the gauge coupling unification problem. The mono-electron channel used in this analysis is predestined to include the search for a W' boson in the scope of new physics.

A Feynman diagram depicting the W' production is shown in Fig. 2.2. The proposed

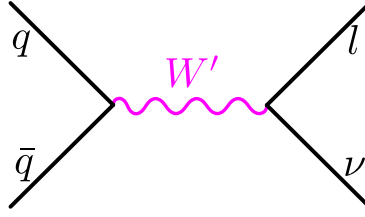


Figure 2.2: Feynman diagram showing the production of a Sequential Standard Model W' boson with leptonic decay.

W' boson has similar decay modes and branching fractions as the Standard Model W boson. An additional decay channel is $W' \rightarrow t\bar{b}$, which becomes available above $m_{W'} > 180$ GeV [5]. Considering the leptonic decay $W' \rightarrow l\nu_l$ with $l = e, \mu$, the branching ratio is $\approx 8.5\%$. A vector-axial vector coupling (V-A) of the W' boson is considered, in which the interaction couples equally to left-handed fermions and right-handed antifermions. The decay $W' \rightarrow WZ$ is beyond the scope of this analysis and a branching ratio of zero is assumed. It is considered in a separate analysis [7,8].

2.3 Dark matter

In this section, dark matter is motivated through astrophysical observations and cosmological arguments. A suitable candidate for a dark matter particle is considered and different detection methods will be discussed. The following discussion is based on [4] and [9].

2.3.1 Astrophysical evidence

Astrophysical observations indicate the presence of non-luminous and non-absorbing dark matter in the universe. Measurements of galaxy rotation curves yield too large values for the rotational velocity, which for a stable Keplerian orbit is given by

$$v(r) = \sqrt{\frac{G \cdot m(r)}{r}} \quad (2.3.1)$$

with the gravitational constant G . At large distances from the galactic center the velocity of luminous objects is expected to decrease with $v(r) \propto \sqrt{1/r}$. Measurements as shown in Fig. 2.3-left however yield approximately constant velocities for the most distant galactic objects, indicating the presence of a dark halo. The measurements give a lower bound on the DM density of at least $\Omega_{DM} \gtrsim 0.1$.

Dark matter is expected to only interact weakly, as indicated by the bullet cluster¹ collision with another cluster. While the hot gas clouds containing most of the baryonic matter interacted and subsequently increased in temperature and decelerated, gravitational lensing showed that the majority of the total mass continued to move on its original trajectory [2].

¹cluster 1E0657-558

The cosmic microwave background radiation indicates very small density perturbations of 0.1% at large redshift values $z \approx 1300$. Observations of very old galaxies with a redshift of $z \approx 10$ therefore indicate the presence of dark matter as well, as dark matter would allow the formation of galaxies from density perturbations at an earlier time in the matter-dominated universe.

Massive compact halo objects causing gravitational microlensing may contribute to baryonic dark matter. However, the low number of such identified objects and further results from big bang nucleosynthesis and the cosmic microwave background radiation disfavor the assumption of baryonic dark matter [4].

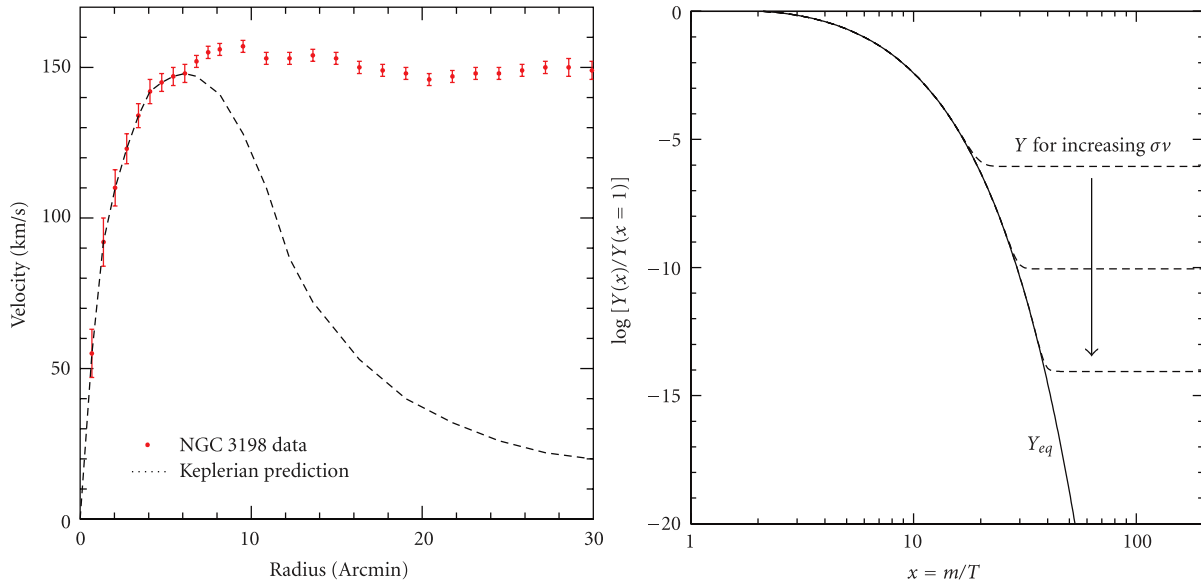


Figure 2.3: Left: Rotation velocity of luminous objects from galaxy NGC 3198 depending on the radius compared to the Keplerian prediction. The measured data indicates an approximately constant velocity for large radii, indicating the presence of a *dark halo*. Right: Relative WIMP abundance $Y(x)/Y(x = 1 m/T)$ in the early universe depending on the inverse temperature showing the WIMP freeze-out for an increasing WIMP-SM annihilation rate $\sigma \times v$, with the annihilation cross section σ , WIMP velocity v and WIMP mass m . Figure from [4].

The observation of anisotropies in the cosmic microwave background radiation measured by the Planck satellite allows the determination of the thermal relic density of cold, non-baryonic matter. It is determined from global fits of cosmological parameters to multiple observations, also including the spatial distribution of galaxies [9, 10]:

$$\Omega_{\text{nbm}} h^2 = 0.1186 \pm 0.0020 \quad (2.3.2)$$

Here, h denotes the reduced Hubble constant $h = H/100 \text{ km sec}^{-1} \text{ Mpc}^{-1}$. The resulting density is significantly larger than the baryonic matter density $\Omega_{\text{b}} h^2$ alone,

$$\Omega_{\text{b}} h^2 = 0.02226 \pm 0.00023, \quad (2.3.3)$$

which is a fraction of $\approx 19\%$ of the cold, non-baryonic matter density. The baryonic matter density is determined by the ratio of deuterium and ${}^4\text{He}$, in which the deuterium is mainly produced through the big bang nucleosynthesis.

2.3.2 Particle candidates for dark matter

A viable candidate for non-baryonic dark matter is required to be stable, weakly-interacting and has to account for the right relic density $\Omega_{\text{nbm}}h^2$. These requirements are met by primordial black holes, axions, sterile neutrinos and weakly interacting massive particles (WIMPs), which are investigated in dedicated searches [9].

The most promising candidate for collider searches is electrically neutral WIMP dark matter χ , which is expected to have a mass in the range of 10 GeV and $\mathcal{O}(\text{TeV})$ [9]. The consideration of WIMPs in the ΛCDM^2 model yields the correct relic density $\Omega_{\text{nbm}}h^2$. A thermal and chemical equilibrium of WIMPs and SM particles is assumed after inflation in the early universe. At decreased temperatures $T < m_{DM}$ the WIMP density is exponentially suppressed as indicated as a solid line in Fig. 2.3-right. Here, the relative WIMP abundance depending on the inverse temperature is shown, in which the abundance corresponds to the relic density. The rate of annihilation between WIMPs and SM particles is given by the cross section multiplied by the WIMP velocity. Once the annihilation rate is below the Hubble expansion rate of the universe, the WIMPs leave the equilibrium, which is referred to as "freeze-out" [9]. The resulting constant relative abundance for increasing rates of annihilation is visible in Fig. 2.3-right as dashed lines. Larger annihilation rates lead to a smaller relic density. In the case of WIMPs, the corresponding cross section is in the order of the electroweak scale $\mathcal{O}(\text{pb})$.

The Standard Model does not provide a viable WIMP candidate, even though the neutrino interacts weakly and is electrically neutral. Measurements by the Planck satellite constrain the neutrino mass to $m_\nu < 0.23\text{ eV}$, which can only account for a cosmological density of $\Omega_\nu h^2 < 0.0072$ [4, 10].

A possible extension to the Standard Model is supersymmetry (SUSY), which introduces an additional symmetry between fermions and bosons. In the Standard Model, the spin of a given particle remains constant and cannot be changed, as stated by the Coleman-Mandula theorem. In SUSY models, fermions (bosons) are associated with a boson (fermion) superpartner [4], which has either spin $\frac{1}{2}$ for fermions or spin 1 for bosons. Fig. 2.4 shows the additional considered particles including squarks and sleptons, the superpartners to quarks and leptons, as well as the superpartners to the gauge bosons. The model introduces a WIMP candidate, the lightest supersymmetric partner (LSP). It is required to have exact R-parity of -1, which is defined by

$$R = (-1)^{3B+L+2S} \quad (2.3.4)$$

with the baryon number B , lepton number L and spin S . Exact R-parity infers the conservation of lepton and baryon numbers, which may be violated in SUSY models. It thus ensures the stability of the LSP. In SUSY models, the LSP is the lightest neutralino, which is a massive particle and a superposition of the neutral superpartners of the Higgs and electroweak gauge bosons [9].

² Λ cold dark matter model

WIMP dark matter is therefore well motivated and different detection methods will be discussed in the following section.

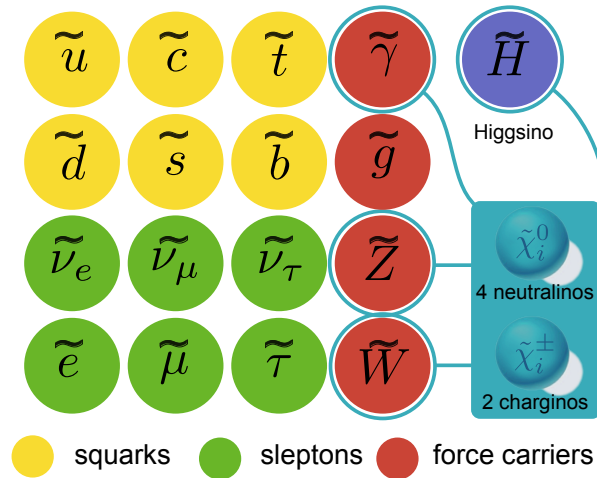


Figure 2.4: The supersymmetric extension of the Standard Model (SUSY). SM fermions (bosons) are associated with a bosonic (fermionic) superpartner shown in the figure. The superposition of the neutral superpartners of the Higgs and gauge bosons yields four additional neutralinos $\tilde{\chi}_i^0$ and two charginos $\tilde{\chi}_i^\pm$.

2.3.3 WIMP dark matter detection methods

WIMP dark matter may be detected via different detection schemes, for which Fig. 2.5 shows the principle interactions. The annihilation of SM particles to dark matter is studied with collider searches. In this case, further initial state radiation is required in order to tag the event in which dark matter may be produced. Indirect detection searches are sensitive to dark matter annihilation signatures involving SM particles. In direct-detection experiments, dark matter recoils off detector nuclei. This interaction can either be spin-dependent or spin-independent. Results obtained in this analysis will be compared to direct- and indirect-detection searches. The detection principles of the relevant experiments will be discussed in the following.

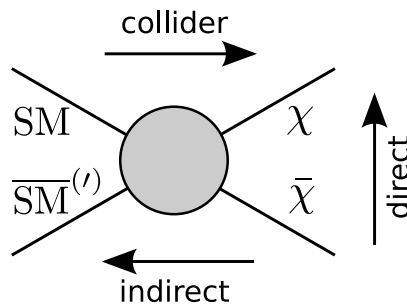


Figure 2.5: Dark matter detection schemes. DM may be detected using either SM or DM annihilation processes or in direct-detection searches, in which the DM recoils off detector nuclei.

Direct-detection searches

WIMPs are expected to interact with target nuclei through elastic scattering, following the assumption that WIMPs are gravitationally trapped inside galaxies with non-relativistic velocities in order to account for the observed rotational curves. Measured nuclear recoil energies range from $\mathcal{O}(10\text{eV})$ to $\mathcal{O}(100\text{keV})$, which corresponds to WIMP masses of $\mathcal{O}(1\text{ GeV})$ up to $\mathcal{O}(10\text{ TeV})$. WIMPs are expected to show an exponential spectrum, which is determined by the convolution of the WIMP velocity distribution and the angular scattering distribution. The differential recoil spectrum is given by [11]:

$$\frac{dR}{dE}(E, t) = \frac{\rho_0}{m_{DM}m_n} \cdot \int v \cdot f(v, t) \frac{d\sigma}{dE}(E, v) d^3v \quad (2.3.5)$$

Here ρ_0 indicates the local DM density, m_n the mass of the target nucleus, v the WIMP velocity and $\frac{d\sigma}{dE}(E, v)$ the differential scattering cross section. The time-dependent velocity distribution $f(v, t)$ accounts for the change in WIMP velocity revolution of the earth around the sun. The differential recoil spectrum can be approximated by [11, 12]

$$\frac{dR}{dE}(E) \approx \left(\frac{dR}{dE}\right)_0 F^2(E) \exp\left(-\frac{E}{E_c}\right), \quad (2.3.6)$$

in which $\left(\frac{dR}{dE}\right)_0$ is the background event rate and E_c denotes the characteristic energy scale depending on m_{DM} and m_n . $F^2(E)$ is a form-factor correction depending on spin-dependent or spin-independent nuclear interactions, in which direct-detection experiments are subdivided and probe different coupling mechanisms [11]. Vector and scalar dark matter would lead to spin-independent interactions, for which the cross section is proportional to the square of the mass of the nucleus. Axial-vector dark matter on the other hand would lead to spin-dependent interactions, which yield separate bounds for the DM-proton and DM-neutron interaction cross sections. As the expected interaction rate is at most one event per day and kilogram of detector material, direct-detection experiments require intense efforts to suppress background contributions [9].

Considering spin-independent interactions, the most sensitive experiments are dual-phase Xenon experiments, which include the LUX³ dark matter experiment as well as XENON1T⁴. Here, two types of detection are used to increase sensitivity and to reduce background contribution. Nuclear interactions in the Xenon target generate scintillating light which is detected by photomultiplier tubes. A strong electric field further allows the detector to be used as a time-projection chamber, which detects free electrons from the nuclear interaction. The electrons drift to the surface of the liquid Xenon and are extracted with an anode, producing a signal [13].

For lower WIMP masses below $m_{DM} < 10\text{ GeV}$ the SuperCDMS⁵ and CRESST-II⁶ experiments are most sensitive [14]. The CDMS experiment detects phonons produced

³Large Underground Xenon dark matter experiment

⁴predecessor: XENON100

⁵Cryogenic Dark Matter Search

⁶Cryogenic Rare Event Search with Superconducting Thermometers

by the interactions with a cryogenic Germanium detector operated at low temperatures of $\mathcal{O}(10\text{mK})$ and at a high bias voltage [15]. In CRESST-II, a scintillating CaWO_4 crystal is used, allowing the detection of both scintillating light and phonons due to the temperature increase followed by a nuclear interaction [16].

The PICO-2L experiment at SNOLAB⁷ uses a two-litre bubble chamber filled with a superheated liquid C_3F_8 . Charged particles deposit energy through ionization, which creates the characteristic track signatures. The PICO experiment offers a good electron-recoil and alpha decay rejection. It provides the most stringent constraints on the spin-dependent DM-proton scattering cross section in the lower mass range of $m_{DM} < 50$ GeV [14]. For spin-independent interactions, the LUX experiments currently provides the best constraints.

A hard limitation for direction-insensitive direct detection experiments are neutrinos from astrophysical sources, commonly referred to as the neutrino background. The astrophysical sources include solar, atmospheric, and diffuse supernova neutrinos and may produce the same signature as a WIMP signal. Collider searches on the other hand may potentially probe beyond the neutrino background.

Indirect detection searches

Indirect dark matter searches are sensitive to WIMP annihilation products such as high-energy neutrinos of the order $\mathcal{O}(\text{GeV})$, gamma rays, positrons, antiprotons and antinuclei [9, 17]. Experiments such as Super-Kamiokande, IceCube and AMANDA⁸ are sensitive to a possible signal coming from the sun or from the center of the earth, as the WIMP density and thus the annihilation probability is potentially increased for WIMPs that are slowed down by massive objects. The experiments include large arrays of photomultipliers to detect a possible WIMP annihilation signal. Other experiments such as the H.E.S.S. Cherenkov telescope and Fermi-LAT probe the strong TeV point source at the center of the galaxy, which is expected to contain a high dark matter density. The PAMELA and AMS satellites as well as the BESS polar balloon mission are sensitive to antiparticles, which may originate from WIMP annihilations. Differences in the high-energy positron and electron fluxes are measured by the PAMELA and AMS02 experiments, which showed a rise of the positron fraction between 10 and 200 GeV [9]. Cross section bounds are determined depending on the WIMP mass m_{DM} . Lower bounds on the cross section competitive to direct-detection searches are derived from annihilation signals coming from the direction of the sun, which are spin-dependent bounds on the DM-proton cross section. In this case, the Super-Kamiokande using $\chi\chi \rightarrow b\bar{b}$ and Ice-Cube experiments using $\chi\chi \rightarrow t\bar{t}$ yield the lowest bounds depending on the mass range of m_{DM} .

Fig. 2.6 shows the best current bounds on the DM-nucleon cross section for spin-independent and on the DM-proton cross section for spin-dependent interactions. The CDMS and CRESST-II experiments in particular provide bounds for light $m_{DM} \lesssim 5$ GeV in the case of spin-independent interactions. This region is below the threshold

⁷Sudbury Neutrino Observatory Laboratory. The PICO collaboration is the merger of the PICASSO and COUPP groups.

⁸Antarctic Muon And Neutrino Detector Array

for spin-dependent searches as indicated in Fig. 2.6-right. Collider searches are suitable to probe for light dark matter, thus providing complementary results.

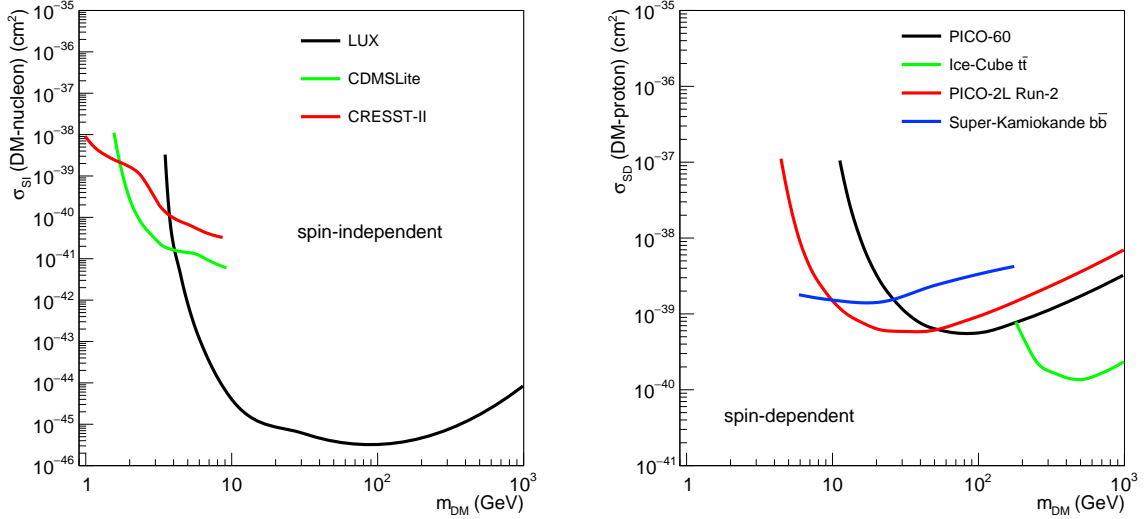


Figure 2.6: Best current bounds on the DM-nucleon cross section for direct and indirect dark matter detection experiments depending on m_{DM} . The spin-independent DM-nucleon cross section limit is shown on the left for the direct detection experiments LUX, CDMSLite and CRESST-II. Shown on the right is the spin-dependent DM-proton cross section limit for the direct detection experiment PICO and indirect detection experiments Ice-Cube and Super-Kamiokande. Figure adapted from [18].

Collider searches

In collider searches, the annihilation of SM particles into a pair of dark matter does not leave a detectable signal. Therefore, an additional component of initial state radiation X is required:

$$pp \rightarrow \chi\bar{\chi} + X \quad (2.3.7)$$

Subsequent mono- X searches are characterized by their respective signature, which include among others mono-jet, mono- γ , mono- Z or mono- W searches. The most recent bounds on dark matter production in colliders have been published by the CMS and ATLAS collaboration using $\sqrt{s} = 7$ TeV and $\sqrt{s} = 8$ TeV, with first results using $\sqrt{s} = 13$ TeV becoming available as well [5].

This analysis uses LHC proton-proton collision data to search for dark matter. The aspects of the dark matter production in the mono- W channel are presented in the following chapter.

2.4 Dark matter production in the mono-W channel

In the following, possible dark matter hadron collider production mechanisms are discussed with special emphasis on the distinctive mono-W channel features. The dark matter search in the mono-W channel, in which the W boson decays leptonically, offers several characteristic advantages. The single-lepton signature is a very clean signature, especially when considering electrons and muons as lepton candidates. The leading Standard Model background is well known and consists of W decays. Other Standard Model background contributions include $t\bar{t}$ and single-top production, Drell-Yan as well as Diboson processes. The SM backgrounds will be discussed in Ch. 5. Another advantage is the ability to study the effect of quark interference, which potentially enhances the production cross section and thus improves the sensitivity of the search. During the writing of this thesis, consecutive publications showed that the enhancement in cross section is due to an unitarity-violating production of longitudinal W bosons [19,20,21]. The implications for this search will be discussed in Ch. 7.

The production of dark matter can either be modelled by an abstract model-independent effective field approach or by more detailed model descriptions, which are referred to as simplified models. Simplified models introduce a new particle which mediates the interactions between Standard Model particles and dark matter. While the effective field approach was used in Run-1 at $\sqrt{s} = 8$ TeV, the transition to simplified models in Run-2 at $\sqrt{s} = 13$ TeV is motivated and discussed.

In the following, dark matter is assumed to be a weakly-interacting massive particle χ as motivated in Ch. 2.3.2. Depending on the coupling mechanism, both Dirac and Majorana dark matter are considered.

2.4.1 Effective field theory approach

The dark matter production can be modelled using an effective field theory (EFT) approach, which is motivated by direct-detection searches [22,23]. In this case, constraints are set on the contact interaction scale Λ . Contact interactions of energy scales $E < \Lambda$ are considered in this description while higher energies $E > \Lambda$ are integrated out of the Lagrangian. This approach therefore provides a model-unspecific description of the underlying production mechanism and has been used in the mono-W channel DM interpretation in Run-1 at a center-of-mass energy of $\sqrt{s} = 8$ TeV [5].

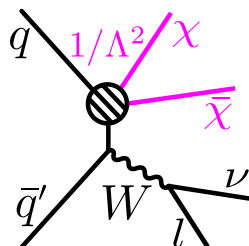


Figure 2.7: Feynman diagram showing the DM production in the mono-W channel. An effective field approach is used to model the DM production, which is motivated by direct-detection searches.

Fig. 2.7 shows the Feynman diagram of the DM production encapsulated in the EFT

2.4. DARK MATTER PRODUCTION IN THE MONO-W CHANNEL

approach in the mono-W channel, in which the W boson decays leptonically. The complete parameter space is given by the interaction scale Λ and the DM mass m_{DM} .

Coupling types

The considered couplings of the DM production mechanism to the SM particles in the EFT approach are axial-vector and vector coupling, for which the dominant production mechanism is quark-antiquark annihilation at tree level [24]. In the previous $\sqrt{s} = 8$ TeV analysis this choice of coupling was motivated in order to compare the results to direct-detection experiments, in which axial-vector (vector) coupling corresponds to spin-(in)dependent DM-nucleon interactions [5]. The effective operators in the Lagrangian for both coupling types are

$$\begin{aligned} \text{vector coupling:} \quad & \mathcal{L} \supset \frac{1}{\Lambda^2} (\bar{\chi} \gamma^\mu \chi) (\bar{q} \gamma_\mu q) \\ \text{axial-vector coupling:} \quad & \mathcal{L} \supset \frac{1}{\Lambda^2} (\bar{\chi} \gamma^\mu \gamma^5 \chi) (\bar{q} \gamma_\mu \gamma^5 q). \end{aligned}$$

Investigating axial-vector coupling in particular is of heightened interest as the interaction is non-zero for Majorana-type dark matter like neutralinos in SUSY. In the case of vector coupling, the interaction vanishes [25].

Quark interference

The DM production mechanism may potentially couple differently to the quarks depending on family, specifically to up- and down-type quarks. For the mono-W channel, the interference effect was first motivated by [26] and has been considered in the DM interpretation of Run-1 [5]. Fig. 2.8 shows the contributing Feynman diagrams leading to the interference effect. A new parameter λ_i is used to describe the potentially different coupling strength for each quark flavour [5], which additionally enters the effective Lagrangian operator.

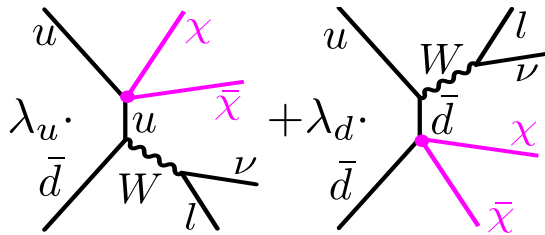


Figure 2.8: Feynman diagrams with the same initial and final state showing the effect of quark interference in the mono-W channel. The DM production mechanism may couple differently to the SM quarks as indicated by the coupling strength λ_i .

Considering up- and down-type quarks, a parameter ζ is introduced to describe the relative coupling strength to down-type quarks relative to up-type quarks [26]:

$$\zeta = \lambda_u \lambda_d \quad (2.4.1)$$

The parameter ξ is interpreted in terms of destructive ($\xi = +1$) or constructive ($\xi = -1$) interference and is included in the Lagrangian as follows:

$$\begin{aligned} \text{vector coupling:} \quad & \mathcal{L} \supset \frac{1}{\Lambda^2} (\bar{\chi} \gamma^\mu \chi) (\bar{u} \gamma_\mu u + \xi \bar{d} \gamma_\mu d) \\ \text{axial-vector coupling:} \quad & \mathcal{L} \supset \frac{1}{\Lambda^2} (\bar{\chi} \gamma^\mu \gamma^5 \chi) (\bar{u} \gamma_\mu \gamma^5 u + \xi \bar{d} \gamma_\mu \gamma^5 d). \end{aligned}$$

As shown by [26], the production cross section is increased for constructive interference ($\xi = -1$) compared to $\xi = 0, +1$. Constructive interference thus would have the ability to greatly contribute to the sensitivity of the mono-W channel, putting this final state in a competitive position to other DM searches such as the CMS monojet search.

Limitations of the EFT approach

Some considerations have to be taken into account to ensure the validity of the EFT approach. The exact nature of the underlying event remains hidden and may potentially involve a resonance decaying into dark matter, which can be interpreted as a mediating particle of mass M_{med} . Regarding such an interpretation, the EFT approach is only valid if the mediating particle is much heavier than the typical energy transfer, as the interaction is otherwise resolved and a UV complete theory is required. Ranges for M_{med} in which the approach remains valid will be quantified in Ch. 2.4.3. Furthermore, in order for the effective field theory to be perturbative,

$$\Lambda > \frac{m_{DM}}{2\pi} \quad (2.4.2)$$

has to be satisfied [5].

2.4.2 Simplified models

At high center-of-mass energies of $\sqrt{s} = 13$ TeV, the mediator may be produced on-shell. In this case, the effective field approach fails to describe the full event kinematics. In contrast, simplified models provide a UV-complete theory which give a more accurate description and address the limitations of the EFT approach described above. In simplified models, the interaction is resolved with the introduction of a mediating particle with mass M_{med} . Following [25], a massive spin-one vector boson from a broken $U(1)'$ gauge symmetry is considered for the mediator in the s-channel. For (axial-)vector coupling mediators, this consideration is comparable to a Z' -like particle and is described in the following Lagrangian [18]:

$$\mathcal{L}_{\text{vector}} = -g_{DM} Z'_\mu \bar{\chi} \gamma^\mu \chi - g_{SM} \sum_{q=u,d,s,c,b,t} Z'_\mu \bar{q} \gamma^\mu q \quad (2.4.3)$$

$$\mathcal{L}_{\text{axial-vector}} = -g_{DM} Z'_\mu \bar{\chi} \gamma^\mu \gamma^5 \chi - g_{SM} \sum_{q=u,d,s,c,b,t} Z'_\mu \bar{q} \gamma^\mu \gamma^5 q \quad (2.4.4)$$

The introduction of a single coupling to all quark flavours g_{SM} ensures that the considered model is minimal flavour violating, thus avoiding existing constraints from quark flavour physics [18].

2.4. DARK MATTER PRODUCTION IN THE MONO-W CHANNEL

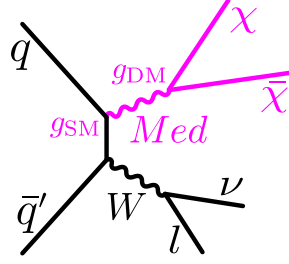


Figure 2.9: Feynman diagram showing the dark matter production through the exchange of an axial-vector or vector coupling mediator particle described in a simplified model, along with the associated production of a leptonically decaying W boson.

Fig. 2.9 shows the modified Feynman diagram in the mono-W channel. With the inclusion of different mediator coupling strengths to both Standard Model particles g_{SM} and dark matter particles g_{DM} , the now extended parameter space becomes as follows:

$$\frac{M_{\text{med}}}{g_{SM}} \mid \frac{m_{DM}}{g_{DM}}$$

In contrast to the EFT approach, the four-dimensional parameter space requires the results to be presented in two-dimensional planes. As discussed in Sec. 2.4.1, the underlying interaction hidden by the effective field approach may be of particle-like nature involving a mediator. The relation between the EFT approach and simplified models is given by [25]

$$\Lambda_{\text{EFT}} = \frac{M_{\text{med}}}{\sqrt{g_{SM}g_{DM}}}. \quad (2.4.5)$$

Non-s-channel production

In addition to the previously introduced coupling types in Sec. 2.4.1, simplified models present an opportunity to study further coupling types, such as scalar and pseudoscalar coupling. A possible associated model involves a pair of quarks annihilating into an excited W boson, which consecutively decays into a leptonically decaying W boson and a spin-zero mediating particle. The mediator in turn decays to a pair of dark matter. The respective effective operators depending on the coupling entering the Lagrangian are

$$\begin{aligned} \text{scalar coupling:} \quad \mathcal{L} &\supset -\frac{1}{2}M_{\text{med}}^2 S^2 - g_{DM} S \bar{\chi} \chi \\ \text{pseudoscalar coupling:} \quad \mathcal{L} &\supset -\frac{1}{2}M_{\text{med}}^2 P^2 - g_{DM} P \bar{\chi} \gamma^5 \chi. \end{aligned}$$

Fig. 2.10 shows a Feynman diagram of the considered simplified model using a scalar and pseudoscalar mediator. The inclusion of a pseudoscalar mediator as shown in Fig. 2.10 however violates gauge unitarity as a pseudoscalar mediator has zero coupling to a pair of vector bosons at tree level. The theoretical model therefore is not renormalizable [27]. In order to conserve gauge invariance, the pseudoscalar mediator has to be

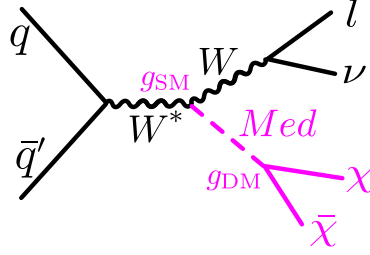


Figure 2.10: Feynman diagram showing the dark matter production through the exchange of a scalar and pseudo-scalar coupling mediator particle described in a simplified model, along with the associated production of a leptonically decaying W boson.

produced in fermionic loop corrections with CP-violating couplings to the W bosons, which would suppress this particular process. In this thesis, the analysis of a hypothetical pseudoscalar mediator with anomalous coupling to the W bosons is considered in order to probe a CP-violating DM production extension to the SM.

Mediator width

To avoid the stringent LHC bounds from di-lepton searches, the mediator couplings to leptons are set to zero [18]. In the following, the considered choices for the mediator decay width are motivated. The sensitivity of the analysis is greatly increased with a narrow decay width Γ_{med} of the mediator, as the process cross section is inversely proportional to Γ_{med} :

$$\sigma(pp \rightarrow \chi\bar{\chi} + X) \propto \frac{g_{SM}^2 g_{DM}^2}{(q^2 - M_{\text{med}}^2) + \Gamma_{\text{med}}^2/4} \hat{s} \quad (2.4.6)$$

Here \hat{s} denotes the partonic center-of-mass energy and q the momentum exchange in which the mediator is involved [28]. Narrow mediator widths lead to an enhancement of the production cross section, thus lower bounds for a narrow mediator width are investigated, as well as upper bounds for a broad mediator width.

For axial-vector and vector coupling the mediator decay width depends on the partial width of the mediator decay to DM and the mediator decay to the considered quarks as defined by [24]:

$$\Gamma_{\text{med}}^{V,A} = \Gamma_{\chi\bar{\chi}}^{V,A} + \sum_{i=1}^{N_f} N_c \Gamma_{q_i\bar{q}_i}^{V,A}. \quad (2.4.7)$$

Here N_f denotes the number of considered SM quark flavors, while N_c refers to the color factor. The fermionic partial decay width $\Gamma_{f\bar{f}}$ depending on the coupling is given by

$$\Gamma_{f\bar{f}}^V = \frac{g_f^2 (M_{\text{med}}^2 + 2m_f^2)}{12\pi M_{\text{med}}} \sqrt{1 - \frac{4m_f^2}{M_{\text{med}}^2}} \quad (2.4.8)$$

$$\Gamma_{f\bar{f}}^A = \frac{g_f^2 (M_{\text{med}}^2 - 4m_f^2)}{12\pi M_{\text{med}}} \sqrt{1 - \frac{4m_f^2}{M_{\text{med}}^2}} \quad (2.4.9)$$

2.4. DARK MATTER PRODUCTION IN THE MONO-W CHANNEL

with f denoting either a SM quark or dark matter. Fig. 2.11-left shows the ratio $\Gamma_{\text{med}}/M_{\text{med}}$ of the mediator width and the mediator mass for subsequent mediator masses.

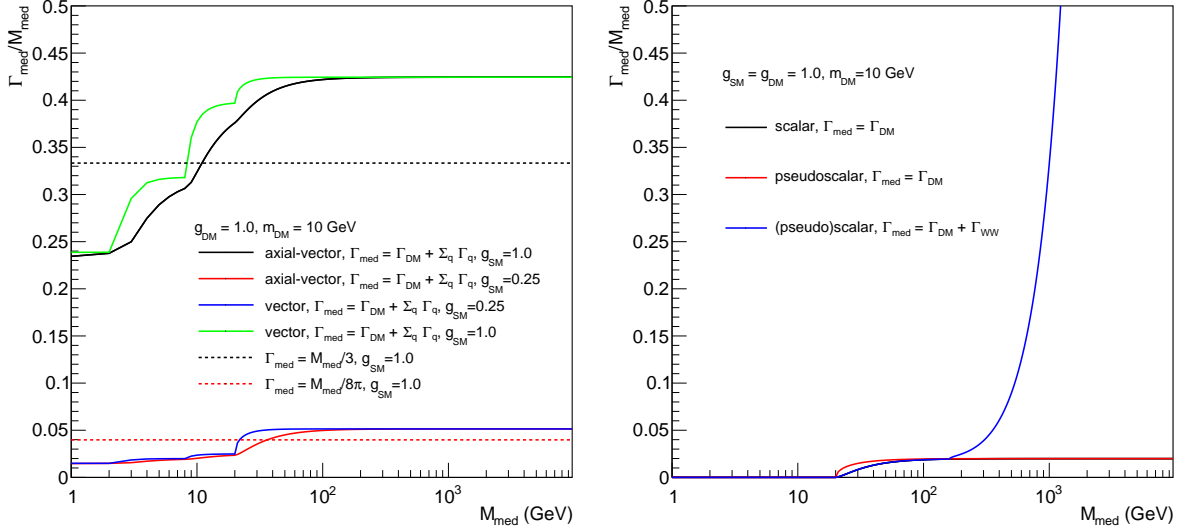


Figure 2.11: Ratio of the mediator decay width and M_{med} depending on M_{med} . Left: The ratio is shown for an axial-vector and vector coupling mediator with different quark coupling strengths $g_{\text{SM}} = 0.25$ and $g_{\text{SM}} = 1.0$. A narrow and broad mediator width approximation of $\Gamma_{\text{med}} = M_{\text{med}}/3$ and $\Gamma_{\text{med}} = M_{\text{med}}/8\pi$ is additionally shown. Right: Shown is the ratio $\Gamma_{\text{med}}/M_{\text{med}}$ for a scalar and pseudoscalar coupling mediator which couples to a pair of W bosons and DM. In order to visualize the influence of the W boson pair coupling contribution, the ratio corresponding to DM coupling only is shown as well.

The considered scalar mediator couples to both dark matter and a pair of W bosons, therefore a lower bound on the mediator width is given by

$$\Gamma_{\text{Med}}^S = \Gamma_{\chi\bar{\chi}}^S + \Gamma_{WW}^S \quad (2.4.10)$$

with the partial decay widths $\Gamma_{\chi\bar{\chi}}^S$ and Γ_{WW}^S [29]

$$\Gamma_{\chi\bar{\chi}}^S = \frac{g_{DM}^2 m_{DM}^2 m_{\text{MED}}}{8\pi v^2} \left(1 - \frac{4m_{DM}^2}{m_{\text{MED}}^2}\right)^{\frac{3}{2}} \quad (2.4.11)$$

$$\Gamma_{WW}^S = \frac{1}{4\pi} \frac{m_W^4}{M_{\text{med}} v^2} \sqrt{1 - \frac{4M_{\text{med}}^2}{m_W^2}} \left(3 + \frac{1}{4} \frac{M_{\text{med}}^4}{m_W^4} - \frac{M_{\text{med}}^2}{m_W^2}\right). \quad (2.4.12)$$

Fig. 2.11-right shows the ratio $\Gamma_{\text{med}}/M_{\text{med}}$ for a scalar mediator. Considering the partial decay width of the mediator to a pair of W bosons, the ratio reaches the perturbative limit of $\Gamma_{\text{med}}/M_{\text{med}} = 0.5$ at a mediator mass of $M_{\text{med}} \approx 1$ TeV, which will

be used as an upper bound on the considered mediator mass in the analysis. For the pseudoscalar mediator an approximation of its decay width is determined using eq. 2.4.10 with the partial decay width $\Gamma_{\chi\bar{\chi}}^P$:

$$\Gamma_{\text{Med}}^P \approx \Gamma_{\chi\bar{\chi}}^P + \Gamma_{WW}^S \quad (2.4.13)$$

$$\Gamma_{\chi\bar{\chi}}^P = \frac{g_{DM}^2 m_{DM}^2 m_{\text{MED}}}{8\pi v^2} \left(1 - \frac{4m_{DM}^2}{m_{\text{MED}}^2} \right)^{\frac{1}{2}} \quad (2.4.14)$$

In general, the mediator width Γ_{med} depends on the simplified model parameter space $M_{\text{med}}, m_{DM}, g_{SM}$ and g_{DM} . As an approximation, a narrow width approach is further used, which corresponds to a mediator which annihilates into only one quark flavor and helicity with $g_{SM} = g_{SM} = 1$ [28]. In this case, $\Gamma_{\text{med}}/M_{\text{med}} = \frac{1}{8\pi}$ can be used as an approximate lower limit, which has also been utilized in [28, 30, 24].

Upper bounds on the mediator width are derived from the perturbative limit. In order for the theory to be perturbative,

$$\sqrt{g_{SM}g_{DM}} < 4\pi \quad (2.4.15)$$

has to hold [30]. Considering the chosen coupling values $g_{DM} = 1$ and $g_{SM} = \{0.25, 1\}$ this requirement is satisfied. The upper perturbative bound for the mediator width is given by [31]:

$$\frac{\Gamma_{\text{med}}}{M_{\text{med}}} \lesssim 0.5 \quad (2.4.16)$$

A conservative upper bound for a broad mediator width is $\Gamma_{\text{med}} = M_{\text{med}}/3$, as also used in [28, 30].

2.4.3 Comparison of dark matter production mechanisms

In order to evaluate the validity of the EFT approach and the requirement for simplified models, numerical simulations using a Monte Carlo signal generator are performed. For both axial-vector and vector coupling mediators, the different DM production mechanisms are simulated using Madgraph5 aMC@NLO [32]. In this section, Madgraph5 aMC@NLO is used to determine the production cross section for a given set of model parameters.

For the EFT approach, a model provided by [26] is used, while for axial-vector and vector coupling mediators simplified models provided by [28] and [33] are utilized. The parton distribution function (PDF) set NNPDF30_1o_as_0130, as also used in the Run-2 analysis and included in the official LHAPDF 6.1 sets, is chosen for the simulation. Parton distribution functions play an important role in e.g. proton-proton collisions. A PDF describes the probability of finding a certain parton, which in this case is a constituent of a given proton with a momentum fraction x at a momentum transfer of q^2 .

2.4. DARK MATTER PRODUCTION IN THE MONO-W CHANNEL

For both DM production model approaches, the effect of quark interference is considered. Fig. 2.12 shows the production cross section times branching ratio $\sigma \times \mathcal{B}(pp \rightarrow \chi\bar{\chi}l\nu_l)$, where the lepton is either $l = e, \mu$ for axial-vector coupling models and for destructive interference ($\zeta = +1$), constructive interference ($\zeta = -1$) and coupling to one quark type only ($\zeta = 0$). The inclusion of the branching fraction allows a direct comparison with the single- μ channel. Fig. 2.12-left shows the EFT approach, while in Fig. 2.12-right a simplified model is used. An exemplary contact interaction scale $\Lambda = 500$ GeV is chosen for the EFT approach and a mediator mass of $M_{\text{med}} = 500$ GeV for the simplified model approach. The enhancement of the production cross section for constructive interference becomes apparent, which is of over one order of magnitude compared to destructive interference. A configuration using $\zeta = 0$ also yields an enhancement, which is however less distinct than $\zeta = -1$. The decrease in production cross section for large m_{DM} visible for both approaches is due to the reduction in phase space, as the production of two heavy DM particles and a W boson is suppressed [5].

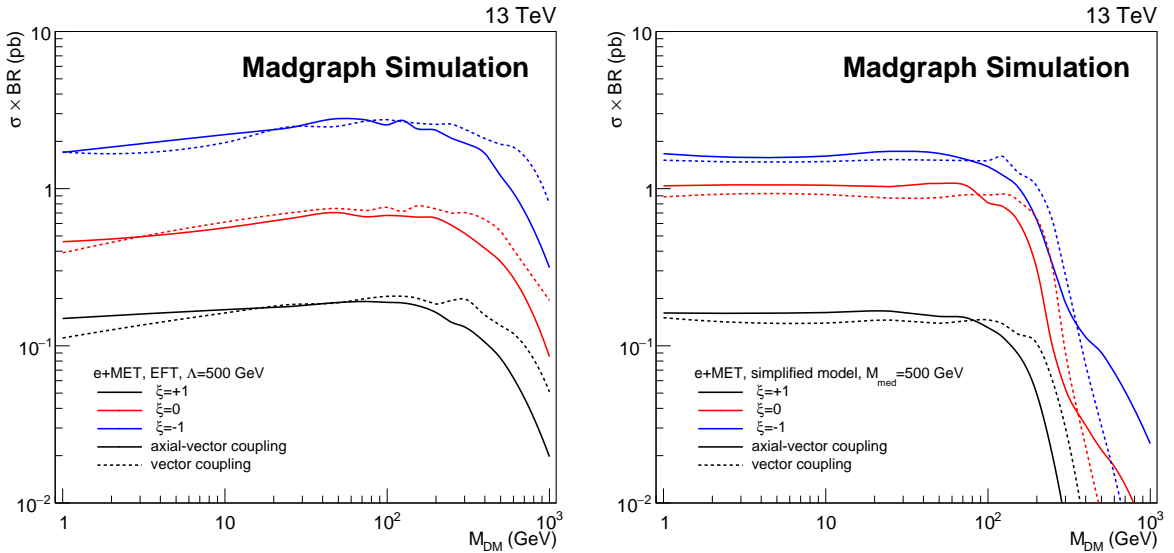


Figure 2.12: Production cross section times branching ratio depending on m_{DM} for the EFT approach (left) and a simplified model (right). Both axial-vector and vector coupling are considered, as well as the effect of quark interference. Constructive interference ($\zeta = -1$) yields the highest production cross section compared to destructive interference ($\zeta = +1$). A narrow mediator width of $\Gamma_{\text{med}} = M_{\text{med}}/8\pi$ has been chosen in the case of simplified model.

Similar results are obtained for both axial-vector coupling and vector coupling models, as shown in Fig. 2.12. This corresponds to the findings in the $\sqrt{s} = 8$ TeV analysis [5]. In the following, focus is placed on axial-vector coupling models and destructive as well as constructive interference, as $\zeta = \pm 1$ leads to largest changes in production cross section.

The comparison is presented two-ways. An estimate for the contact interaction scale

using simplified models is given by

$$\Lambda_{\text{SM}} \propto \sqrt[4]{\frac{\sigma_{\text{SM}}}{\sigma_{\text{EFT}}}} \times \Lambda_{\text{EFT}}, \quad (2.4.17)$$

as Λ is proportional to $\sqrt[4]{\sigma}$. For Λ_{EFT} , a fixed value of 600 GeV used in the $\sqrt{s} = 8$ TeV analysis is chosen [5]. Following [30], Fig. 2.13 shows the resulting contact interaction scale for an axial-vector coupling mediator model with destructive and constructive interference. A light and heavy DM mass of $m_{DM} = 1$ GeV and $m_{DM} = 250$ GeV have been chosen, and Λ_{SM} is shown for different M_{med} and a narrow and broad mediator width, with $g_{DM} = g_{SM}$ set to one.

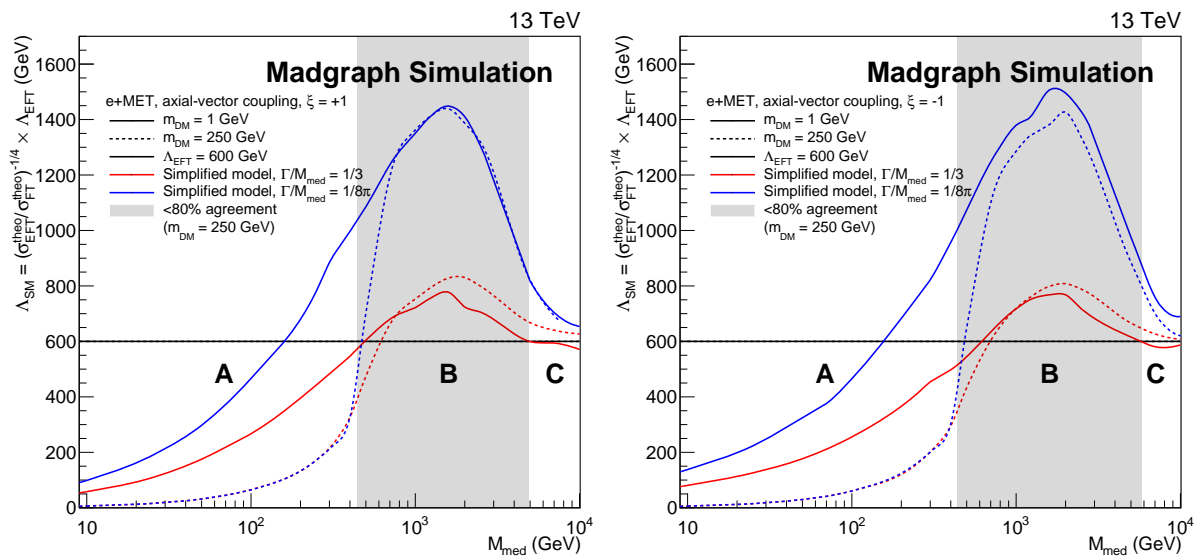


Figure 2.13: Comparison of an axial-vector coupling mediator simplified model to a fixed value of Λ_{EFT} for both a light and heavy DM mass m_{DM} . Shown is the contact interaction scale Λ_{SM} depending on M_{med} for a narrow and broad mediator width. For $m_{DM} = 250$ GeV the mediator mass range is divided into three regions with region B depicted in grey. For region A and C, Λ_{SM} is less dependent on the mediator width as the agreement between both values of Γ_{med} is over 80%. Region B corresponds to the resonant enhancement of the mediator production, in which Λ_{SM} significantly depends on Γ_{med} . Left: $\xi = +1$, right: $\xi = -1$.

Three different regions can be identified which are defined by a certain level of agreement of Λ_{SM} for a broad and narrow mediator width for a given m_{DM} . The central region is indicated by a grey band, which correspond to $< 20\%$ agreement of Λ_{SM} for a heavy DM mass of $m_{DM} = 250$ GeV. Both destructive and constructive interference yield similar results. For mediator masses below ≈ 450 GeV, Λ_{SM} is considerably smaller than Λ_{EFT} . Here, the EFT approach would yield a too high value of Λ_{EFT} , thus providing too strong limits when used in a DM search. For $450 \lesssim M_{\text{med}} \lesssim 5000$ GeV, a resonant enhancement is visible due to the on-shell production of the mediator. The features in the simplified model production cross section are due to the consideration

2.4. DARK MATTER PRODUCTION IN THE MONO-W CHANNEL

of the mediator and whether it can provide resonant enhancement to the production cross section. The latter is the case if on-shell production occurs [34]:

$$M_{\text{med}}^2 > 4m_{DM}^2 + (E_T^{\text{miss}})_{\text{min}}^2 \quad (2.4.18)$$

Here E_T^{miss} denotes the missing transverse energy as defined in eq. 5.4.1. The value $(E_T^{\text{miss}})_{\text{min}}$ refers to the minimal value of missing transverse momentum, on which no lower cut will be imposed in this analysis. Large values of both m_{DM} and $(E_T^{\text{miss}})_{\text{min}}$ hence prohibit on-shell mediator production, thus suppressing the production cross section [34]. In the resonant enhancement region, the EFT approach yields a too low constant value of Λ_{EFT} , while not describing the resonant enhancement. Above $M_{\text{med}} > 5$ TeV both approaches give comparable results, as $\Lambda_{\text{SM}} \approx \Lambda_{\text{EFT}}$. In this region the EFT approach remains valid.

As discussed in Sec. 2.4.2, the contact interaction scale is given by

$$\Lambda_{\text{EFT}} = \frac{M_{\text{med}}}{\sqrt{g_{\text{SM}}g_{\text{DM}}}}. \quad (2.4.19)$$

Using this relation, values of Λ_{EFT} can be included in a M_{med} -dependent representation of the DM production cross section.

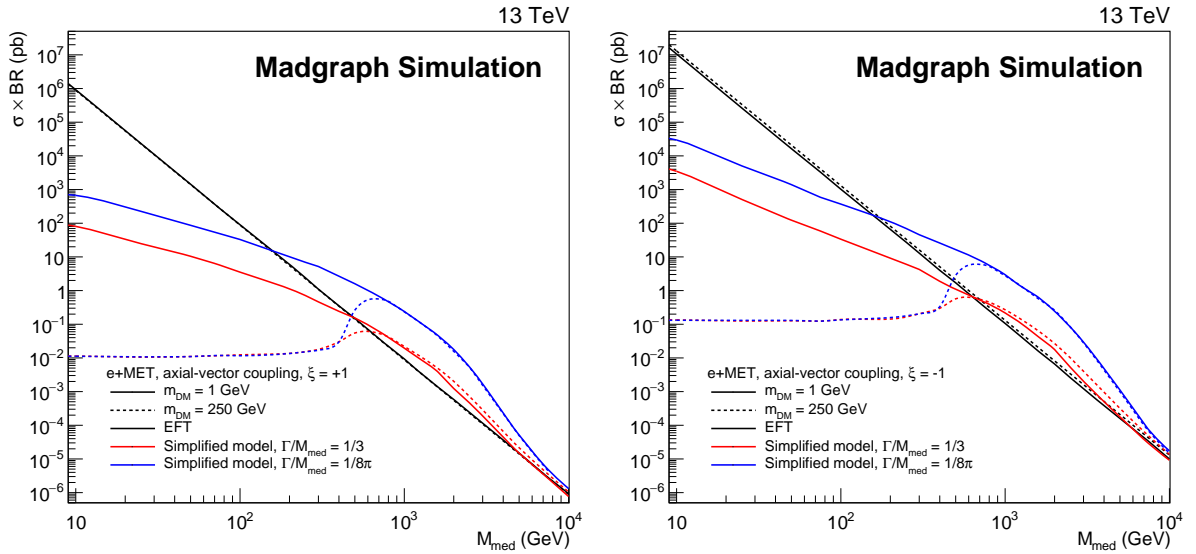


Figure 2.14: Comparison of the EFT approach and simplified models for an axial-vector coupling mediator showing the DM production cross section times branching ratio. A light and heavy m_{DM} is considered, as well as a broad and narrow mediator width. Left: $\zeta = +1$, right: $\zeta = -1$.

Following [34], Fig. 2.14-left shows the DM production cross section times branching ratio for the EFT approach and an axial-vector coupling mediator simplified model using the same parameters as in Fig. 2.13. Again, the three different regions of model description disagreement, resonant mediator production enhancement, and subsequent model description agreement are visible.

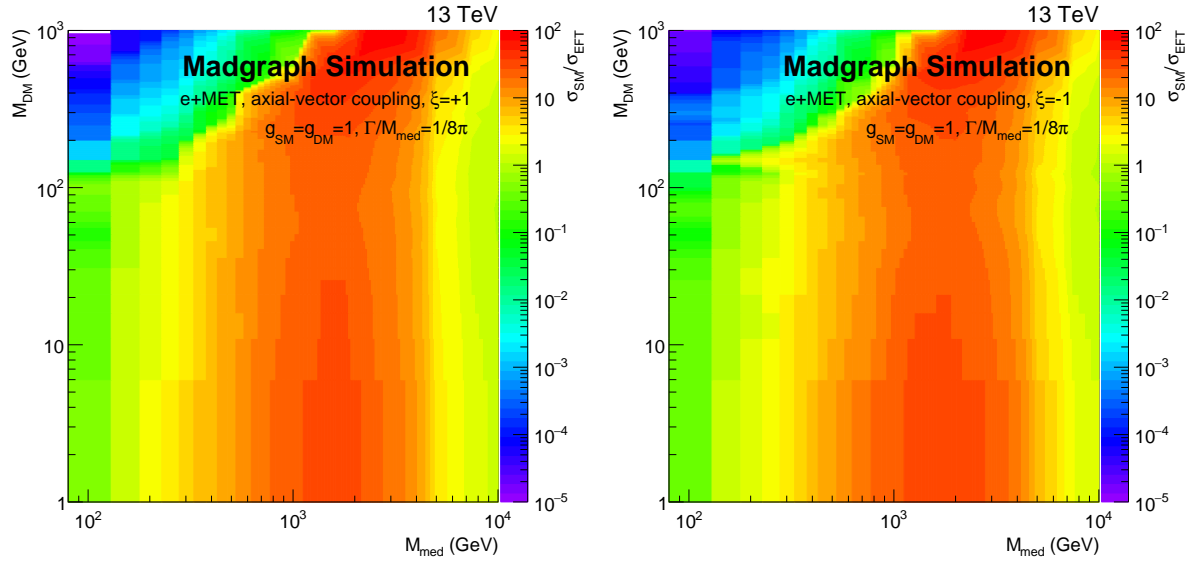


Figure 2.15: Level of agreement between the EFT approach and an axial-vector coupling simplified model for different m_{DM} and M_{med} . Left: $\xi = +1$, right: $\xi = -1$. For heavy mediator masses M_{med} both approaches yield $\frac{\sigma_{SM}}{\sigma_{EFT}} \approx 1$, indicated in light green, while the resonant enhancement in the simplified model is indicated in red color.

In order to quantify the agreement between the EFT approach and simplified models and thus the validity region of the EFT approach, Fig. 2.15 shows the ratio $\frac{\sigma_{SM}}{\sigma_{EFT}}$ for different pairs of M_{med} and m_{DM} as well as for destructive and constructive interference. A narrow mediator width $\Gamma_{med} = M_{med}/8\pi$ is considered. Good agreement between the models yields $\frac{\sigma_{SM}}{\sigma_{EFT}} \approx 1$ and is indicated as light green. Between $150 \text{ GeV} \lesssim M_{med} \lesssim 300 \text{ GeV}$ both approaches yield comparable results in the transition between regions A and B as defined in Fig. 2.13. For heavier M_{med} the resonant enhancement becomes apparent. For $M_{med} \gtrsim 7 \text{ TeV}$ (9 TeV) for destructive (constructive) interference, the simplified model approach shows agreement with the EFT approach in the asymptotic limit.

2.4.4 Conclusion

Simplified models have been introduced and the transition from the EFT approach has been motivated, which is only valid when considering heavy mediator masses above $M_{med} \approx 9 \text{ TeV}$. Necessary assumptions concerning the mediator of the DM production mechanism have been discussed, requiring a minimal flavour violation and zero coupling to leptons in order to avoid established constraints. For the DM interpretation of the Run-2 data, simplified models also offer the possibility to study further mediator coupling mechanisms as pseudoscalar and scalar coupling. Lower and upper bounds have been determined for the mediator width. The lower bound determines the maximum parameter reach in this analysis. Including heavy mediator masses in the simplified model parameter selection provides a comparison to the EFT approach used in the Run-1 analysis.

Chapter 3

The Compact Muon Solenoid

The collider search for dark matter is performed with the Compact Muon Solenoid (CMS) experiment hosted at the Large Hadron Collider (LHC). The Large Hadron Collider is located at CERN near Geneva in the border region of Switzerland and France. It is a circular collider with a circumference of 27 km, providing proton-proton collisions currently at a center-of-mass energy of 13 TeV. Fig. 3.1 shows the location and general layout of the collider, as well as the major LHC experiments including the CMS experiment.

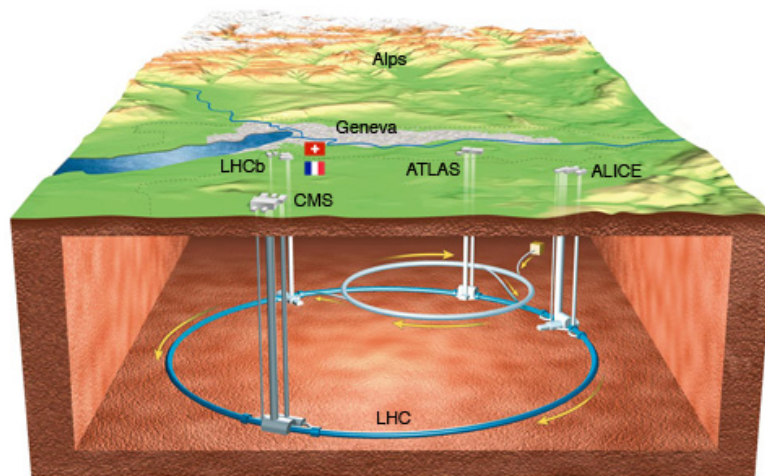


Figure 3.1: The Large Hadron Collider (LHC) with the accompanied main experiments ATLAS, ALICE, CMS and LHCb. Image source: CERN.

The following discussion is based on the official CMS documentation [35]. The CMS detector is designed to study proton-proton collisions at a center-of-mass energy of up to $\sqrt{s} = 14$ TeV. Fig. 3.2 shows a transverse cross section of the general layout of the detector. The inner detector components are surrounded by a superconducting solenoid which creates a magnetic field of $B = 3.8$ T. The innermost layer of the detector encompasses the silicon tracker, which allows for precision measurement of the momentum of charged particles diverted by the magnetic field. The crystal electromagnetic and a sampling hadron calorimeter follow. Outwards, the iron return yoke interspersed with the muon chambers is located. Exemplary particle tracks are indi-

cated in Fig. 3.2 for charged particles including leptons and hadrons, as well as neutral hadrons and a photon. Electrons and charged hadrons exhibit a bended track in the silicon tracker with their energy deposited in the electromagnetic and hadron calorimeter, respectively. Neutral particles such as neutrons or photons only deposit energies in the respective calorimeters without showing a track in the silicon tracker. Muons are minimum-ionizing particles and reach the muon chambers located outwards from the electromagnetic and hadron calorimeter.

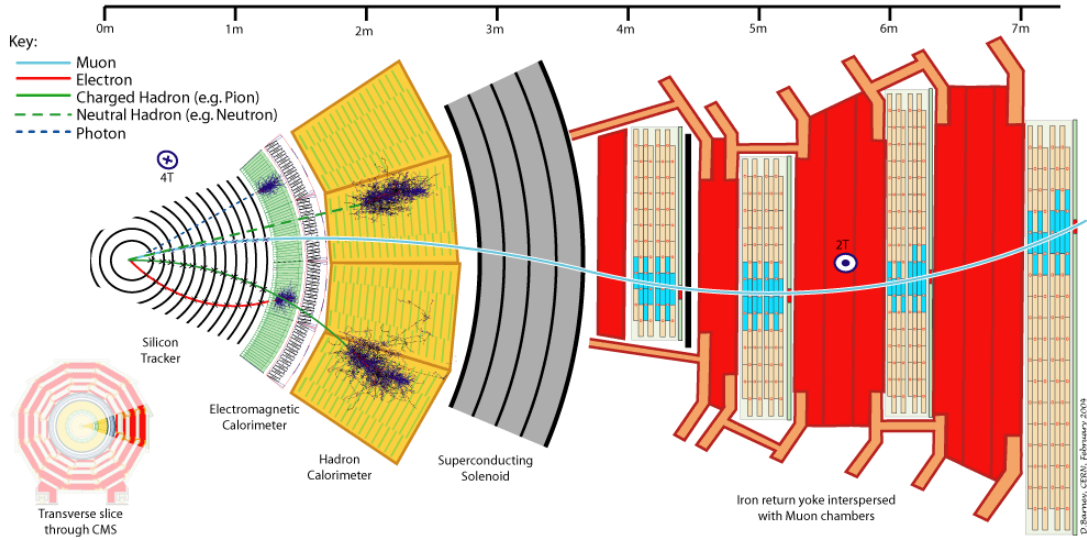


Figure 3.2: Transverse cross section through the Compact Muon Solenoid (CMS) detector. Depicted are the silicon tracker, the electromagnetic and hadron calorimeter, the superconducting solenoid and the muon chambers with exemplary tracks of five different particles. Figure from [36].

In order to describe the different longitudinal regions of the detector, the quantity of pseudorapidity is used as defined by

$$\eta = -\ln \tan \frac{\theta}{2}.$$

In the following it is used in particular to distinguish between the barrel region ($|\eta| < 1.2$) and the endcap region ($1.2 < |\eta| < 2.4$) of the detector.

The inner tracking system consists of a silicon pixel detector containing 1440 pixel modules in three barrel layers and a silicon strip tracker containing 15148 strip detector modules in 10 barrel detection layers. Charged particles create electron-hole pairs in the silicon material, which is characterized by the presence of a band gap. Electrons can thus be excited from the valence band to the conduction band. The resulting electric field proportional to the particle's energy and the number of electron-hole pairs is then measured, and the charged particle's track can be recorded.

The electromagnetic calorimeter is used to measure the energy of charged particles as well as photons and is comprised of individual scintillating lead tungstate (PbWO_4) crystals. The calorimeter is structured into a barrel volume with a radius of 129 cm and two endcaps. While 61200 crystals are located in the barrel region, 7324 crystals

are located in each endcap. An overall high granularity limits the effects of high pile-up [37]. The scintillation of the crystal triggered by electrons and photons is detected with avalanche photodiodes in the barrel and vacuum phototriodes in the endcaps [35].

The sampling hadron calorimeter is comprised of an alternating absorber and active scintillation material, structured into a barrel volume and two endcaps as well as an outer calorimeter volume. It is designed to measure the energy of hadrons. The determination of possible missing transverse energy is of special importance. For the absorber material, brass plates are used, with the exception of stainless steel in the inner- and outermost regions. The active material consists of trays of plastic scintillators connected to wavelength shifting fibres. The scintillators are optically connected to hybrid photodiodes.

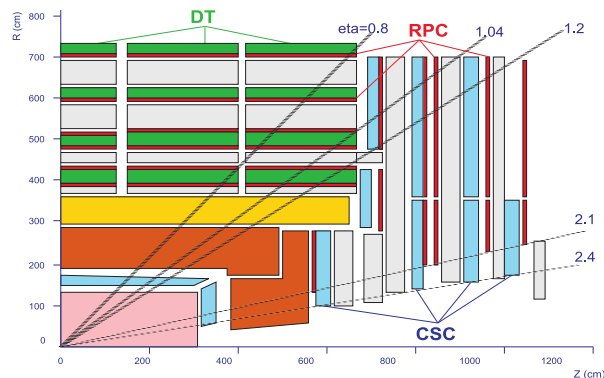


Figure 3.3: Layout of the CMS muon chambers with the location of the different types of gaseous detectors. Shown are drift tubes (DT), resistive plate chambers (RPC) and cathode strip chambers (CSC). Reproduced from [37].

Muons are detected through three different types of gaseous detectors depending on the radiation environment of the given muon chamber [38]. Drift tubes are used in the low-radiation barrel region ($|\eta| < 1.2$). In the endcap region ($|\eta| < 2.4$), cathode strip chambers are used. In order to provide high-precision timing for the trigger information, resistive plate chambers are used in both regions up to $|\eta| < 2.1$ [37].

As the LHC provides proton-proton collisions at a high rate of 40 MHz, the CMS experiment utilizes a sophisticated trigger system in order to select the events which are stored. The reduction of available data is necessary as not all detected events can be recorded and processed due to the high amount of events, which is further increased by multiple interactions from the same bunch crossing referred to as pile-up. The trigger system consists of the hardware-based Level-1 (L1) and the software-based high-level trigger (HLT). The L1 trigger uses programmable electronics to analyze coarse segmented energy deposits in the calorimeters as well as signals in the muon chambers to provide the Global Calorimeter and Global Muon trigger information for a given event, resulting in a reduced data rate of at most 100 kHz. Detector information is then aggregated by the data acquisition (DAQ) system, which provides the specialized HLT software with a complete data read out. The combined trigger system provides a reduction of data by a factor of $\approx 10^6$ [35].

The recorded data is stored and processed in the CMS offline computing system, which further provides the data to the Worldwide LHC Computing Grid (WLCG) used for the

CHAPTER 3. THE COMPACT MUON SOLENOID

individual physics analyses.

In this analysis, the impact of the High-Luminosity LHC upgrade is discussed in Ch. 6, for which the CMS detector will be upgraded to accommodate very high luminosity conditions. The planned detector upgrade is presented in Ch. 6.2.

Chapter 4

Simulation tools

In this chapter the different simulation tools necessary for the data analysis and for the HL-LHC upgrade studies are discussed. First the Monte Carlo generators used to simulate the Standard model background contributions as well as the dark matter and W' signals are presented, followed by CMS detector simulation tools, which model the detector response.

4.1 Monte Carlo sample generation

Monte Carlo generators are used to model high-energy collision processes. Depending on the specific program, the hard process as well as the final state parton shower is generated. The standard output format of such generators is the Les Houches Event (LHE) file format as defined by the Les Houches Accord [39], which can be then further used for the detector response simulation of the process. The different simulation tools are presented and their specific role in the overall analysis is discussed.

4.1.1 Madgraph5 aMC@NLO

Madgraph5 aMC@NLO [32] is a versatile framework which is capable of simulating both SM and BSM processes. For a given initial and final state, it determines the cross section and generates the hard interactions. QCD corrections to SM processes can be determined with next-to-leading order (NLO) accuracy. Madgraph5 aMC@NLO has already been introduced for the determination of the dark matter production cross section in Ch. 2.4.3. In this analysis, version 2.3.3 is used. The primary role of Madgraph5 is the co-determination of the dominant SM background in the mono-electron channel, the W boson decay including jets, and the simulation of simplified model DM samples with axial-vector and vector coupling of the mediator between SM and DM particles. Further applications are the determination of sub-leading backgrounds such as single-top production and γ +jets production.

4.1.2 POWHEG BOX

POWHEG BOX [40,41,42] is a general framework for NLO Monte Carlo particle shower calculations. It provides integrated SM and BSM processes. Furthermore it may be used with other MC generators for showering. In this analysis, it is used for SM background contributing processes as single top production and Drell-Yan ($pp \rightarrow l\bar{l}$) processes.

4.1.3 Pythia

Pythia [43, 44] models high-energy collision processes at LO and features integrated hard processes and models for initial and final state parton showers, parton-parton interactions and particle decays. In this analysis, Pythia 8 is used to simulate the off-shell leptonic W decays as well as the Diboson ($pp \rightarrow WW, WZ, ZZ$) background contributions at LO.

4.1.4 JHU generator

The JHU¹ generator [45] is a specialized MC generator which models processes involving a single-produced X resonance, such as $ab \rightarrow X \rightarrow VV$, where V can be either a Z or W boson as well as a photon. Furthermore vector boson fusion or $ab \rightarrow VX$ processes may be modelled. In this analysis, the JHU generator is used to generate the simplified model DM samples involving a mediator with scalar and pseudoscalar coupling to SM bosons and DM particles, for which a Feynman diagram is shown in Fig. 2.10.

While Madgraph5 is able to simulate the mediator decay into a pair of dark matter particles, the JHU generator provides information about the hard process as well as spin information and cross section up to the point of the mediator generation. The subsequent decay into a pair of dark matter is handled by the external program `boltdmdec`. The cross section remains unchanged by the use of `boltdmdec`.

4.2 CMS detector simulation

The CMS detector response simulation may be simulated with either a full or a parametrized simulation. While the full simulation is demanding computing-wise, a fast simulation uses a parametrization of the detector.

4.2.1 GEANT4

The full CMS detector simulation is done using the GEANT4 toolkit [46], which is included in the CMS software (CMSSW) framework 7.4.6. It simulates the passage of particles through matter, which may be arranged in a complex geometry as it is the

¹Johns Hopkins University

case of the CMS detector. The physics simulation includes electromagnetic, hadronic and optical processes with a library of predefined particles, materials and geometrical elements. The program itself uses Monte Carlo techniques to model the passage and decay with subsequent showering of particles, where different kinds of matter yield respective stochastic parameters for the simulation [46]. Full detector simulations are used in the determination of DM exclusion limits as well as partially for the HL-LHC upgrade studies.

4.2.2 DELPHES

In contrast to a full detector simulation of the complete geometry and materials, DELPHES [47] offers a fast simulation method in which the detector response of a hadron collider is parametrized. The simulation covers the tracker, magnetic field, electromagnetic and hadron calorimeters as well as the muon detectors, in which the physics objects induce a parametrized detector response. In this analysis, it is used for the HL-LHC upgrade studies, as DELPHES also features the simulation of high pile-up conditions.

The detector response parameters such as the geometrical acceptance of sub-detectors and their finite resolution are described in DELPHES data cards [48]. The data cards used in this analysis are referenced in Sec. 9.2 of the appendix.

Chapter 5

Search for new physics with LHC Run-2 at $\sqrt{s} = 13$ TeV

In this chapter, the search for new physics in the mono-electron channel with data recorded in 2015 at $\sqrt{s} = 13$ TeV is presented. The search results for a W' boson with the data and SM background contributions have been successfully approved for public presentation at the LHC End-Of-Year Jamboree 2015 [49].

5.1 Analysis method

The analysis signature involves a high energy lepton, in this case an electron, and large missing transverse energy. The analysis uses the transverse mass M_T as the main discriminant variable, which is defined by the transverse momentum of the lepton p_T^l , the transverse missing momentum E_T^{miss} , and the azimuthal angle between the two directions:

$$M_T = \sqrt{2 p_T^l E_T^{\text{miss}} (1 - \cos \Delta\phi(l, E_T^{\text{miss}}))}$$

Deviations of data and the SM background contribution are evaluated in the transverse mass distribution and are interpreted as 95% CL exclusion limits.

5.2 Data

After the initial start of the $\sqrt{s} = 13$ TeV period (Run-2), several data-taking runs have been performed in 2015 with different configurations and conditions. The aim was to provide pp collisions with a bunch spacing of 25 ns and a magnetic field of 3.8 T. Tab. 5.1 shows the progression to these conditions.

For this analysis, the run D data-taking period is used, which yields a total integrated luminosity of $\mathcal{L} = 2.2 \text{ fb}^{-1}$ using certified runs only¹. Prior runs exhibited varying

¹For this analysis, certified runs from the Golden JSON dating from 13th Nov. 2015 containing runs

Run	B (T)	Δt_{bunch} (ns)	\mathcal{L} (pb^{-1})	runs
A	0	50	45.03 + 26.48	248036-248038
B	3.8	50 ns	45.03	251244-251283
C	3.8	50 + 25	26.48 + 14.61	254833 + 254231-254914
D	3.8	25	2193.53	256630-260627

Table 5.1: Data-taking periods of Run-2 with the CMS detector.

conditions or no magnetic field and were thus omitted. Data certification of runs and subsequent luminosity sections ensures that all detector subsystems were operating as intended and thus can be used for physics analyses. A single electron trigger was required for the selection of the dataset. In particular, the following datasets were used:

- /SingleElectron/Run2015D-050ct2015-v1/MINIAOD
- /SingleElectron/Run2015D-PromptReco-v4/MINIAOD

The data is prepared centrally at CERN in the MINIAOD version 2 format, which represents a high-level data tier for mainstream physics analyses featuring a small event size of 30-50 kb/event while retaining necessary event information [50]. The format contains information about the high level physics objects, the full list of reconstructed particles using the ParticleFlow algorithm and trigger information. High level physics objects include leptons, E_T^{miss} , photons and jets, for which detailed information is saved. Furthermore, trigger level 1 to level 3 and residual corrections to jets are applied and type 1 corrections to E_T^{miss} . Information about the ParticleFlow list is minimized, while retaining the four-vector, impact parameter, PDG identification number and certain quality flags. The trigger information include the prescale values of all triggers as well.

The data samples are prepared for the analysis by converting the events into the PXLIO² format, which is described in [51]. Further selection criteria such as the lepton identification are applied, which are described in Sec. 5.4. The global tag 74X_dataRun2_v5 is used, which represents the CMS software version and run conditions, such as detector calibration and alignment, which affects the physics object reconstruction.

5.3 Standard model background

In order to evaluate the level of agreement between data and Standard Model prediction, an accurate description of the SM background in the mono-electron channel is required, as several SM processes may yield the same final state $l + E_T^{\text{miss}}$. In order of decreasing importance, these background contributions are as follows:

- leptonic W decay: $W \rightarrow l\nu$

256630 - 260627 have been used.

²Physics eXtension Library Input Output format

- $t\bar{t}$ production
- single-top production, such as $gb \rightarrow tW$ or $qb \rightarrow q't$
- Drell-Yan processes: $Z \rightarrow l\bar{l}$
- Diboson processes: WW, WZ, ZZ

The dominant background in the analysis is the leptonic W decay $W \rightarrow e\nu$.

Monte Carlo simulations are used to model these types of SM background contributions. The MC samples are obtained from the CMS MC production in the previously presented MINIAOD version 2 format (Sec. 5.2). For MC samples, the MINIAOD format includes the MC generator information as well. The MC samples have been prepared using the global tag `74X_mcRun2_asymptotic_v4`. Tab. 5.2 lists the individual simulated SM backgrounds along with the MC generator information and cross-section.

5.3.1 Higher order corrections for the W Standard Model background

As $W \rightarrow e\nu$ processes present the dominant contributions to the overall SM background in the analysis, these processes need to be simulated with high accuracy in the high M_T region. The MC simulation is performed in leading order accuracy calculation using PYTHIA, which includes parton shower simulations to consider higher jet multiplicities. The simulation is then further enhanced by including QCD and electroweak higher order corrections.

Following the approach presented in [52], an invariant mass-dependent correction factor k for the differential cross-section of the W boson is defined as

$$k(M_{\text{inv}}) = \frac{\Delta\sigma_{(N)NLO} / \Delta M_{\text{inv}}}{\Delta\sigma_{LO} / \Delta M_{\text{inv}}}$$

in which M_{inv} is the invariant mass of the lepton-neutrino system. σ_{NLO} is determined by including electroweak calculations and σ_{NNLO} by including QCD calculations with two jets. The calculations are based on a MC approach. NLO calculations are included with the MCSANC event generator [53], which calculates Drell-Yan processes at NLO precision. From EW and NLO QCD only NLO EW is used. NNLO calculations are performed using the FEWZ³ generator [54]. To combine the NLO and NNLO contributions, either an additive or factorized approach can be utilized:

$$\left[\frac{d\sigma}{d\mathcal{O}} \right]_{\text{QCD} \oplus \text{EW}} = \left[\frac{d\sigma}{d\mathcal{O}} \right]_{\text{QCD}} + \left[\frac{d\sigma}{d\mathcal{O}} \right]_{\text{EW}} - \left[\frac{d\sigma}{d\mathcal{O}} \right]_{\text{LO}}$$

$$\left[\frac{d\sigma}{d\mathcal{O}} \right]_{\text{QCD} \otimes \text{EW}} = \left(\frac{\left[\frac{d\sigma}{d\mathcal{O}} \right]_{\text{QCD}}}{\left[\frac{d\sigma}{d\mathcal{O}} \right]_{\text{LO}}} \right) \times \left[\frac{d\sigma}{d\mathcal{O}} \right]_{\text{EW}}$$

Background		Generator	σ (pb)
W	WjetsToLNu	Madgraph NLO	61526.7
	WjetsToLNu HT-100To200	Madgraph LO	1347
	WjetsToLNu HT-200To400	Madgraph LO	360
	WjetsToLNu HT-400To600	Madgraph LO	48.98
	WjetsToLNu HT-600To800	Madgraph LO	12.8
	WjetsToLNu HT-800To1200	Madgraph LO	5.261
	WjetsToLNu HT-1200To2500	Madgraph LO	1.334
	WjetsToLNu HT-2500ToInf	Madgraph LO	0.03089
W offshell	WToENu M-200 13 TeV	Pythia 8 LO	6.236
	WToENu M-500	Pythia 8 LO	0.2138e
	WToENu M-1000	Pythia 8 LO	0.01281
	WToENu M-3000	Pythia 8 LO	2.904e-05
	WToMuNu M-200	Pythia 8 LO	6.236
	WToMuNu M-500	Pythia 8 LO	0.2138
	WToMuNu M-1000	Pythia 8 LO	0.01281
	WToMuNu M-3000	Pythia 8 LO	2.904e-05
	WToTauNu M-200	Pythia 8 LO	6.236
	WToTauNu M-500	Pythia 8 LO	0.2138
	WToTauNu M-1000	Pythia 8 LO	0.01281
	WToTauNu M-3000	Pythia 8 LO	2.904e-05
Top	single top s-channel 4f leptonDecays	Madgraph NLO	10.11
	single top t-channel 4f leptonDecays	Madgraph NLO	216.99
	single top tW antitop 5f inclusiveDecays	PowHeg NLO	38.09
	single top tW top 5f inclusiveDecays	PowHeg NLO	38.09
	ttbar 13 TeV MCRUN2 74 V9 ext3-v1	PowHeg NLO	831.76
	ttbar Mtt-1000toInf 13 TeV MCRUN2 74 V9 ext1-v2	PowHeg NLO	18.0602
Drell Yan ($Z \rightarrow \tau\tau$)	DYjetsToLL M-10to50	Madgraph LO	18610
	DYjetsToLL M-50	Madgraph LO	6104
	DYjetsToLL M-100to200	Madgraph LO	226
	DYjetsToLL M-200to400	Madgraph LO	7.67
	DYjetsToLL M-400to500	Madgraph LO	0.423
	DYjetsToLL M-500to700	Madgraph LO	0.24
	DYjetsToLL M-700to800	Madgraph LO	0.035
	DYjetsToLL M-800to1000	Madgraph LO	0.03
	DYjetsToLL M-1000to1500	Madgraph LO	0.016
	DYjetsToLL M-1500to2000	Madgraph LO	0.002
Drell Yan ($Z \rightarrow e\bar{e}$, $Z \rightarrow \mu\bar{\mu}$)	DYjetsToLL M-2000to3000	Madgraph LO	0.00054
	ZToLL M_50_120	Powheg NLO	1975
	ZToLL M_120_200	Powheg NLO	19.3
	ZToLL M_200_400	Powheg NLO	2.73
	ZToLL M_400_800	Powheg NLO	0.241
	ZToLL M_800_1400	Powheg NLO	0.01678
	ZToLL M_1400_2300	Powheg NLO	0.0013
	ZToLL M_2300_3500	Powheg NLO	8.95e-05
	ZToLL M_3500_4500	Powheg NLO	4.13e-06
	ZToLL M_4500_6000	Powheg NLO	4.560e-07
γ + jets	ZToLL M_6000_Inf	Powheg NLO	2.066e-08
	Gjets HT-40To100	Madgraph LO	23080
	Gjets HT-100To200	Madgraph LO	9110
	Gjets HT-200To400	Madgraph LO	2281
	Gjets HT-400To600	Madgraph LO	273
	Gjets HT-600ToInf	Madgraph LO	94
Diboson	WW 13 TeV	Pythia 8 LO	63.21
	WZ 13 TeV	Pythia 8 LO	22.82
	ZZ 13 TeV	Pythia 8 LO	10.32

Table 5.2: Simulated MC samples for the considered SM background contributions. For each background sample the generator used and its (N)LO cross-section \times branching fractions are specified. Leptonic decays are indicated with $L = \mu, e, \tau$.

Fig. 5.1 shows the resulting correction factor for different M_{inv} and both additive and factorized combination. Both combination methods can be equally motivated: For the additive approach the assumption is made that electroweak corrections are of additive nature and thus can be added for all orders of QCD corrections. The factorized approach on the other hand assumes the electroweak corrections to be the same for all orders of QCD corrections. This analysis follows the recommendation of the Les Houches working group [55] to use the additive combination method for determining k while determining the difference to the factorized combination as its uncertainty.

³abbreviation for Fully Exclusive W and Z production.

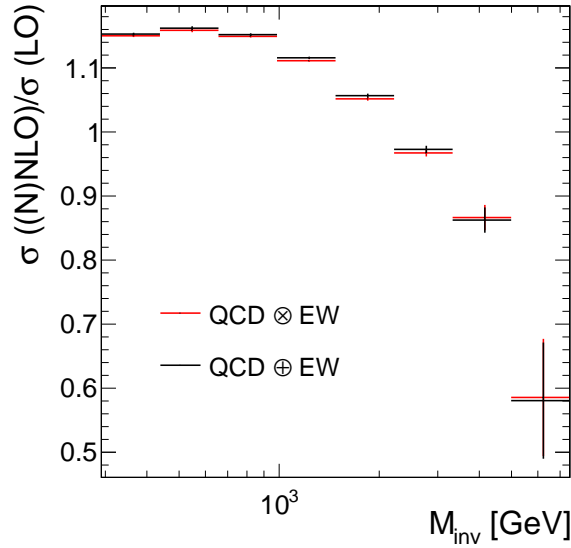


Figure 5.1: Higher order corrections for the W SM background in the single-electron channel for different M_{inv} . Both additive and factorized combination methods are shown. In the analysis, the additive approach is used for the correction factor k . The subsequent uncertainty on k is determined from the difference to the factorized method.

5.4 Physics objects

In this section, the physics objects relevant to this analysis - electrons and missing transverse energy - are presented.

5.4.1 Electron

Electrons are selected from the electron candidates present in the events triggered by the high-level electron trigger using the High Energy Electron Positron (HEEP) identification criterion documented in [56, 57]. In this analysis, HEEP version 6.0 is used as recommended for Run-2.

Electron trigger

In this analysis, either a high- p_T or low- p_T trigger requirement is used. For the high- p_T trigger, which is also used in [49], at least one of the following high-level electron triggers have to be triggered, with a minimum p_T of 105 GeV or 115 GeV, respectively:

- HLT_Ele115_CaloIdVT_GsfTrkIdT_v*
- HLT_Ele105_CaloIdVT_GsfTrkIdT_v*

An offline p_T cut of 130 GeV is applied to avoid trigger-turn-on effects and to remain in the flat efficiency plateau [49] shown in Fig. 5.2.

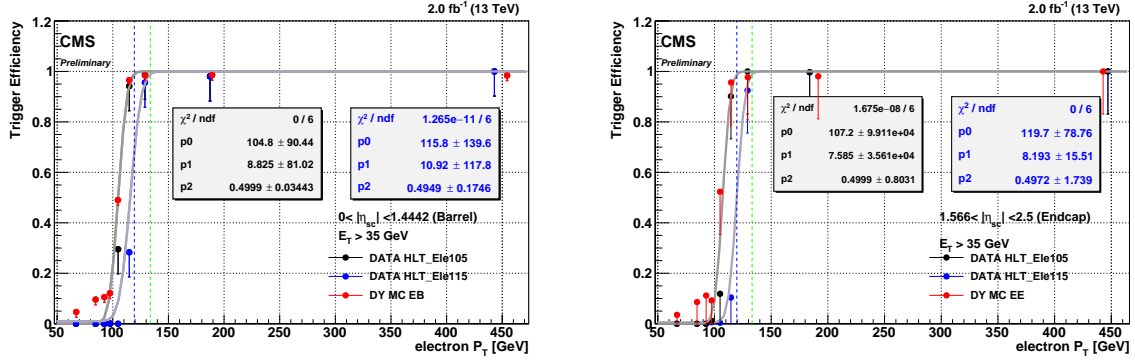


Figure 5.2: Electron trigger efficiency depending on the electron transverse momentum for the barrel (left) and endcap region (right). For $p_T \gtrsim 130$ GeV the trigger efficiency reaches a constant value of $\epsilon \approx 1$ for both considered high- p_T electron triggers. A tag and probe method was used with MC truth matching to a Drell-Yan MC sample. Figure from [58].

Unless explicitly stated, a high- p_T trigger with $p_T > 130$ GeV is used. For the low- p_T trigger, at least one of the following electron triggers have to be triggered with a minimum p_T of 27 GeV:

- HLT_Ele27_eta2p1_WP75_Gsf_v*
- HLT_Ele27_eta2p1_WPLoose_Gsf_v*

In this case, an offline p_T cut of 35 GeV is used.

HEEP 6.0 identification criteria

Tab. 5.3 shows the variables used for the HEEP 6.0 identification in order to select a well isolated high energy electron or positron.

HEEP variable	Barrel	Endcap
E_T	> 35 GeV	
η range	$ \eta_{SC} < 1.44$	$1.57 < \eta_{SC} < 2.5$
isEcalDriven	true	
$ \Delta\eta_{in}^{seed} $	< 0.004	< 0.006
$ \Delta\phi_{in} $	< 0.06	
$\frac{H}{E}$	$< \frac{1}{E} + 0.05$	$< \frac{5}{E} + 0.05$
full $5 \times 5 \sigma_{ij\eta}$	-	< 0.03
full $5 \times 5 E^{2 \times 5} / E^{5 \times 5}$	> 0.94 or $E^{1 \times 5} / E^{5 \times 5} > 0.83$	-
EM + hadr. depth 1 isolation	$< 2 \text{ GeV} + 0.03 \cdot E_T + 0.28 \cdot \rho \text{ GeV}$	$< 2.5 \text{ GeV} + 0.28 \cdot \rho \text{ GeV}$ ($E_T < 50 \text{ GeV}$) $< 2.5 \text{ GeV} + 0.03 \cdot (E_T - 50 \text{ GeV}) \text{ GeV} + 0.28 \cdot \rho \text{ GeV}$ ($E_T > 50 \text{ GeV}$)
track isolation (track p_T)	< 5	
inner layer lost hits	≤ 1	
$ d_{xy} $	< 0.02	< 0.05

Table 5.3: High Energy Electron Positron (HEEP) 6.0 identification criteria. Different criteria are used for the barrel and endcap regions.

The HEEP variables are described in [57]. The main variable is the transverse energy, which is derived from $E_T = E_{\text{supercluster}} \cdot \sin \theta$, where θ is the polar angle between the

electron track at the inner layer of the tracker and the extrapolated interaction vertex. A supercluster refers to a collection of calorimeter clusters, which collect radiated energy from a local energy maximum deposited in a basic cluster. In Tab. 5.3, η_{SC} refers to the pseudorapidity of the electron supercluster with respect to the detector cluster. By requiring `isEcalDriven`, the electrons are identified using $e\gamma$ techniques rather than the tracker-driven `ParticleFlow` algorithm. The latter is not validated for non-isolated low energy electrons or high-energy electrons.

$|\Delta\eta_{in}^{seed}|$ and $|\Delta\varphi_{in}|$ refer to the difference of φ or η of the inner layer track position and the supercluster.

The ratio $\frac{H}{E}$ refers to the hadronic energy H of the CaloTowers centered on the position of the electron ($r = 0.15$) and the supercluster energy E . The variable $\sigma_{i\eta}$ refers to the variance of energy in the 5x5 crystal block around the seed crystal.

Further HEEP variables consider the lepton isolation in hadronic calorimeter depth and track p_T isolation. The variable d_{xy} is the minimum distance in the transverse plane from the beamspot. For the isolation criteria, the respective variable is evaluated within a specific cone size and an isolation condition is imposed.

5.4.2 Missing transverse energy

Physics objects may be reconstructed using specialized approaches as in the case of electrons presented above, or by using the `ParticleFlow` algorithm, which combines the information from all subdetector systems [59]. By reconstructing all particles in the detector, the missing transverse energy is determined via

$$E_T^{\text{miss}} = -\sum_i p_{T,i}. \quad (5.4.1)$$

Collision products which escape detection in the detector and cannot be reconstructed thus contribute to E_T^{miss} . Such particles can be neutrinos, non-SM particles or non-identified particles, as e.g. very forward particles with $\eta > 5$ which are outside the calorimeter acceptance. Furthermore, detector noise effects or inactive detector cells also contribute, as do potentially unaccounted physics processes as pile-up, underlying events, the beam halo or influences of cosmic radiation [60].

In this analysis, E_T^{miss} is used as provided in the MINIAOD format (`pfMET`), which contains jet energy scale corrections (type-I corrections⁴) and their propagations.

The applied correction is based on the energy response of the reconstructed jets in the event with the intent to remove biases due to possible non-linear and η -dependent calorimeter responses [60]. Here, `ak4PFJetsCHS` jets with $p_T > 15$ GeV were used. A list of recommended E_T^{miss} filters has been applied to further enhance E_T^{miss} ⁵.

⁴The used jet energy scale corrections are `Summer15_25nsV6_DATA.db` for data samples and `Summer15_25nsV6_MC.db` for MC samples.

⁵primary vertex filter, CSC beam halo filter, HBHE noise filter, HBHEiso noise filter, ee badSC noise filter

5.5 Event selection

The basic event selection consists of the electron trigger requirement, a minimum offline p_T of 130 GeV (high- p_T trigger) or 35 GeV (low- p_T trigger) as well as $M_T > 50$ GeV.

The analysis aims to select events in which the lepton recoils against the missing transverse energy. To select the characteristic lepton + E_T^{miss} signature and to suppress the SM background, advantage is taken of back-to-back kinematics. In a balanced event, the ratio p_T/E_T^{miss} is expected to be a distribution centered around one, while the angular distribution $\Delta\phi$ is expected to show a maximum at π . In this analysis, the kinematic cut variables p_T/E_T^{miss} and $\Delta\phi$ may either be defined as static or M_T -dependent.

The static kinematic cut variables previously used in the $\sqrt{s} = 8$ TeV analysis [5] are as follows:

- $\Delta\phi > 2.5$
- $0.4 < p_T/E_T^{\text{miss}} < 1.5$

Furthermore, M_T -dependent kinematic cut variables are explored and their influence on the analysis sensitivity is evaluated. By requiring a certain minimal signal efficiency for each bin of a M_T distribution, M_T -dependent functions for p_T/E_T^{miss} and $\Delta\phi$ are determined. This approach is discussed in Ch. 5.12.5.

In the following, preselection refers to the basic selection while for the full selection the kinematic cuts are applied as well.

5.6 Pile-up reweighting

The effect of pile-up refers to the number of additional interactions in the same bunch crossing, which increases the number of vertices in a given event [61]. The effect is considered in the simulations by superimposing minimum bias interactions in order to provide the same conditions.

The number of additional interactions per luminosity section can be determined by averaging the number of reconstructed primary vertices per event, while considering a vertex reconstruction efficiency of $\approx 70\%$. An alternative method is to measure the instantaneous luminosity for each bunch crossing and to multiply with the total inelastic cross-section. In this analysis, the latter presents the recommended method to determine pile-up, with the vertex counting method is used as a cross-check [61]. Fig. 5.3 shows the number of primary vertices before (left) and after pile-up reweighting for the MC simulation (right).

5.7 Multijet background estimation

Fig. 5.4 shows the distributions p_T/E_T^{miss} and $\Delta\phi$ at preselection, which exhibit a significant disagreement between data and MC simulation. At this stage, only trigger and

5.7. MULTIJET BACKGROUND ESTIMATION

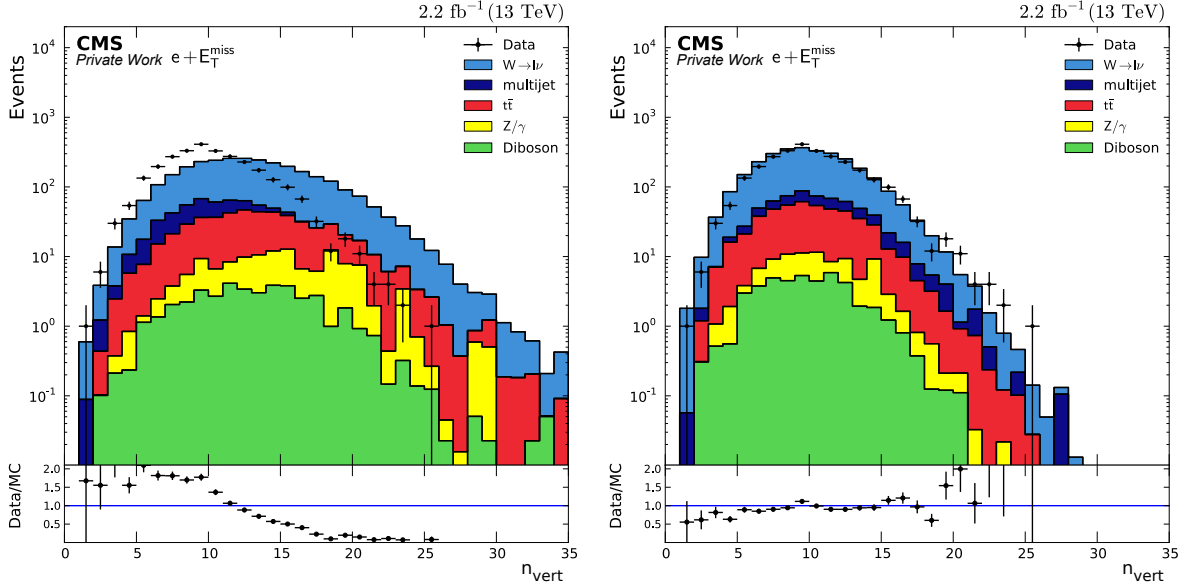


Figure 5.3: Number of primary vertices per event. Left: before pile-up reweighting, right: after pile-up reweighting for the MC simulation.

identification requirements are imposed, and no kinematic cuts have been applied yet. The source of this disagreement are QCD multijet contributions, which in contrast to the $\sqrt{s} = 8$ TeV analysis are non-negligible for $\sqrt{s} = 13$ TeV.

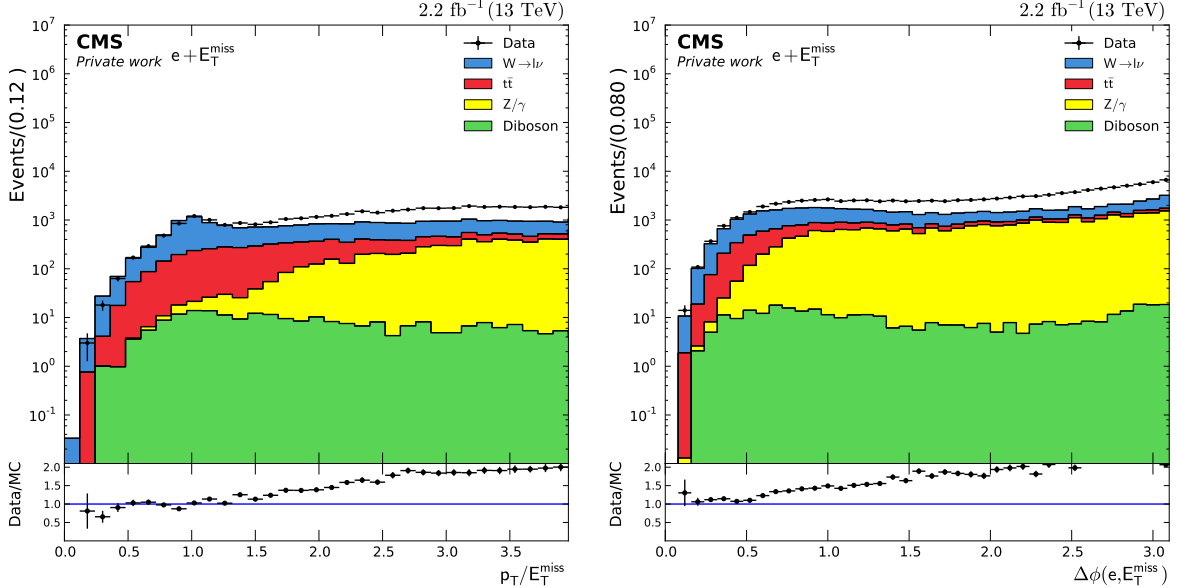


Figure 5.4: Kinematic distributions p_T/E_T^{miss} and $\Delta\phi$ before including the data-driven QCD multijet background contribution.

The QCD multijet background is due to jets misidentified as prompt electrons. As available QCD MC simulations cannot be used because of the unknown amount of higher order corrections needed, they also do not provide sufficient statistics and a data-driven approach is therefore used instead.

Fig. 5.5 shows the ABCD method from [62, 5] used to determine the multijet background, whose shape and normalization is derived from data. The signal region is defined as $0.4 < p_T/E_T^{\text{miss}} < 1.5$, while the QCD region is defined as $p_T/E_T^{\text{miss}} > 1.5$. A tight-to-loose ratio is measured in the QCD region which represents the control region between the non-isolated (region C) and isolated (region D) events. This ratio is then used to scale the non-isolated events to the isolated ones in the signal region.

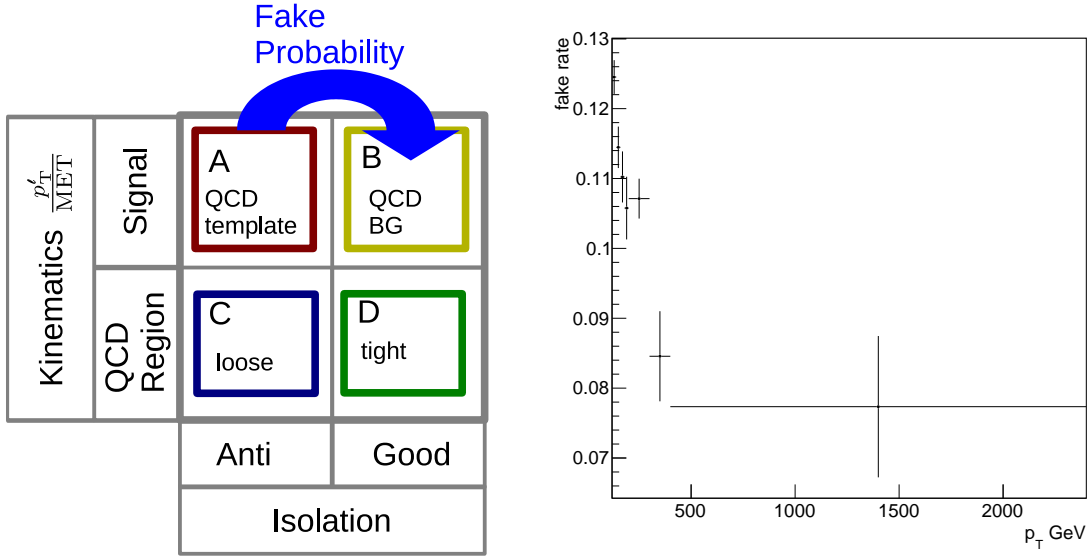


Figure 5.5: Left: ABCD method to determine the data-driven QCD multijet background. Right: resulting fake probability dependent on p_T , which is determined by the tight-to-loose ratio of isolated to non-isolated electrons.

Fig. 5.6 shows the kinematic distributions p_T/E_T^{miss} and $\Delta\phi$ after the inclusion of the data-driven QCD multijet background, which shows a good agreement. While the method is self-predicting in the QCD region, the corresponding events are not considered in the final distribution.

5.8 Systematic uncertainties

Systematic uncertainties are considered in the analysis for the simulated SM background, the data-driven multijet contribution and the signal. For each systematic uncertainty the quantity is shifted either by $\pm 1\sigma$ or within its limits to evaluate its influence in the analysis.

The systematic uncertainties are grouped in global and object-related uncertainties. Considering global systematic uncertainties, an uncertainty of 4.6% is considered for the luminosity. Furthermore, systematic uncertainties of pile-up reweighting and the higher order corrections for the W background are considered. As stated in Sec. 5.3.1, the difference between the additive and factorized combination methods is used as the uncertainty on the higher order correction factor.

The theoretical uncertainty related to the choice of the PDF set is estimated using the updated PDF4LHC prescription, which is a combination of the CT14, MMHT14 and

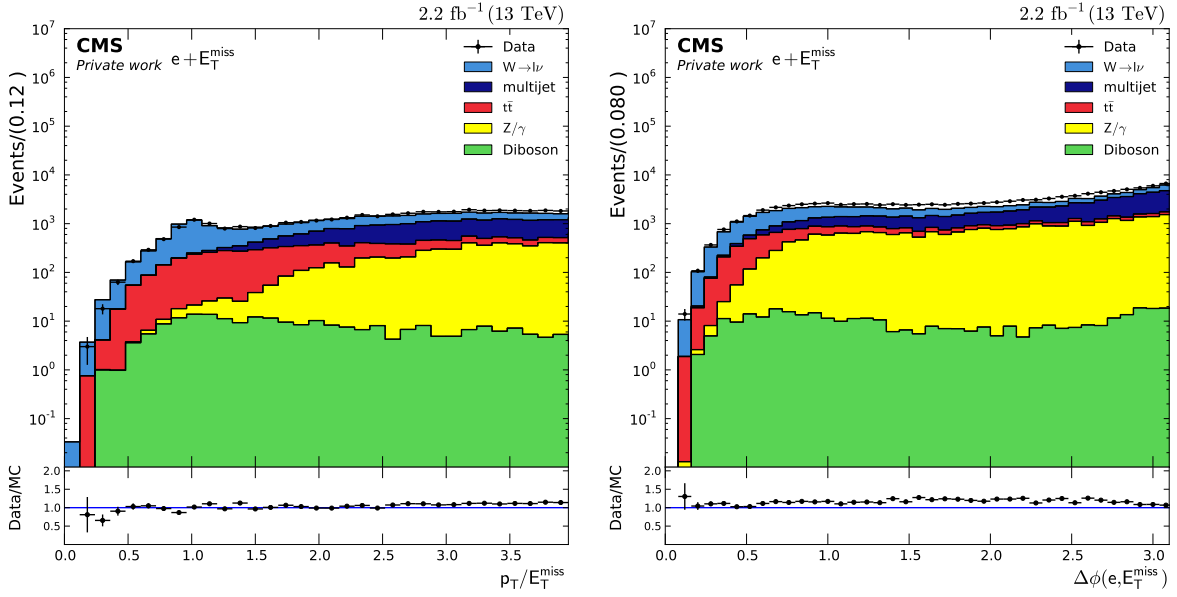


Figure 5.6: Kinematic distributions p_T/E_T^{miss} and $\Delta\phi$ after including the QCD multijet background determined with a data-driven technique.

NNPDF3.0 PDF sets. The combination is done using either a Hessian or MC representation of the the PDF uncertainties, which differ in the assumption of the underlying distribution to be (multi-)Gaussian [55]. For both channels, a symmetric Hessian PDF set with a number of 30 eigenvectors is used.

The electron-related uncertainties include the systematic uncertainty on the energy scale and resolution as well as on the electron identification. Systematic uncertainties from Run-1 are used for the energy scale and resolution [49]. For the energy scale, a systematic uncertainty of 0.4% (0.8%) for the barrel (endcap) region is used. For the energy resolution, a Gaussian smearing of 1.2% (2.4%) is applied to the MC simulation. For the electron identification, a HEEP efficiency of 0.04% (0.1%) as well as a HEEP scale factor of 0.1% (0.2%) is used [56].

Furthermore, the systematic uncertainty on the jet energy scale and resolution is considered by using the CMSSW jet energy corrections version 6.

Fig. 5.7 shows the relative uncertainty of the considered systematic uncertainties in the analysis binned in M_T . The dominant source of systematic uncertainties is the systematic uncertainty of the PDF, followed by the electron energy scale and pile-up uncertainty.

5.9 Final M_T distribution

Fig. 5.8-left shows the final M_T distribution after the electron trigger selection and after all cuts have been applied, which includes the kinematic cut selection discussed in Sec. 5.5, a lower bound on the transverse mass $m_T > 50$ GeV and an offline p_T cut of 130 GeV.

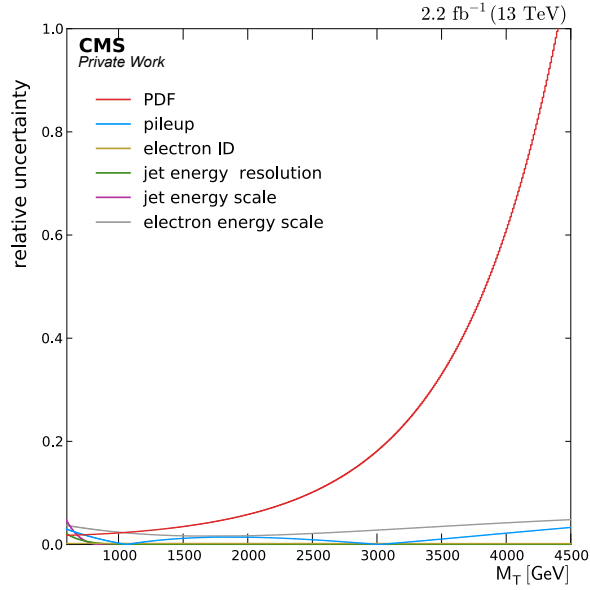


Figure 5.7: Relative systematic uncertainties binned in M_T . The PDF uncertainty constitutes the most dominant systematic uncertainty, followed by the electron energy scale.

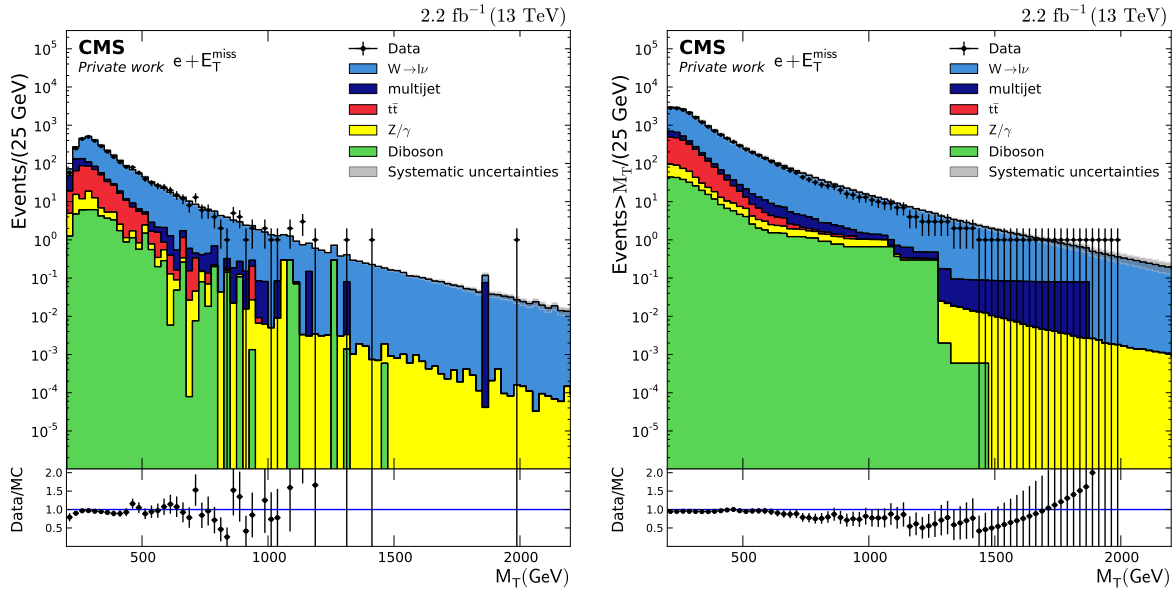


Figure 5.8: Left: Final M_T distribution after electron trigger selection and after all applied cuts. Right: cumulative M_T distribution.

Fig. 5.8-right shows the cumulative M_T distribution, which is constructed via

$$N(M_T) = \sum_{x=M_T}^{\infty} N(x).$$

A deficit of data with respect to the SM background is visible in the M_T distribution for $M_T \gtrsim 700$ GeV. This sample contains one event with a maximum value of $M_T = 1.95$ TeV. This event contains a well isolated reconstructed electron with a clean track, which exhibits a good agreement with the supercluster energy measurement. An event

display is provided in Sec. 9.1 of the appendix.

The deviations of data and SM background contributions are interpreted as 95% CL exclusion limits. In the following, two interpretations including the production of a W' boson and dark matter are considered.

5.10 Limit determination

Following [49], a modified CL_s method described in [63, 64] is used to determine the significance of deviations of data from the Standard Model prediction. The profile likelihood ratio is used as the test statistic q_μ and is given by

$$q_\mu = -2 \ln \frac{\mathcal{L}(\text{data}|\mu, \hat{\theta}_\mu)}{\mathcal{L}(\text{data}|\hat{\mu}, \hat{\theta})} \quad (5.10.1)$$

Systematic uncertainties are included as nuisance parameters θ . A given signal strength $\hat{\mu}$ and nuisance parameter $\hat{\theta}$ maximizes the considered likelihood \mathcal{L} , while a likelihood including $\hat{\theta}_\mu$ has been maximized for a given signal strength μ [58].

A 95% CL limit corresponds to a CL_s ratio $CL_s \leq 0.05$, which is given by

$$CL_s(\mu) = \frac{P(q_\mu \geq q_\mu^{\text{obs}} | \mu s(\theta) + b(\theta))}{P(q_\mu \geq q_\mu^{\text{obs}} | b(\theta))}. \quad (5.10.2)$$

The 95% CL limit is thus determined by tuning the signal strength parameter μ .

5.11 Sequential Standard Model W' interpretation

The first interpretation in terms of physics beyond the Standard Model is a hypothetical SSM W' boson. 95% CL exclusion limits are determined dependent on the mass of the W' boson.

5.11.1 SSM W' signal generation

The simulation of the W' signal is performed using Pythia 8.2 with tune CUETP8M1 using the parton distribution function set NNPDF3.0. A full detector simulation using GEANT4 with subsequent trigger emulation and event reconstruction is performed for different masses of the W' boson. A mass range of 1 - 5.8 TeV with a step size of 200 GeV is considered.

Fig. 5.9 shows the characteristic shape of the M_T distribution for signals with different W' masses of 1, 3.6 and 5 TeV. The signal shape shows a Jacobian peak at approximately its W' mass and extends gradually into the lower M_T region.

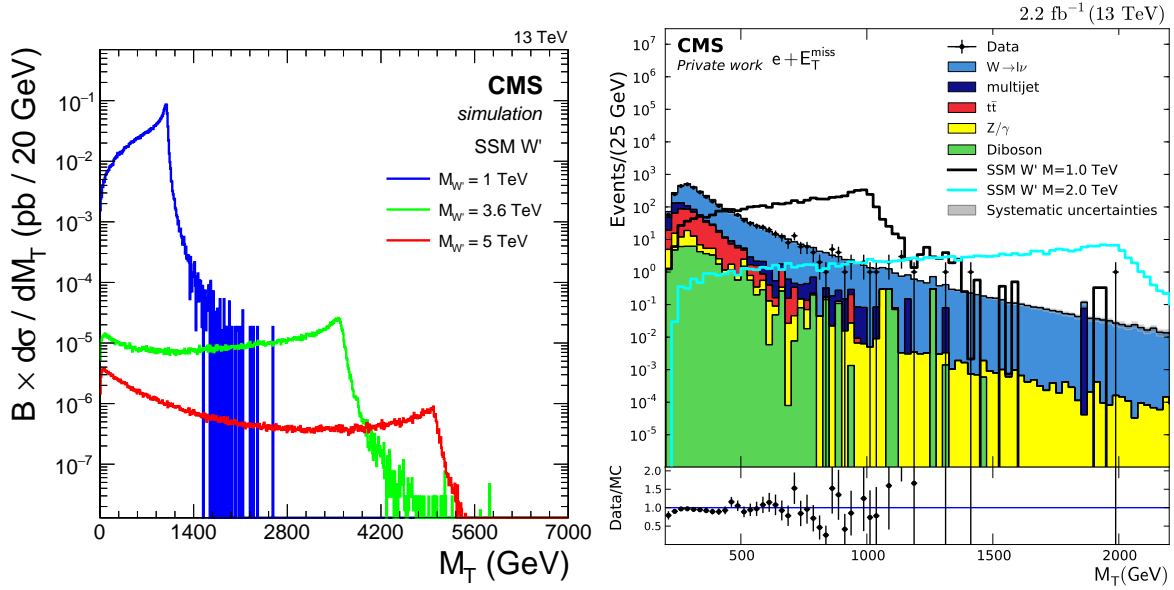


Figure 5.9: Left: W' signal shape on generator level. Right: reconstructed SSM W' signals for two W' masses of 1.0 and 2.0 TeV compared to the SM prediction.

5.11.2 Exclusion limits

Reconstructed W' signals with W' masses of 1.0 TeV and 2.0 TeV are shown in Fig. 5.9 in the full selection. Fig. 5.10-left shows the signal reconstruction efficiency for different W' masses. The efficiency is predominantly flat in the considered W' mass range.

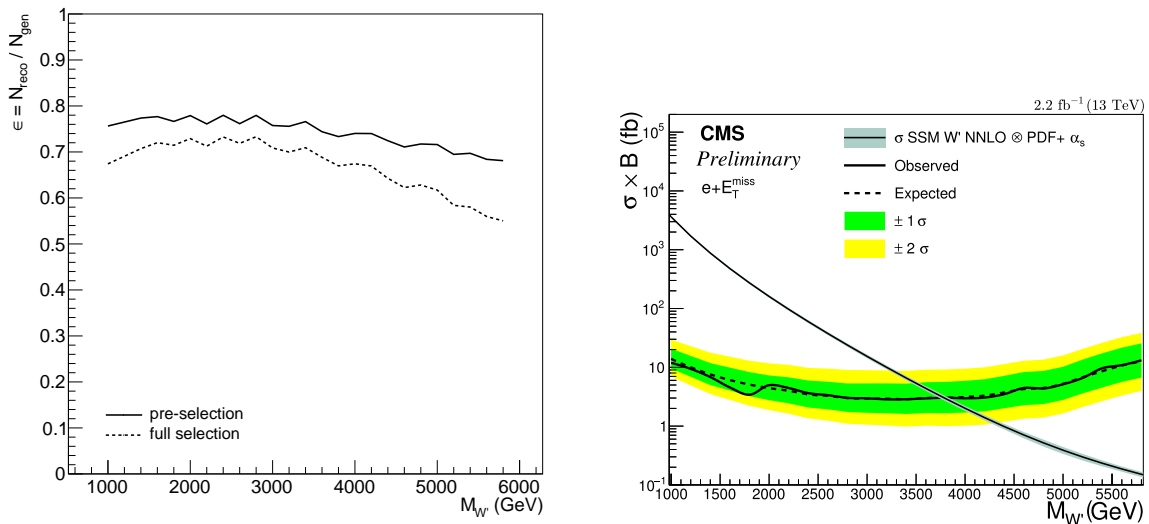


Figure 5.10: Left: W' signal selection efficiency dependent on $m(W')$. Right: expected and observed 95% CL limits on W' production.

Expected and observed 95% CL limits for the considered W' mass range of 1 - 5.8 TeV are shown in Fig. 5.10-right. For the expected 95% CL limit, the $\pm 1\sigma$ and $\pm 2\sigma$

are shown in green and yellow color bands, respectively. The theoretical cross section determined from NNLO⁶ calculations is shown with the uncertainty on the PDF. The intersection of the theoretical cross section and the observed limit yields the excluded cross section σ_{excl} and excluded W' mass $(m_{W'})_{\text{excl}}$. W' masses up to 3.75 TeV can be excluded at 95% CL. This result has been included in a physics analysis summary along with the results of the single-muon channel, which excludes W' masses above 4 TeV [49]. Furthermore, both channels can be combined to produce 95% CL limits while gaining from significantly improved statistics. This way, W' masses up to 4.4 TeV can be excluded.

5.12 Dark matter interpretation

In this section, deviations of data from the expected SM background in the final M_T distribution will be interpreted in terms of dark matter and 95% CL exclusion limits are determined for the model parameter space.

5.12.1 Dark matter signal generation

The dark matter interpretation utilizes simplified models for the description of the dark matter production mechanism. Models introduced in Ch. 2.4.2 with an axial-vector, vector, scalar and pseudoscalar coupling mediator are considered, with their respective Feynman diagrams shown in Fig. 2.9 and 2.10. Depending on the coupling mechanism, different MC generators are used to generate the signal. For an axial-vector and vector coupling mediator, Madgraph5 is used with simplified models provided by J. Kopp et al. [28] and L. Basso [33]. While this setup has already been used for the determination of the production cross sections in Ch. 2.4.3, it is now used to simulate the hard processes.

The implementation by J. Kopp et al. has been used for the generator studies of this analysis, while the implementation by L. Basso was used in the CMS signal production. Both model implementations yield comparable results in both production cross section and M_T signal shape.

Considering scalar and pseudoscalar coupling mediators, the JHU generator is used. The JHU generator generates a single-produced X resonance, which in this case is the mediator particle. The subsequent decay into dark matter is simulated with the external `boltdmdec` tool, which is chained to the output of the JHU generator. With the current implementation, the simulation of the mediator decay is independent of m_{DM} . Nevertheless, results in parameter reach can be determined for different choices of M_{med} .

Fig. 5.11-left shows the distribution in M_T for an axial-vector coupling mediator model. A parameter selection motivated by large changes in M_T shape is shown, which consists of $M_{\text{med}} = 50, 500$ and 2000 GeV and a fixed $m_{DM} = 10$ GeV. It is apparent from Fig. 5.11-right that the effect of quark interference and thus the choice of ζ influences

⁶next-to-next-to leading order

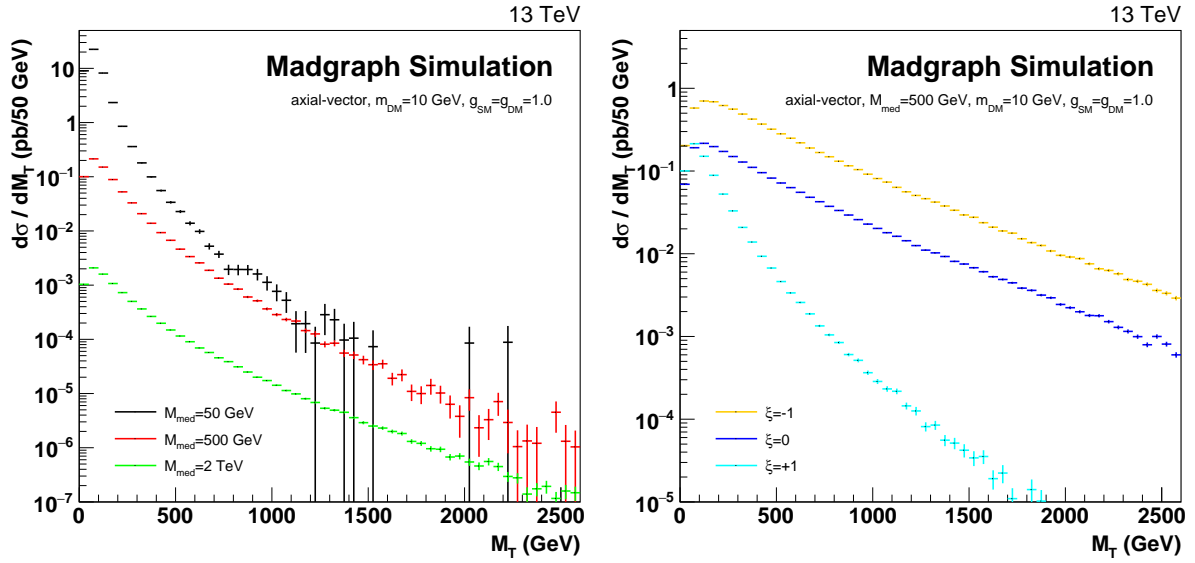


Figure 5.11: Simulation of axial-vector coupling dark matter signals using Madgraph5. Shown is the M_T distribution for mediator masses of $M_{\text{med}} = 50, 500$ and 2000 GeV and constant $m_{DM} = 10$ GeV (left) as well as the quark interference cases $\xi = 0, \pm 1$ for $M_{\text{med}} = 500$ GeV and $m_{DM} = 10$ GeV (right).

the shape of the M_T distribution, which directly translates into different exclusion limits, as the limit determination is sensitive towards the shape of M_T . Both axial-vector and vector coupling mediator models yield similar shapes in the M_T distribution.

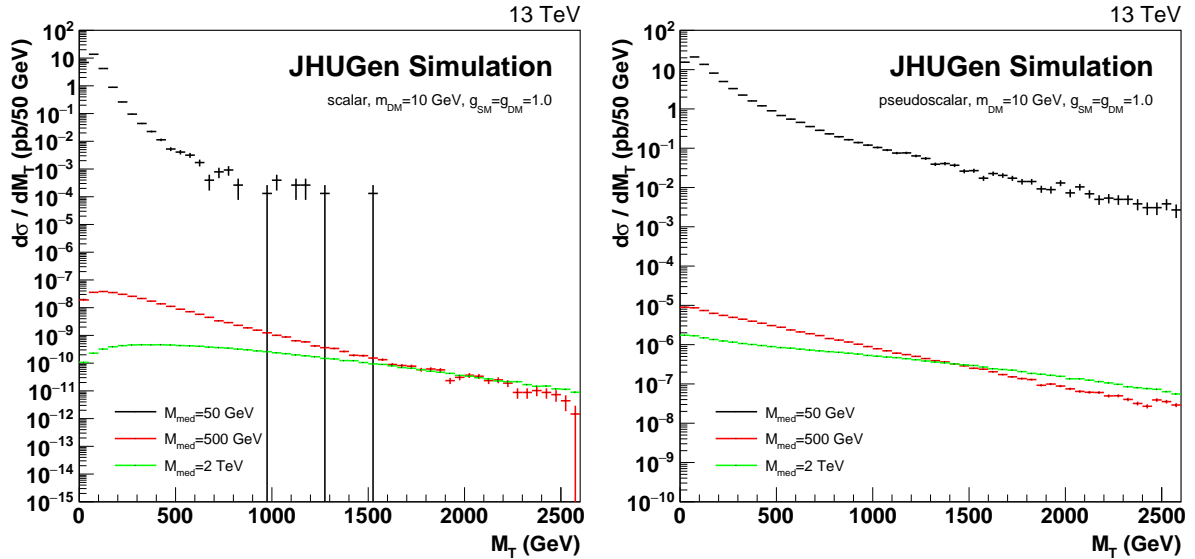


Figure 5.12: Simulation of dark matter signals with mediator masses of $M_{\text{med}} = 50, 500$ and 2000 GeV and constant $m_{DM} = 10$ GeV using the JHU generator. Left: scalar coupling, right: pseudoscalar coupling.

The M_T distributions for a scalar and pseudoscalar coupling mediator model simulated with the JHU generator are shown in Fig. 5.12. A strong dependence of the shape of the M_T distribution with respect to the mediator mass M_{med} is apparent.

5.12.2 Selection of parameter sets for full detector simulation

For a subset of the simplified model parameter space consisting of M_{med} , m_{DM} , g_{SM} and g_{DM} , a full detector simulation using GEANT4 is performed. As this process is computationally expensive, the subset should include a parameter selection which dominantly affects the resulting exclusion limits, thus changes the shape of the M_T distribution. In order to investigate the simplified model parameter space the Dark Matter Forum, a joint collaboration of the ATLAS and CMS experiment was founded. Part of this analysis has been contributed for considerations for the mono-W channel. The findings of this working group have been published in [65]. Considering mono-W searches, the main discriminant quantity in terms of sensitivity is the mediator mass M_{med} and whether the mediator is produced on-shell. The shape of the M_T distribution is predominantly independent of the chosen mediator width Γ_{med} and therefore of the coupling parameters g_{SM} and g_{DM} . This M_T shape independence is verified in [65].

Tab. 5.4 shows the resulting selection of parameters agreed upon in the Dark Matter Forum collaboration, of which full detector simulation signal samples are available in the CMS MC production. The coupling strengths are set to $g_{SM} = g_{DM} = 1$. A heavy mediator of $M_{\text{med}} = 10$ TeV has been included to approximate the EFT approach. Mediator masses with only one corresponding m_{DM} are further included to probe the transition region between the on- and off-shell mediator production.

m_{DM} (GeV)	M_{med} (GeV)													
	10	20	50	100	195	200	295	300	500	995	1000	1995	2000	10000
1	A,V,P	A,V,P	A,V,P	P		A,V,P			A,V,P		A,V,S,P		P	A,V,S,P
10		P	A,V,P	A,V,P		A,V,P		A,V	A,V,P		A,V,S,P		S,P	A,V,S,P
50	A,V		A,V	S,P		A,V,P		A,V	A,V,P		S,P		A,V,P	A,V,S,P
100				A,V	A,V	P		A,V	A,V,P		A,V,S,P		A,V,P	A,V,S,P
150	A,V					A,V	A,V		A,V,P		A,V,S,P		A,V,P	A,V,S,P
500									A,V,P		A,V,S,P		A,V,P	A,V,S,P
1000	A,V									A,V	P		A,V,P	A,V,S,P
												A,V	P	A,V,S,P

Table 5.4: Simplified model parameter set for the mono-W channel as available in the CMS MC production. For each combination of M_{med} and m_{DM} , the letters denote the coupling type for which a MC signal sample is available from the CMSSW 7.4.X MC production. A, V, S and P indicate axial-vector, vector, scalar and pseudoscalar coupling, respectively.

5.12.3 Event reweighting

In order to consider parameters which are not included in the selection shown in Tab. 5.4, event-by-event reweighting is performed. Considering axial-vector and vector coupling mediator models, DM signal samples with full detector simulation are available for destructive interference ($\zeta = +1$) in the CMS MC production. In order to determine exclusion limits for other quark interference cases $\zeta = 0$ and $\zeta = -1$, event reweighting is used. The DM signal is simulated using Madgraph5 with $N_{\text{events}} = 200\text{k}$ for each value of ζ and pairs of M_{med} and m_{DM} . Weights are then produced by dividing the normalized M_T distribution with $\zeta = 1$ by the normalized M_T distribution with either $\zeta = 0$ or $\zeta = -1$. The full detector simulation sample with $\zeta = +1$ is reweighted using the obtained weights.

5.12.4 Reconstructed dark matter signals

Fig. 5.13-left shows the M_T distribution of a reconstructed DM signal for $M_{\text{med}} = 1$ TeV and $m_{DM} = 10$ GeV (axial-vector coupling) compared to the SM background contributions. Fig. 5.13-right shows the M_{med} -dependent signal reconstruction efficiency. The low signal efficiency for $\xi = +1$ is due to the high SM background contributions in the low M_T region. The signal efficiency becomes flat for $M_{\text{med}} > 2$ TeV.

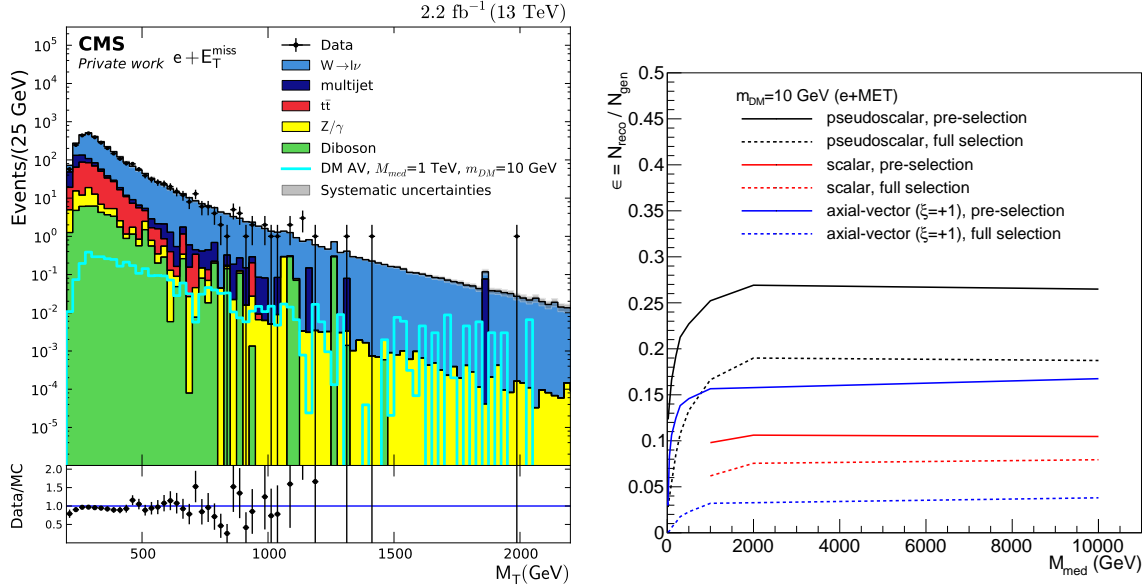


Figure 5.13: Left: reconstructed DM signal for different coupling types with $M_{\text{med}} = 100$ GeV. Right: signal reconstruction efficiency.

5.12.5 Optimization strategies

Two methods of optimizing the analysis results are explored. First, an optimization of the kinematic cut values may yield an improved signal selection efficiency. Furthermore, utilizing a low- p_T trigger may present the opportunity to include transverse momenta below $p_T = 130$ GeV in the analysis, which is of particular interest as the dark matter signal rate shows a local maximum below this threshold. A low- p_T trigger may thus further improve the signal selection.

M_T -dependent kinematic cuts

For high M_T , the Standard Model background has a small contribution. Looser kinematic cuts in this region compared to stringent cuts in the low M_T region containing large contribution of the Standard Model background may thus be chosen. The optimization is performed by maximizing the signal efficiency ϵ and significance s for each bin of size 50 GeV in the M_T distribution and each bin in the kinematic cut variable range. The signal efficiency ϵ is defined as the ratio of the number of events after and prior application of a certain cut. With the predicted number of signal and background

events N_i contained in a given bin, the significance is defined as

$$s = \frac{N_{sg}}{\sqrt{N_{sg} + N_{bg}}}.$$

For a given M_T bin and kinematic cut variable, the bin contained in the possible range of the variable with the highest significance down to a minimal signal efficiency of 50% is chosen. The resulting M_T -dependent cut variable is then fitted to obtain the cut function $f(M_T)$. Fig. 5.14 shows the optimized M_T -dependent cut variables p_T/E_T^{miss} and $\Delta\phi$. The influence of the kinematic cut optimization is evaluated in Sec. 5.12.6.

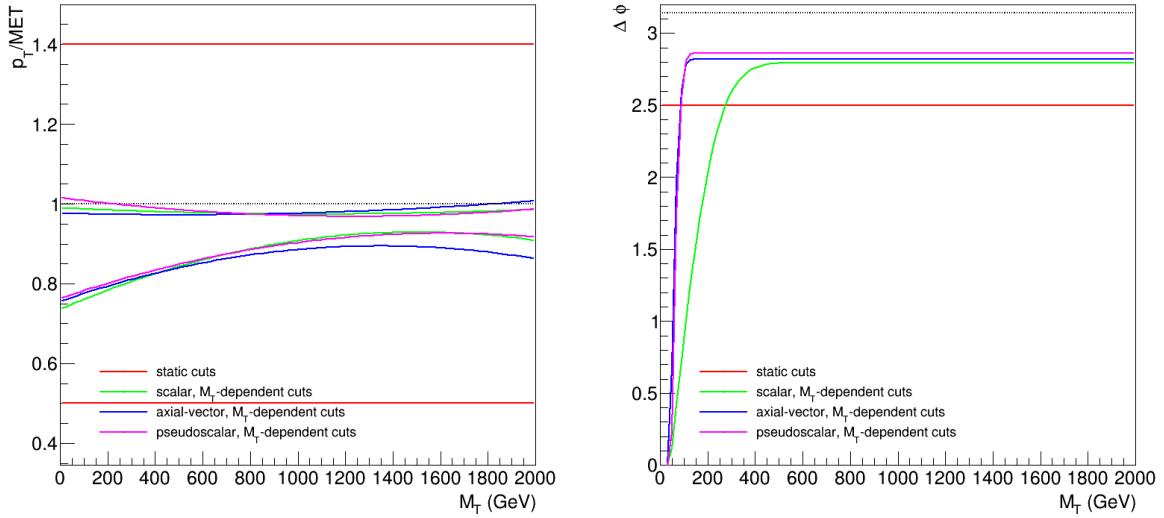


Figure 5.14: M_T -dependent kinematic cut functions p_T/E_T^{miss} (left) and $\Delta\phi$ (right) compared to the static kinematic cut values introduced in Ch. 5.5 shown in red.

Low- p_T trigger

By considering a lower value for the minimum transverse momentum of the lepton, the low- p_T trigger introduced in Ch. 5.5 can be further utilized. Fig. 5.15 shows the M_T distribution after all applied cuts with a modified minimum lepton transverse momentum of $p_T > 35$ GeV and the resulting improved signal selection efficiency.

5.12.6 Exclusion limits in the simplified model parameter space

After establishing the selection for the simplified model parameter space, 95% CL exclusion limits can be determined for the axial-vector, vector, scalar and pseudoscalar mediator coupling models. Upper exclusion limits on the production cross section times branching ratio are determined for pairs of M_{med} and m_{DM} shown in Tab. 5.4. Two-dimensional representations of the four-dimensional simplified model parameter space are then determined in order to evaluate the parameter reach. In the following, Dirac dark matter is considered unless stated otherwise.

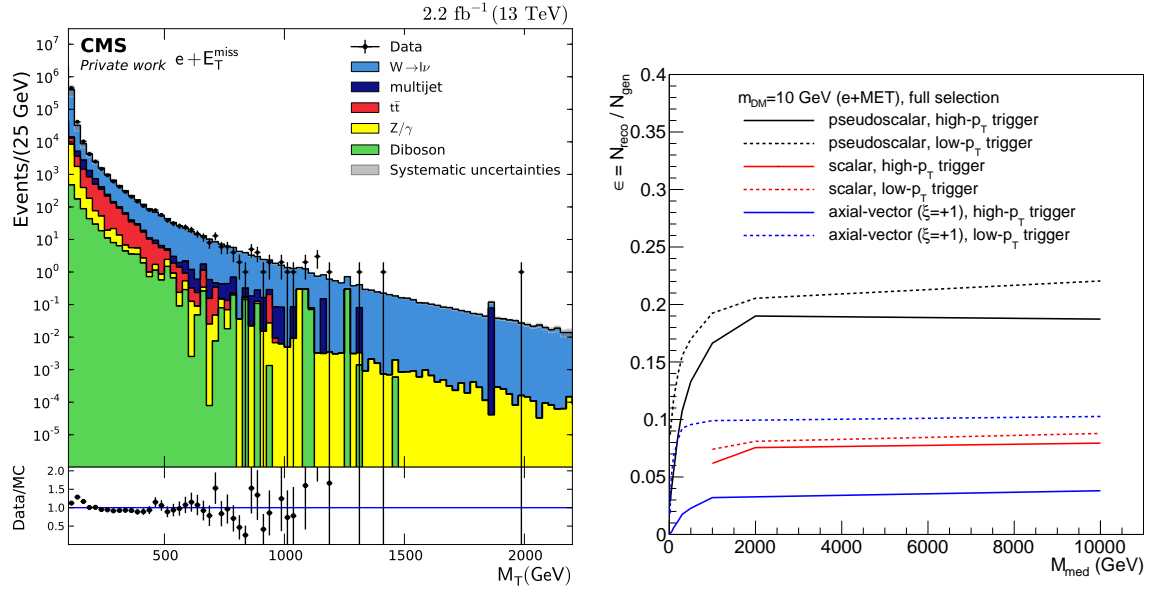


Figure 5.15: Left: M_T distribution after low- p_T trigger selection and after all applied cuts. Right: signal reconstruction efficiency for different coupling types and a low- p_T and high- p_T trigger.

Axial-vector coupling mediator model

M_{med} -dependent upper expected and observed 95% CL exclusion limits for an axial-vector coupling mediator model are shown in Fig. 5.16 for two exemplary DM masses of 1 GeV and 50 GeV. Destructive interference ($\xi = +1$) and a fixed DM coupling strength of $g_{DM} = 1$ is considered. For the expected 95% CL exclusion limit, the $\pm 1\sigma$ and $\pm 2\sigma$ bands are shown in green and yellow color bands, respectively. The theoretical production cross section determined from Madgraph5 calculations is shown for different mediator widths. A minimal mediator width using either $g_{SM} = 0.25$ or $g_{SM} = 1.0$ and both a broad ($\Gamma_{\text{med}} = M_{\text{med}}/3$) and narrow width approximation ($\Gamma_{\text{med}} = M_{\text{med}}/8\pi$) are considered. For $m_{DM} = 1$ GeV the resonant enhancement for on-shell mediator production is visible throughout the considered mediator mass range, while for $m_{DM} = 50$ GeV both off- and on-shell mediator production can be seen.

In order to evaluate the overall parameter reach of the considered simplified model, the lowest excluded production cross section σ_{excl} for all intersections of the theoretical production cross section with the observed 95% CL exclusion limit is determined for all available pairs of (M_{med}, m_{DM}) . If possible, the accompanying intersections with the expected 95% CL exclusion limit as well as the ± 1 expected 95% CL limit bands are determined. Of all considered signal samples, σ_{excl} denotes then the lowest and therefore best excluded production cross section. To evaluate the parameter reach in the simplified model parameter space, a two-dimensional representation is shown in Fig. 5.17-left. For each point (M_{med}, m_{DM}) indicated in the figure, the production cross section for the parameter set $(M_{\text{med}}, m_{DM}, g_{SM}, g_{DM})$ has been determined. A nearest-neighbor interpolation is performed to include the space between the calculated mass points, which is shown as a heatmap visualization. The decline in production cross

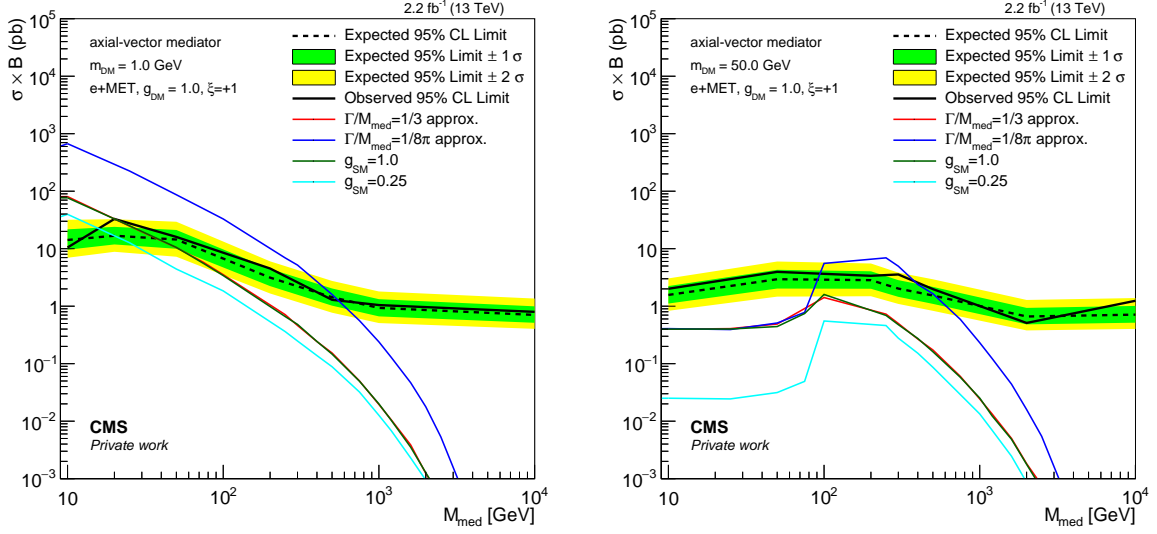


Figure 5.16: M_{med} -dependent upper expected and observed exclusion limits for an axial-vector coupling mediator model. Left: $m_{DM} = 1$ GeV, right: $m_{DM} = 50$ GeV.

section is visible for subsequent heavier M_{med} and m_{DM} , as well as a sharp decrease for the off-shell mediator production. The best excluded production cross sections σ_{excl} corresponding to the observed and expected 95% CL exclusion limit are included as contours, indicating their reach in the parameter space. For the narrow width approach using $\Gamma_{\text{med}}/M_{\text{med}} = 1/8\pi$, mediator masses up to 550 GeV and dark matter masses up to 175 GeV can be excluded.

Fig. 5.17-right adds further contours with different corresponding mediator widths. It becomes apparent that for destructive interference ($\zeta = +1$), the sensitivity is limited for broad mediator widths.

The effect of quark interference for $\zeta = 0, -1$ is included in Fig. 5.18. Due to the enhanced cross section especially for constructive interference ($\zeta = -1$), the sensitivity of the analysis is increased. While a minimal width using $g_{SM} = 0.25$ yields excluded mediator masses of $M_{\text{med}} \lesssim 1.25$ TeV, the upper bound of excluded mediator masses rises as high as $M_{\text{med}} \lesssim 2.25$ TeV for a narrow width approach using $\Gamma_{\text{med}} = M_{\text{med}}/8\pi$.

The influence of the optimization strategies discussed in Ch. 5.12.5 is evaluated. Fig. 5.19-left shows the simplified model parameter reach utilizing a low- p_T trigger with a decreased minimum transverse lepton momentum $p_T > 35$ GeV. In Fig 5.19-right optimized M_T -dependent kinematic cut functions have been used. The systematic uncertainty is increased in the low- M_T region as visible in Fig. 5.15-left, which becomes accessible by using the low- p_T trigger. Compared to the original approach shown in Fig. 5.17-right, the optimization strategies do not increase the analysis sensitivity. This finding also holds true for other mediator coupling types.

The parameter reach for an axial-vector coupling mediator model and Majorana DM is shown in Fig. 5.20. In the case of Majorana DM, the theoretical production cross section differs by a factor of two compared to Dirac DM [66,67]. Considering the narrow width approach, mediator masses up to 2.5 TeV can be excluded for $\zeta = -1$ with excluded

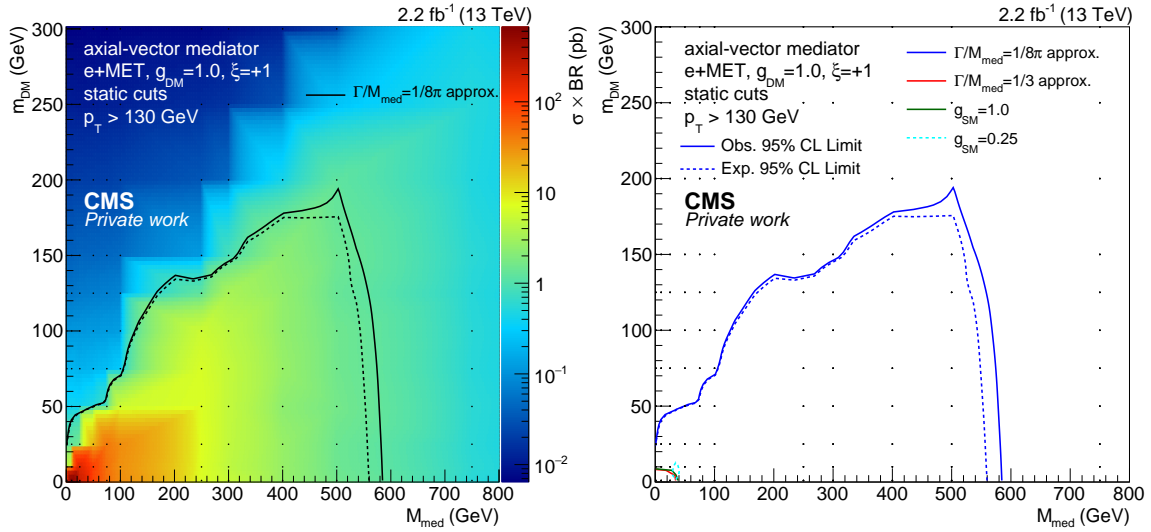


Figure 5.17: Two-dimensional representation of the production cross section in the $M_{\text{med}}-m_{\text{DM}}$ plane for an axial-vector coupling simplified model. Left: heatmap visualization of the simplified model production cross section interpolation with contours indicating the best excluded production cross section corresponding to the observed and expected 95% CL exclusion limit. Right: added contours corresponding to 95% CL exclusion limits using different mediator widths.

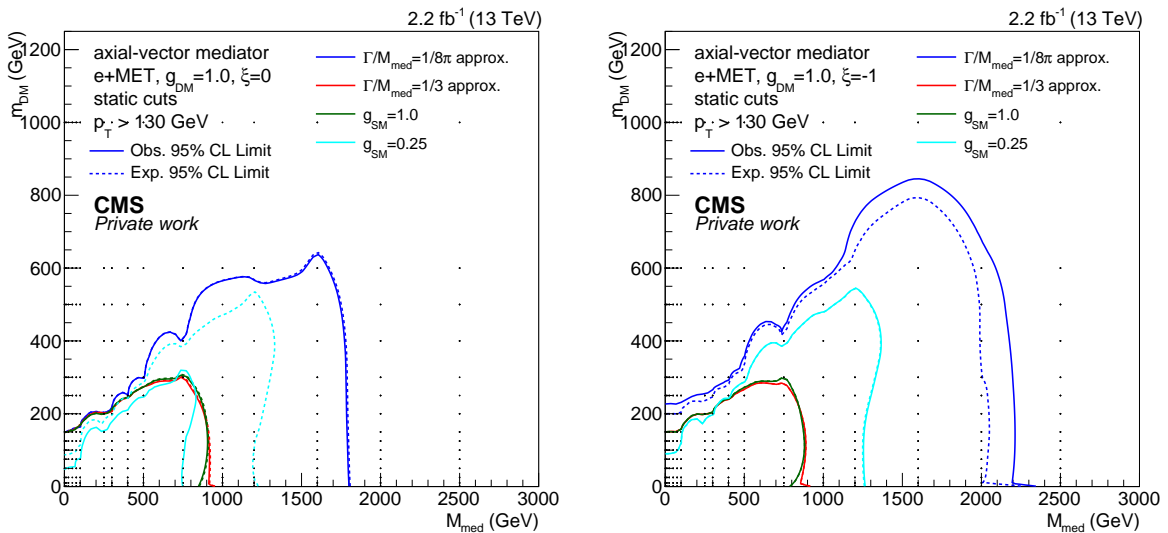


Figure 5.18: Simplified model parameter reach for an axial-vector coupling mediator and different interference cases. Left: $\xi = 0$, right: $\xi = -1$.

dark matter masses up to 850 GeV. For $\xi = +1$, mediator masses up to 750 GeV and dark matter masses up to 225 GeV can be excluded.

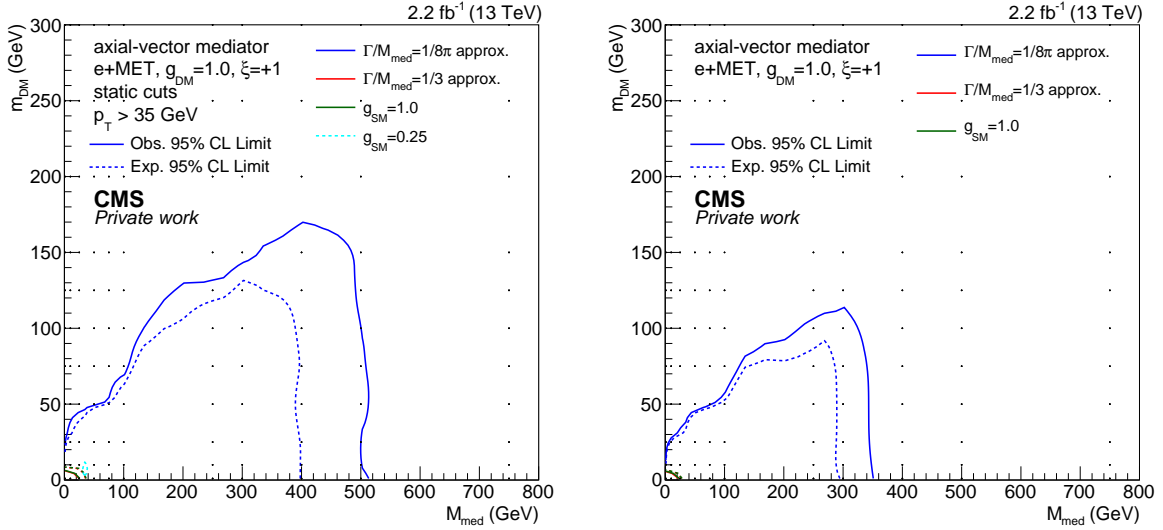


Figure 5.19: Impact of optimization methods on the simplified model parameter reach, shown for axial-vector coupling with $\zeta = +1$. Left: Inclusion of low- p_T events with $p_T > 35$ GeV using a low- p_T trigger. Right: m_T -dependent optimized kinematic cuts.

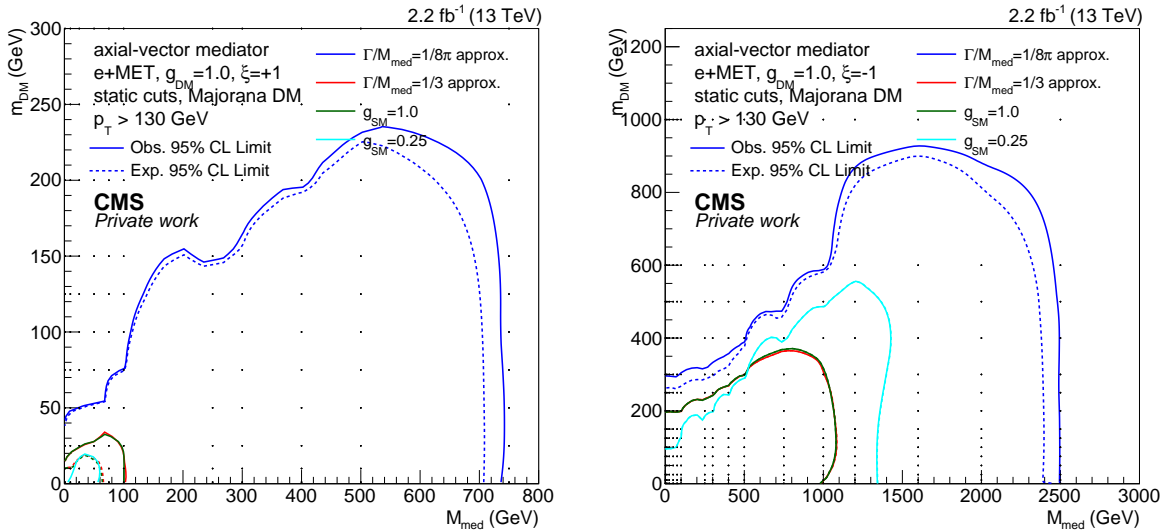


Figure 5.20: Simplified model parameter reach for an axial-vector coupling mediator model with Majorana dark matter and different interference cases. Left: $\zeta = +1$, right: $\zeta = -1$.

Vector coupling mediator model

For vector coupling mediator models, similar 95% CL exclusion limits are expected as for axial-vector coupling, as both couplings yield comparable production cross sections as well as a comparable shape of the M_T distribution. Fig. 5.21-left shows upper expected and observed exclusion limits for a fixed $m_{DM} = 1$ GeV. Best exclusion limits σ_{excl} are determined for all considered values of m_{DM} and are shown for $\zeta = +1$ in Fig. 5.21-right for different mediator widths and couplings g_{SM} . The resulting parameter

reach is comparable to the axial-vector coupling model.

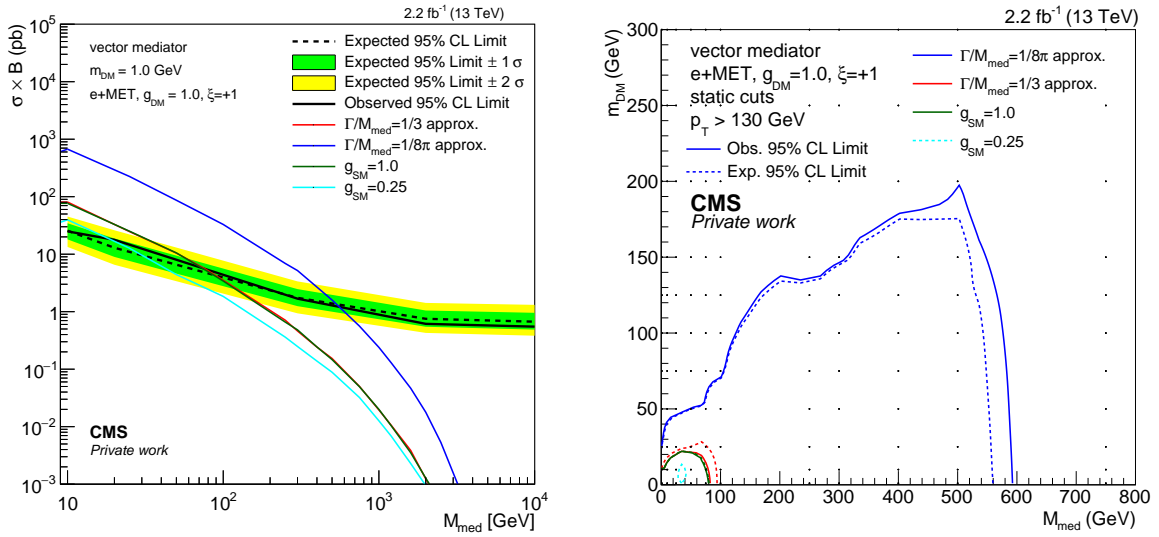


Figure 5.21: Left: M_{med} -dependent upper expected and observed exclusion limits for a vector coupling mediator model and an exemplary DM mass of $m_{\text{DM}}=1$ GeV. Right: simplified model parameter reach for a vector coupling mediator.

Quark interference with $\zeta = 0, -1$ is considered in Fig. 5.22, which yields similar results as for axial-vector coupling shown in 5.18.

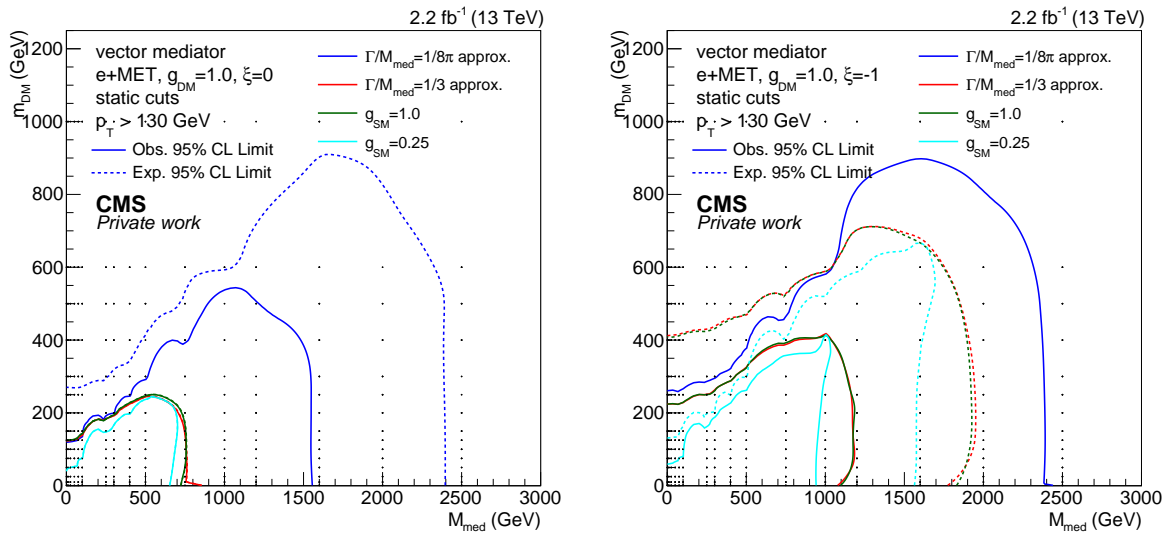


Figure 5.22: Simplified model parameter reach for a vector coupling mediator and different interference cases. Left: $\zeta = 0$, right: $\zeta = -1$.

Scalar and pseudoscalar mediator models

The determination of the production cross section using the JHU generator is independent of m_{DM} , as the decay of the mediator is performed by an external program which

does not modify the cross section. Therefore for a scalar and pseudoscalar coupling mediator model the best obtained bounds are shown. For a scalar coupling mediator model, Fig. 5.23-left shows the best expected and observed 95% CL limits. Here, mediator masses up to 150 GeV and dark matter masses up to 50 GeV can be excluded. In the case of a pseudoscalar coupling mediator model, Fig. 5.23-right shows the best expected and observed 95% CL limits. Here, dark matter masses up to $m_{DM} \lesssim 150$ GeV corresponding to $M_{\text{med}} \lesssim 400$ GeV can be excluded.

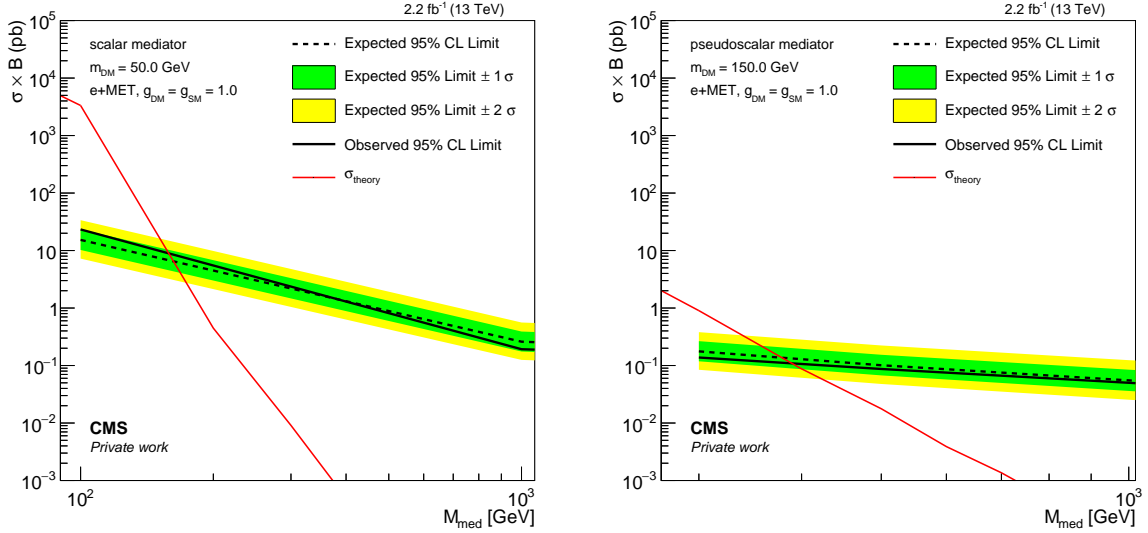


Figure 5.23: Left: Simplified model parameter reach for a scalar coupling mediator. Right: pseudoscalar mediator

5.12.7 Comparison with direct- and indirect-detection searches

In the following, a subset of the results presented above will be compared to bounds on the dark matter scattering cross section set by direct- and indirect-detection experiments introduced in Ch. 2.3.3. In particular, axial-vector and vector coupling with destructive interference ($\zeta = +1$) is considered. Upper exclusion limits derived using axial-vector coupling are compared to spin-dependent searches, while results obtained using vector coupling are compared to spin-independent searches. The comparison depends on the considered dark matter production mechanism, as lower bounds determined with collider searches are only valid for the specific considered model and considered parameter set, while direct- and indirect-detection experiments may remain valid for different production models as well [18].

Exclusion limits derived using scalar and pseudoscalar coupling mediator models may in principle also be compared to spin-independent and spin-dependent searches respectively. However due to the independence of the production cross section determination on m_{DM} the following presentation is only shown for vector and axial-vector coupling.

The upper 95% CL exclusion limits presented in Ch. 5.12.6 are translated to DM-nucleon scattering cross sections following the official recommendation from the LHC

Dark Matter Working Group [18]. For the spin-independent case, the scattering cross section is given by

$$\sigma_{\text{SI}} = \frac{f^2(g_{SM})g_{DM}^2\mu_{n\chi}^2}{\pi M_{\text{med}}^4} \quad (5.12.1)$$

with the reduced mass of the DM-nucleon system

$$\mu = \frac{m_n m_{DM}}{m_n + m_{DM}}. \quad (5.12.2)$$

Taking N_c and the universal coupling strength g_{SM} into account, the coupling between the mediator and the nucleon $f(g_{SM})$ becomes $f(g_{SM}) = 3g_{SM}$.

For the spin-dependent case, the scattering cross section is given by

$$\sigma_{\text{SD}} = \frac{3f^2(g_{SM})g_{DM}^2\mu_{n\chi}^2}{\pi M_{\text{med}}^4} \quad (5.12.3)$$

in which the coupling $f(g_{SM})$ now depends on the type of nucleon considered in the scattering process. For protons and neutrons, the term is given by

$$f^{p,n}(g_{SM}) = \Delta_u^{p,n} g_u + \Delta_d^{p,n} g_d + \Delta_s^{p,n} g_s \quad (5.12.4)$$

with values for Δ_u^p provided by [9]

$$\Delta_u^p = \Delta_d^n = 0.84 \quad (5.12.5)$$

$$\Delta_d^p = \Delta_u^n = -0.43 \quad (5.12.6)$$

$$\Delta_s = -0.09. \quad (5.12.7)$$

Precise determination of the nucleon spin include contributions of strange quark-anti-quark pairs, even though nucleons have zero strangeness [68]. Strange quarks affect the nucleon spin through their presence as sea quarks. Assuming equal coupling to the quark flavours the coupling term now becomes $f(g_{SM}) \approx 0.32 g_{SM}$ [18].

Fig. 5.24 shows the upper 90% CL limits on the DM-nucleon cross section determined by direct- and indirect-detection searches and the 95% CL collider limits presented in this analysis for both the spin-independent (top) and spin-dependent case (bottom). The exclusion limits derived in Ch. 5.12.6 for different mediator widths including the narrow width approach using $\Gamma_{\text{med}} = M_{\text{med}}/8\pi$ and different coupling strengths $g_{SM} = 0.25$ and $g_{SM} = 1.0$ have been translated using formulas 5.12.1 and 5.12.3. For the spin-independent case, results from the LUX, CDMS and CRESST collaborations are shown. For spin-dependent DM-proton scattering, the figure includes the results from the direct-detection PICO experiment as well as specific indirect-detection annihilation channels from the Ice-Cube and Super-Kamiokande experiments ($\chi\bar{\chi} \rightarrow t\bar{t}$ and $\chi\bar{\chi} \rightarrow b\bar{b}$, respectively).

The comparison is valid under the assumption that χ is the sole constituent of dark matter in the universe. Experimental bounds set by direct and indirect searches will weaken if more constituents have to be considered, unlike bounds set by collider searches [18].

For spin-independent searches, the CMS search results derived in the previous section surpass the lower bounds set by the direct- and indirect-detection experiments for $m_{DM} < 2$ GeV and a narrow width approach. Otherwise the LUX, CDMS and CRESST experiments set the lowest bounds on the DM-nucleon scattering cross section. For the spin-dependent case, the collider search exceeds the bounds set by the (in)direct detection experiments for DM masses up to 200 GeV. This holds true in particular for light dark matter with $m_{DM} \lesssim 5$ GeV, as this region is inaccessible to the spin-dependent direct- and indirect-detection experiments.

5.13 Results

In this chapter, 2.2 fb^{-1} of recorded data with CMS in 2015 at $\sqrt{s} = 13$ TeV have been analyzed in the transverse mass distribution for the mono-electron channel. The final M_T distribution exhibits a deficit of data with respect to the SM background contribution for $M_T \gtrsim 700$ GeV. Two interpretations of physics beyond the Standard Model have been investigated and 95% CL exclusion limits have been determined.

The production of a W' boson can be excluded for W' masses up to 3.75 TeV using the single-electron channel. The combination of the results presented in this thesis with the single-muon channel allows the exclusion of even heavier W' masses up to 4.4 TeV [49].

Simplified models have been used to model the dark matter production in Run-2. The simplified model parameter reach has been explored for axial-vector, vector, scalar and pseudoscalar couplings.

For axial-vector and vector coupling, mediator masses up to 550 GeV and dark matter masses up to 175 GeV can be excluded using a narrow width approach ($\xi = +1$). The exclusion limits have been compared to (in)direct detection experiments. For spin-independent searches, the mono-electron CMS search results exceed the bounds set by (in)direct searches for light dark matter $m_{DM} < 2$ GeV. The CMS search is competitive in the spin-dependent case, in which (in)direct detection bounds are exceeded for a large range of $m_{DM} < 200$ GeV.

Simplified models provide an opportunity to study scalar and pseudoscalar coupling mediators. Mediator masses up to 150 GeV with dark matter masses up to 50 GeV can be excluded for scalar coupling. For pseudoscalar coupling, mediator masses up to 400 GeV and dark matter masses up to 150 GeV can be excluded.

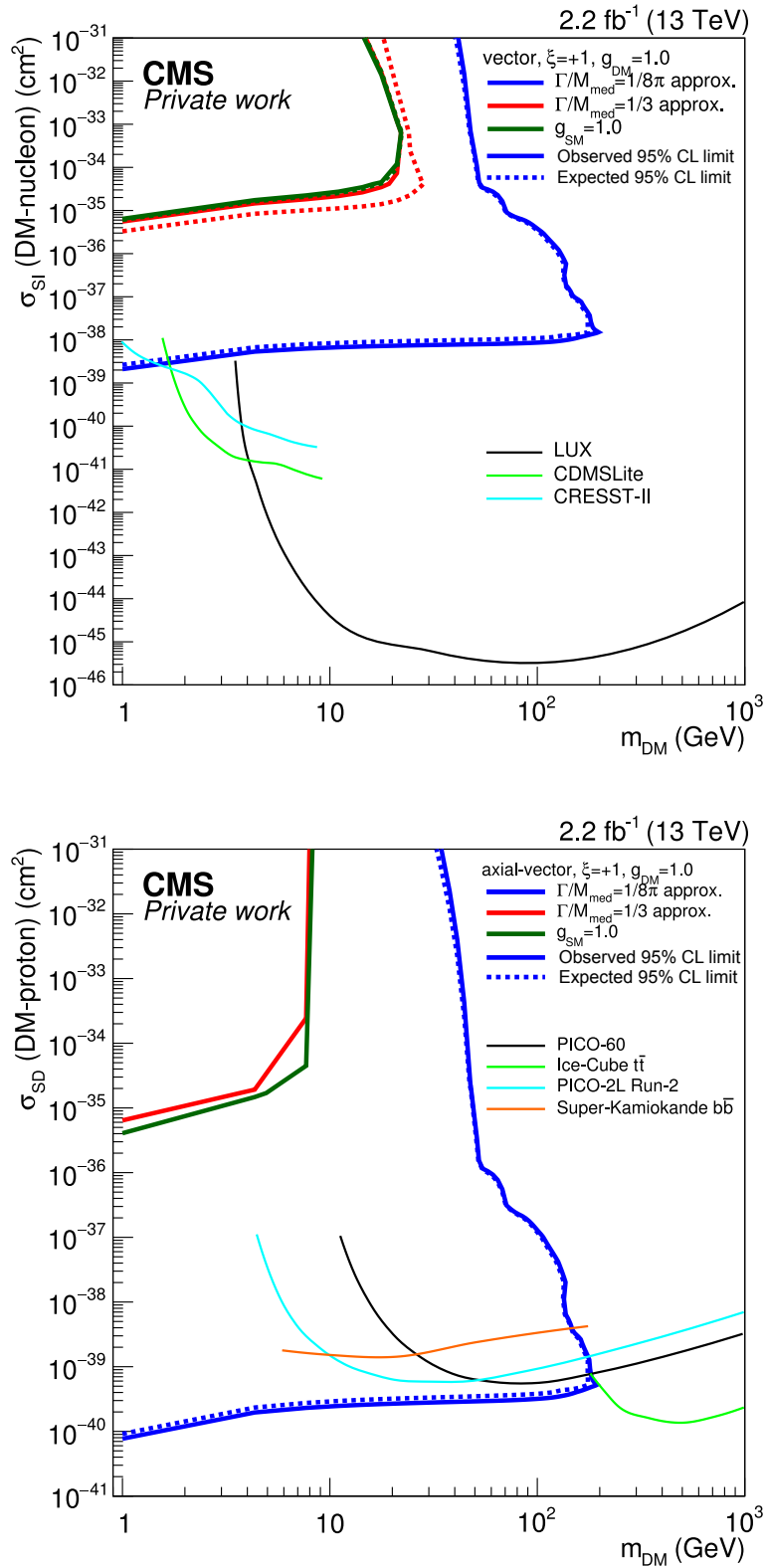


Figure 5.24: Comparison of 90% CL exclusion limits from (in)direct detection searches and 95% CL exclusion limits from the mono-electron CMS analysis. Shown is the spin-independent DM-nucleon and spin-dependent DM-proton cross section limit dependent on m_{DM} . Top: spin-independent searches corresponding to vector coupling mediator models. Bottom: spin-dependent searches corresponding to axial-vector coupling mediator models. Direct- and indirect-detection scattering cross section bounds from [18].

Chapter 6

Impact of the High-Luminosity LHC and upgraded CMS detector on dark matter searches

In the previous chapter, exclusion limits on the dark matter parameter space have been determined at a center-of-mass energy of 13 TeV using an integrated luminosity of 2.2 fb^{-1} , which corresponds to the available certified data from the year 2015 for analyses involving missing transverse energy in Run-2. The integrated luminosity is expected to further increase starting in 2016 up to 300 fb^{-1} in the following years, with the center-of-mass energy reaching 14 TeV.

The High-Luminosity LHC (HL-LHC) upgrade project is designed to increase the integrated luminosity up to 3000 fb^{-1} with a run period of ten years. In this chapter, the impact of the increased luminosity and center-of-mass energy on the DM search in the mono-electron channel is investigated. The increased luminosity is expected to enhance the sensitivity of the dark matter search and thus the reach in parameter space for new physics beyond the standard model.

In the following, the HL-LHC project is discussed with a focus on the accompanying CMS detector upgrades. The project itself is documented in the Technical Proposal document [69]. The simulation methods of the upgraded detector are presented and expected 95% CL exclusion limits of the DM search in the mono-electron channel are extrapolated to the upgraded conditions. Selected results of this chapter have been included in the Technical Proposal itself.

6.1 The High-Luminosity LHC project

Fig. 6.1 shows the timeline of the projected LHC performance. Currently the LHC operates in Run-2 of Phase-I, with the next long shutdown scheduled for 2018 - 2019 (LS2). In this timeframe, the luminosity of the LHC will be increased beginning with a modified bunch formation in the Proton Synchrotron. Improvements to the injector chain will yield bunches with higher intensity and lower emittance, thus providing an integrated luminosity of $\mathcal{L}_{\text{int}} \approx 300 \text{ fb}^{-1}$ by 2023 [69]. Further modifications to increase

the luminosity are scheduled for the LS3, as by 2023 the beam-focussing quadrupoles at the collision region will have to be replaced due to radiation damage. After LS3, Phase-II of the HL-LHC is expected to begin. Modifications to the CMS detector components will be required to accommodate the very high luminosity conditions, which are described in the following chapter.

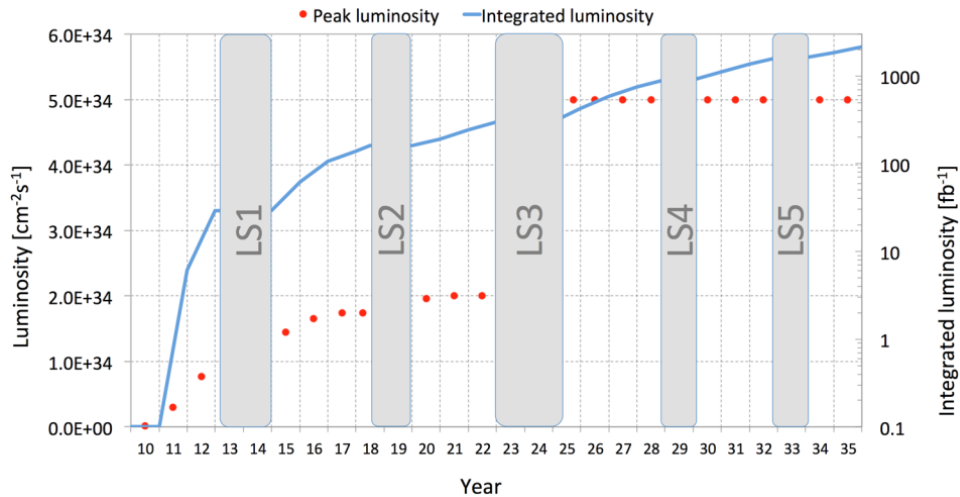


Figure 6.1: Projected LHC performance showing peak luminosity (left axis, red color) and integrated luminosity (right axis, blue color) over time. Long shutdown periods are denoted as "LS". The HL-LHC project is expected to be prepared in the LS3 period, after which the integrated luminosity is planned to increase up to 3000 fb^{-1} . Figure from [69].

6.2 CMS detector upgrades

An overview of the CMS upgrades is given in Ch. 1.5 of [69], on which this section is based. The integrated design luminosity of the CMS detector is $\mathcal{L}_{\text{int}} = 300 \text{ fb}^{-1}$. To maintain detector performance up to this integrated luminosity, Phase-I upgrades according to the Phase-I Technical Proposal [70] are performed, which affect the pixel detector, the hadron calorimeter and the hardware trigger.

As the CMS detector reaches its integrated design luminosity goal, simulations show that detector upgrades will become necessary after $300 - 500 \text{ fb}^{-1}$, as the detector components experience aging effects due to radiation damage. As pile-up is increased from 25 simultaneous interactions per bunch crossing at the beginning of Run-2 to approximately 140 simultaneous interactions in the HL-LHC phase, the upgraded tracker and endcap calorimeter components are furthermore optimized for these high pile-up conditions. The increased pile-up is a necessity of higher luminosity which cannot be avoided, as the number of bunches remains fixed at ≈ 2800 per beam.

The radiation damage is due to charged particles produced at a high rate of $5 \cdot 10^9 / \text{s}$ in Phase-II in the pp collisions. Of these charged particles, pions are mostly relevant to this process as they ionize the detector material. Photons from π^0 decay further produce electromagnetic showers in the calorimeter. Pions also may induce nuclear

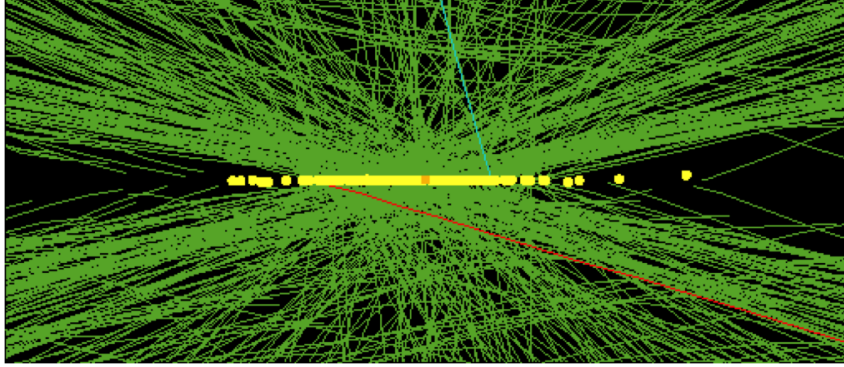


Figure 6.2: Exemplary event from Run-1 with 78 reconstructed vertices illustrating the effect of pile-up. Figure taken from [69].

interactions in the calorimeters, producing cascades from which particles also may be backscattered to other detector components. In the tracker, the radiation produces defects in the silicon lattice, thus producing leakage currents or trapped charge carriers which decreases the detector output signal. Considering the electromagnetic calorimeter, which is comprised of $PbWO_4$ crystals, and in the case of the hadron calorimeter, brass and plastic scintillating tiles, the main radiation exposure effect concerns the embedded wavelength-shifting fibers, as they exhibit a loss in transmission by more than 90% in high-luminosity simulations.

The increased pile-up also has to be addressed during the Phase-II upgrade, which degrades both the trigger performance and the offline reconstruction.

Radiation damage simulations show that for Phase-II the silicon tracker and endcap calorimeters have to be replaced. The silicon tracker will have to be completely replaced in LS3. The new silicon tracker will have four times the granularity as the current installed tracker. The pixel system will further feature up to ten additional pixel disks which allow extended coverage up to $|\eta| \approx 4$. The calorimeter endcaps will be replaced by the High Granularity Calorimeter (HGC). The muon endcaps in the region $1.5 \leq |\eta| \leq 2.4$ are not supported by redundant components, thus additional muon chambers will be installed to maintain a good trigger performance. The additional installed chambers will consist of gas electron multiplier chambers in the vicinity of the magnetic field, and resistive plate chambers in the outer regions. Overall coverage will be extended with the installation of the additional chambers to $\eta \approx 3$.

Other components included in the upgrade process are the beam radiation protection and luminosity measurement, the trigger system, the data acquisition system and software as well as computing.

6.3 Simulation of Phase-II conditions

To simulate Phase-II detector conditions with increased coverage $|\eta| \approx 4$, a more granular silicon tracker as well as considering ageing effects of the components, both a full and a parametrized simulation of the CMS detector are utilized. The full detector simulation based on GEANT4 as presented in Ch. 4 is extended to accommodate the Phase-II

detector with an increased pile-up of 140 interactions. Additionally, a parametrized detector simulation using DELPHES is used. The DELPHES configuration cards utilized in [71] are used to model the Phase-I and Phase-II detector conditions. For Phase-I, ageing effects of the detector components are considered as well. The configuration cards can be found in Sec. 9.2 of the appendix .

The physics object performance in the full simulation, in particular the electron and E_T^{miss} performance for Phase-II is discussed in [69].

6.4 Dark matter exclusion limits

In Ch. 5 exclusion limits on dark matter have been determined using simplified models. Here, expected exclusion limits on the production cross section are extrapolated for luminosities up to 3000 fb^{-1} using the EFT approach. The EFT-derived expected limits are shown in Fig. 6.3-left and serve as a conservative indication for the simplified model parameter reach for Phase-II, as the EFT approach corresponds to the heavy mediator mass region.

6.4.1 Effective field approach

Extrapolated 95% CL exclusion limits on the dark matter production cross section times branching ratio using the EFT approach have been determined in a previous extrapolation study in the mono-W channel for Phase-II by [71]. This study discusses multiple interpretations beyond the SM including the dark matter production modelled by the EFT approach. The 95% CL exclusion limit on the production cross section times branching ratio are shown in Fig. 6.3-left. A constant dark matter mass of $m_{DM} = 10 \text{ GeV}$ has been used. The extrapolation is shown for integrated luminosities ranging up to high-luminosity conditions of 3000 fb^{-1} and for the different interference cases. Comparable excluded cross sections for $\zeta = 0$ and $\zeta = -1$ result from similar signal efficiencies.

Fig. 6.3-right shows the extrapolated exclusion limit on the contact interaction scale Λ , which is obtained by a translation of the expected limit on the process cross section given by

$$\Lambda_{\text{expected}}^4 = \frac{\sigma_{\text{theory}} \cdot \Lambda_{\text{theory}}^4}{\sigma_{\text{expected}}} \quad (6.4.1)$$

with the production cross section σ_{theory} and Λ_{theory} as well as the expected exclusion limit on the cross section σ_{expected} .

6.4.2 Simplified models

The sensitivity of a simplified model with an axial-vector coupling mediator presented in Ch. 2.4.2 is estimated. An interaction scale Λ of $\approx 5000 \text{ GeV}$ corresponding to

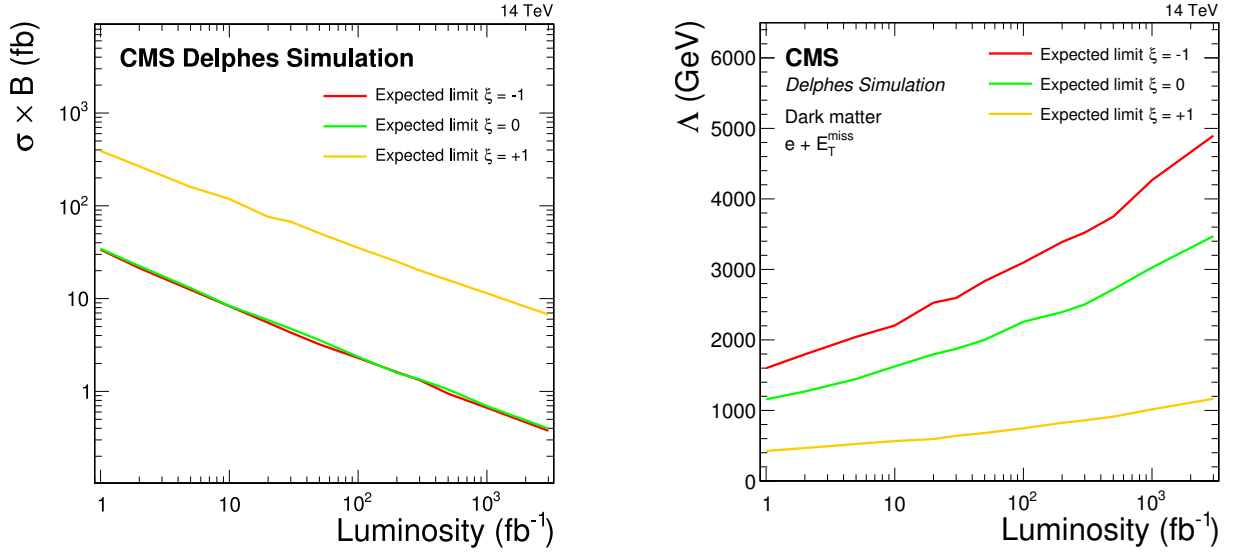


Figure 6.3: Left: extrapolated 95% CL exclusion limits on the DM production cross section times branching ratio using the EFT approach with $m_{DM} = 10$ GeV and different values of ζ . The extrapolation is shown for luminosities up to 3000 fb^{-1} . Right: extrapolated exclusion limits on the contact interaction scale Λ for different values of ζ as a function of the integrated luminosity. Figures from [71].

3000 fb^{-1} for constructive interference as seen in Fig. 6.3-right falls into the region where both DM production models are valid, thus the EFT approach and simplified models yield comparable results.

Simplified model process cross sections for pairs of (m_{DM}, M_{med}) using a narrow width approach ($\Gamma_{\text{med}} = M_{\text{med}}/8\pi$) with couplings $|g_{DM}| = |g_{SM}| = 1$ are determined. Exclusion limits on the process cross sections times branching ratio from Fig. 6.3-left are shown as solid contour curves in Fig. 6.4 for the interference cases $\zeta = \pm 1$. For $\zeta = 0$, the parameter reach lies between $\zeta = \pm 1$ and exclusion limits are included in Sec. 9.3 of the appendix. The resulting projections are compared to the 90% CL limits of the mono-jet analysis and the neutrino background published in [30].

Both analyses employ a DELPHES detector simulation. The mono-jet analysis scales the $\sqrt{s} = 8$ TeV limits to the different scenarios assuming that the underlying performances of the CMS mono-jet search in terms of signal efficiency and background suppression remains unchanged [30]. The mono-jet projection for high-luminosity conditions of 3000 fb^{-1} is in close proximity of the neutrino background boundary.

Considering the mono-electron channel, constructive interference yields the highest projected reach in both mediator mass and DM mass. In this case and for an integrated luminosity of 300 fb^{-1} , the LHC is expected to probe beyond the direct-detection bounds, whose ultimate reach is set by the neutrino background. The high-luminosity LHC with 3000 fb^{-1} is expected to probe even further beyond a mediator mass of 5500 GeV or a DM mass above 2000 GeV. Different interference cases yield a lowered projected reach. The projected reach is significantly decreased for destructive interference, with excluded mediator masses expected to be lower than excluded mono-jet

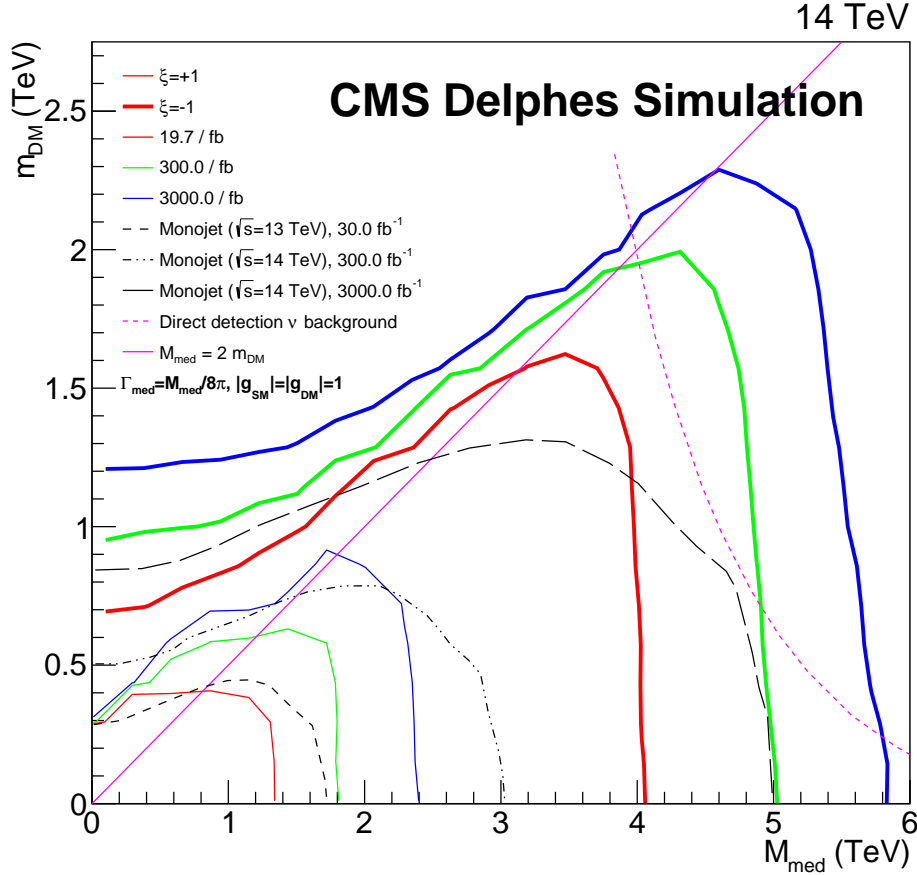


Figure 6.4: Production cross sections for grid pairs of $(M_{\text{med}}, m_{\text{DM}})$ determined from a simplified model for axial-vector coupling for $\xi = \pm 1$. For $\xi = 0$, refer to Sec. 9.3 of the appendix. The solid contours indicate projected 95% CL limits from the mono-electron analysis, compared to the projected 90% CL limits from mono-jet analysis results [25] marked as dotted contours. In both analyses the projected cross section limits have been calculated using a DELPHES simulation. The transition region between on- and off-shell mediator production is indicated as a solid magenta line. The neutrino background, also from [25], which is the irreducible background for direct-detection experiments, is shown as a dashed magenta curve.

analysis projections.

Compared to the bounds set on Λ obtained by the EFT approach, the projected reach of the mediator mass in the simplified model for constructive interference is increased. Fig. 6.3-right shows a limit of $\Lambda \approx 5000$ GeV for 3000 fb^{-1} , whereas for the same luminosity a mediator mass of $M_{\text{med}} \approx 5800$ GeV is within the projected reach in the case of $\xi = -1$. The latter however is heavily dependent on the mediator width Γ_{med} , as larger values of Γ_{med} decrease the projected reach of M_{med} .

6.4.3 Sensitivity to detector performance

In the following, the detector performance for both Phase-I and Phase-II including the “aged” scenario for Phase-I is discussed. Fig. 6.5-left shows the electron reconstruction efficiency for $\zeta = 0$ for both phases as well as ageing affecting the detector performance. A single electron selection has been applied, such that $200 \text{ GeV} < M_T < 250 \text{ GeV}$. Detector ageing effects become mostly apparent below $M_T < 1500 \text{ GeV}$ as shown in Fig. 6.5-right.

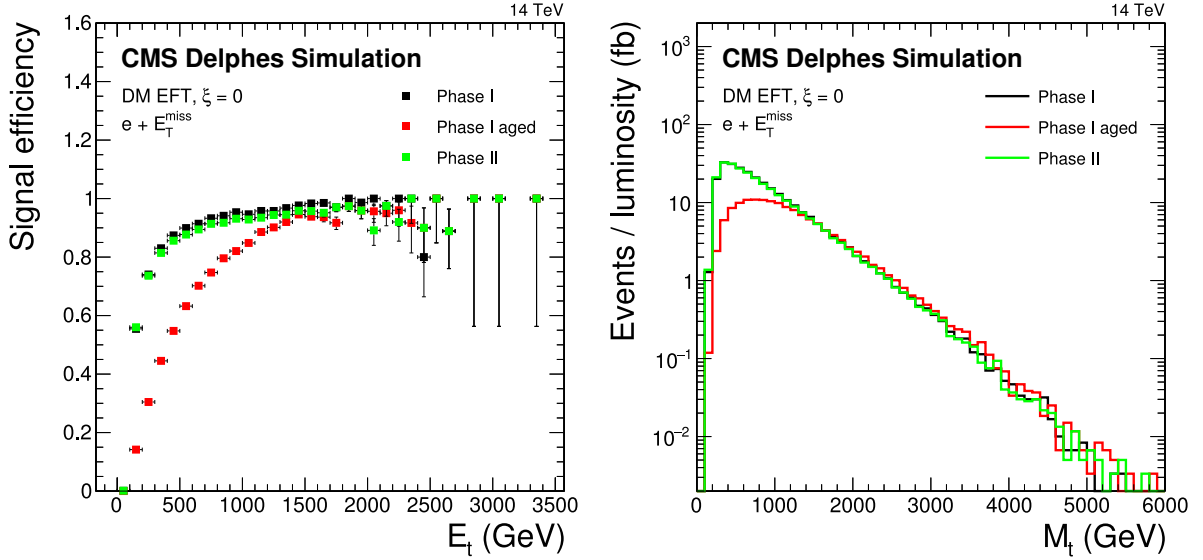


Figure 6.5: Detector performance for different scenarios including Phase-I “ageing” effects imposed on the tracker and endcap calorimeters. Left: signal efficiency for an axial-vector DM signal with a mass of $m_{DM} = 10 \text{ GeV}$ and $\zeta = 0$. Right: corresponding M_T spectrum. Figures from [71].

The sensitivity estimation of the simplified model presented in Sec. 6.4.2 is compared to the “aged” Phase-I scenario. Fig. 6.6 shows a comparison of the different scenarios with the “aged” Phase-I scenario, indicated as dashed contours for $\zeta = \pm 1$. For $\zeta = 0$, refer to Sec. 9.3 of the appendix. Aged detector conditions affect the projected reach of the considered simplified model. Considering constructive interference, the M_{med} sensitivity is decreased by $\approx 200 \text{ GeV}$ for 3000 fb^{-1} . This difference would require the Phase-II detector to record an additional luminosity of $\approx 1000 \text{ fb}^{-1}$ compared to the exclusion limit of the Phase-I “aged” detector.

6.4.4 Conclusion

The High-Luminosity LHC is expected to provide a significant increase in sensitivity of the dark matter search. For axial-vector coupling simplified models and a narrow width approach, it can potentially probe beyond heavy mediator masses of 2 TeV. Considering constructive quark interference, this parameter reach is extended above mediator masses of 5 TeV and dark matter masses above 2 TeV, which potentially probes beyond the neutrino background.

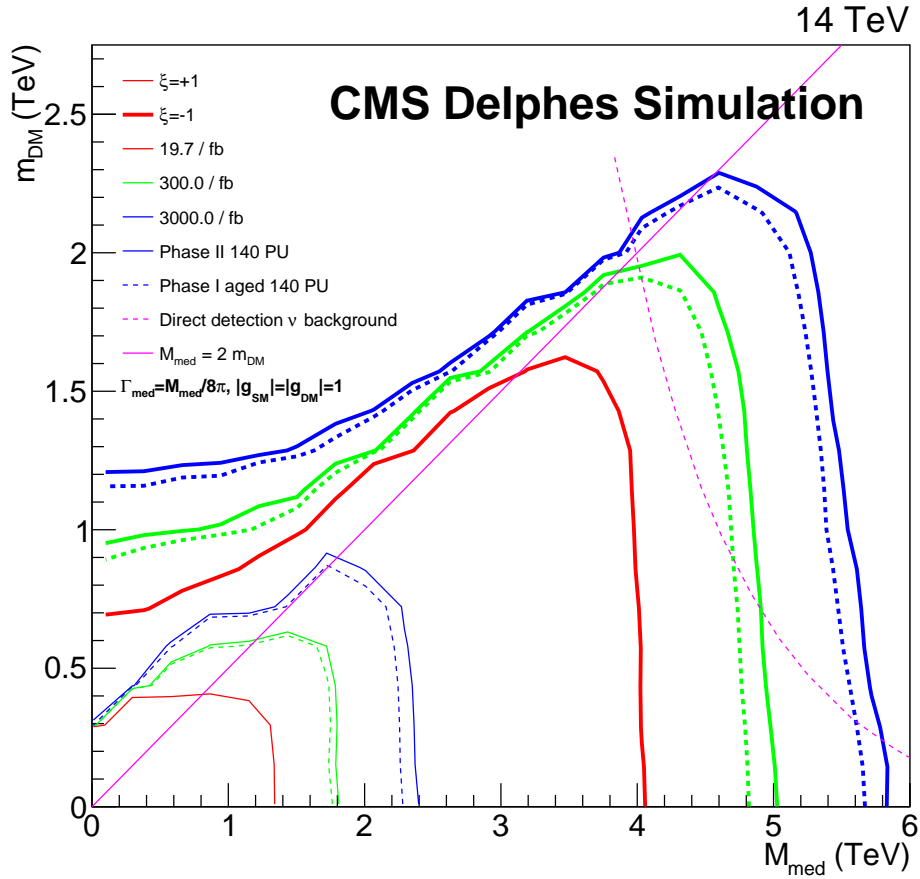


Figure 6.6: Production cross sections for grid pairs of $(M_{\text{med}}, m_{\text{DM}})$ determined from a simplified model for axial-vector coupling for $\xi = \pm 1$. For the $\xi = 0$, refer to Sec. 9.3 of the appendix. Contours indicate projected 95% CL limits derived by the EFT approach, of which solid contours represent Phase-II conditions and dashed contours indicate Phase-I “aged” conditions. The transition region between on- and off-shell mediator production is indicated as a solid magenta line. The neutrino background, also from [25], which is the irreducible background for direct-detection experiments, is shown as a dashed magenta curve.

Chapter 7

Unitarity violation in quark interference models

This chapter discusses the limitations of the dark matter production models in the mono-W channel involving the effect of quark interference, as introduced in Ch. 2.4.1 and shown again in Fig. 7.1. The production cross section is significantly enhanced for constructive interference ($\zeta = -1$) and coupling to one quark flavour only ($\zeta = 0$), as shown in Fig. 2.12. During the writing of this thesis, multiple publications [19, 20, 21] showed that the enhancement in cross section is due to an unitarity-violating production of longitudinal W bosons. This chapter discusses the implications for the analysis based on these findings.

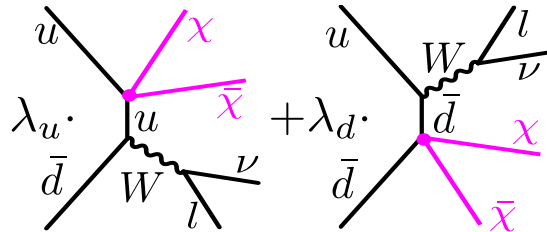


Figure 7.1: Feynman diagrams with the same initial and final state showing the effect of quark interference in the mono-W channel as shown in Ch. 2.4.1. The DM production mechanism may couple differently to the SM quarks, as indicated by the coupling strength λ_i .

The concept of quark interference in the mono-W channel has been first proposed in [26]. BELL et al. showed that the interference cases $\zeta \neq +1$ give rise to a production of longitudinal W bosons when considering the EFT approach [19]. This causes the violation of the Ward identity, and as a consequence, violates the SM weak gauge symmetry. This finding has been extended to simplified models involving quark interference as well [20]. The most recent publication at the time of writing does not allow interference for simplified models [21], however presents possible solutions to the problem short of not considering the effect of quark interference altogether. A proposed solution is to consider a small difference in coupling values to each quark type only, which however significantly reduces the enhancement of the production cross section. The sensitivity of the mono-W channel is thus limited when considering an axial-vector and a vector coupling mediator. Another proposed solution is to intro-

duce an additional interaction between the spin-1 mediator and the W boson, which is proportional to the difference between the left-handed couplings λ_u^L and λ_d^L [21].

In order to provide a comparison to other analyses, the results of this analysis have been presented for models involving quark interference $\xi = -1$ and $\xi = 0$ as well. They have however to be treated with caution. A future analysis may incorporate the dark matter production with an extended simplified model as proposed in [21], therefore retaining the effect of quark interference without violating unitarity. Both approaches may then be compared in terms of reach in simplified model parameter space.

Chapter 8

Conclusion

In this thesis, data collected in 2015 by the CMS experiment at $\sqrt{s} = 13$ TeV have been analyzed in the mono-electron channel. Deviations in transverse mass from the Standard Model prediction have been interpreted in terms of both a new vector boson W' and dark matter. The transition of the dark matter production mechanism from the effective field approach used in Run-1 to simplified models utilized in Run-2 has been presented.

While no evidence for new physics has been found, constraints on the mass of the new vector boson and dark matter parameter space have been set. A SSM W' interpretation can be excluded for W' masses below 3.75 TeV using the single-electron channel. The combination of the results presented in this thesis with the single-muon channel allows the exclusion of even heavier W' masses up to 4.4 TeV.

Concerning dark matter, simplified models with different coupling structures have been investigated. For axial-vector and vector coupling, mediator masses up to 550 GeV and dark matter masses up to 175 GeV can be excluded using a narrow width approach ($\xi = +1$). The exclusion limits have been compared to (in)direct detection experiments. For spin-independent searches, the mono-electron CMS search results exceed the bounds set by (in)direct searches for light dark matter $m_{DM} < 2$ GeV. The CMS search is competitive in the spin-dependent case, in which (in)direct detection bounds are exceeded for a large range of $m_{DM} < 200$ GeV.

Simplified models also provide an opportunity to study scalar and pseudoscalar coupling mediators. Mediator masses up to 150 GeV with dark matter masses up to 50 GeV can be excluded for scalar coupling. For pseudoscalar coupling, mediator masses up to 400 GeV and dark matter masses up to 150 GeV can be excluded.

The High-Luminosity LHC is expected to provide a significant increase in sensitivity of the dark matter search. For axial-vector coupling simplified models and a narrow width approach, it can potentially probe beyond heavy mediator masses of 2 TeV. Considering constructive quark interference, this parameter reach is extended above mediator masses of 5 TeV and dark matter masses above 2 TeV, which potentially probes beyond the neutrino background.

CHAPTER 8. CONCLUSION

Chapter 9

Appendix

9.1 Event displays

Fig. 9.1 shows the event display exhibiting the currently largest transverse mass M_T measured in the mono-electron channel.

9.2 DELPHES data cards

The following DELPHES cards have been used for the CMS detector upgrade studies presented in Ch. 6:

- `JetStudies_Phase_I_140PileUp_MuonResolutionInverse_rms_Eff96.tcl`
- `JetStudies_Phase_I_140PileUp_aged_MuonResolutionInverse_rms_Eff96.tcl`
- `JetStudies_Phase_II_140PileUp_conf4_MuonResolutionInverse_rms_Eff96.tcl`

The cards can be found at <https://github.com/vkutzner/upgradestudies>.

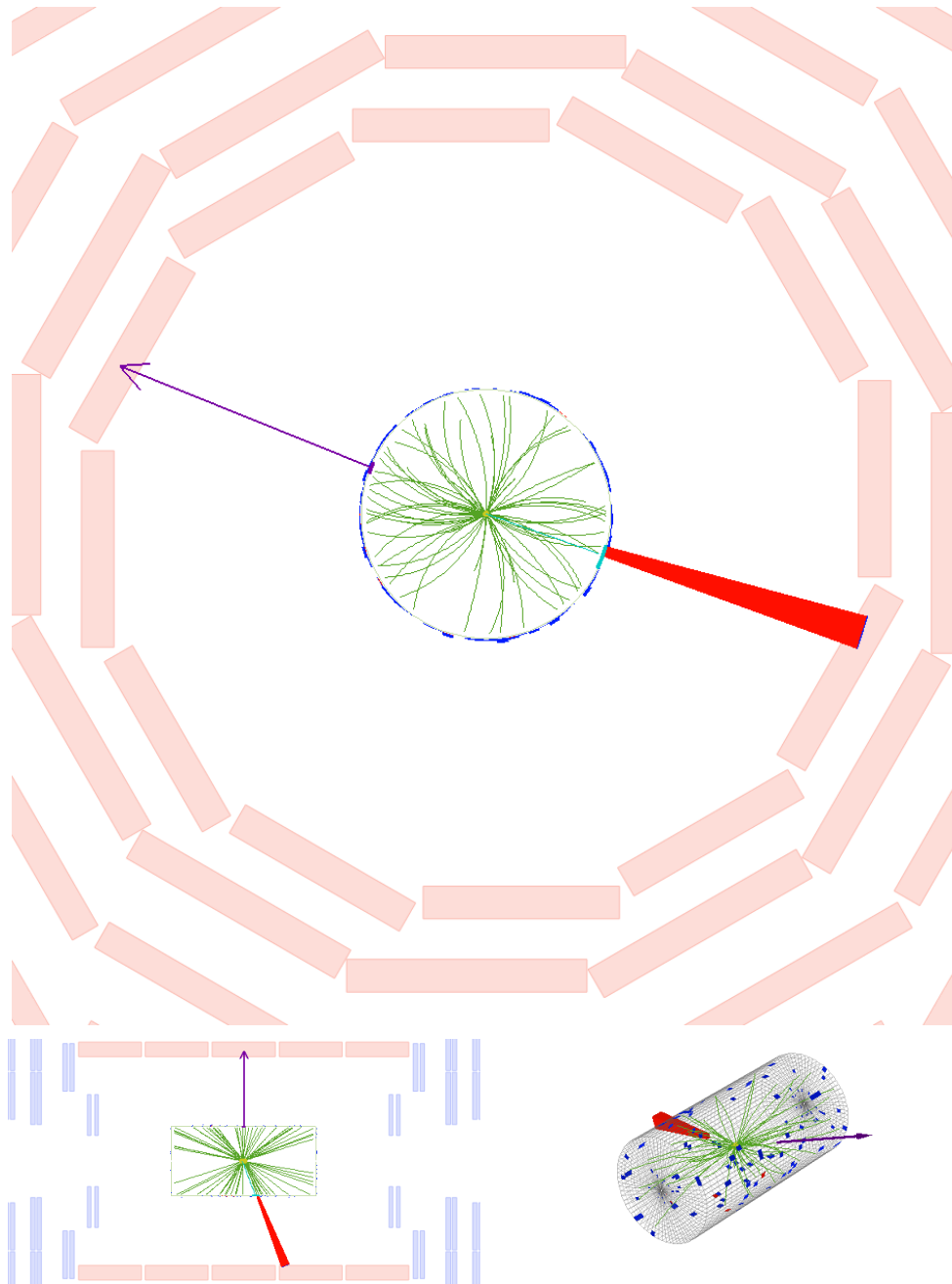


Figure 9.1: Event display showing the event with the highest transverse mass $m_T = 1.95$ GeV in the single-electron channel. The electron is well isolated and has a transverse momentum of $p_T = 998$ GeV. A missing transverse momentum of $E_T^{\text{miss}} = 998$ GeV is present in the event (run 260627, luminosity block 324, event 568831331).

9.3 Impact of the HL-LHC on dark matter searches

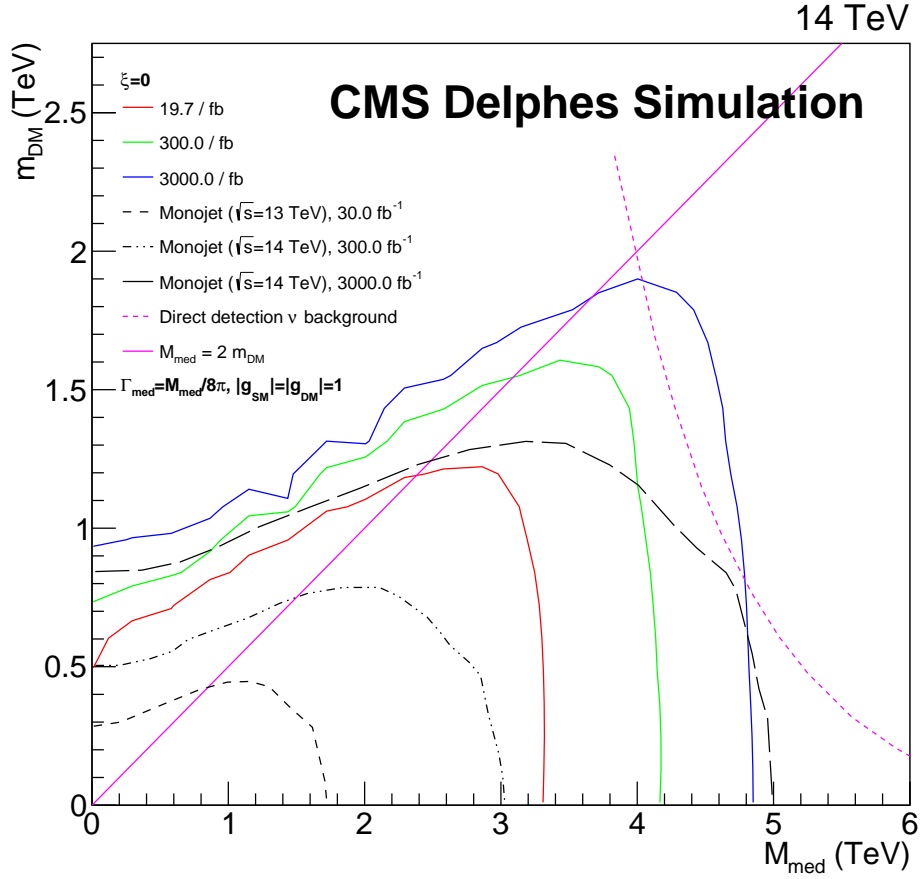


Figure 9.2: Production cross sections for grid pairs of $(M_{\text{med}}, m_{\text{DM}})$ determined from a simplified model for axial-vector coupling for $\xi = 0$. The solid contours indicate projected 95% CL limits from the mono-electron analysis, compared to the projected 90% CL limits from mono-jet analysis results [25] marked as dotted contours. In both analyses the projected cross section limits have been calculated using a DELPHES simulation. The transition region between on- and off-shell mediator production is indicated as a solid magenta line. The neutrino background, also from [25], which is the irreducible background for direct-detection experiments, is shown as a dashed magenta curve.

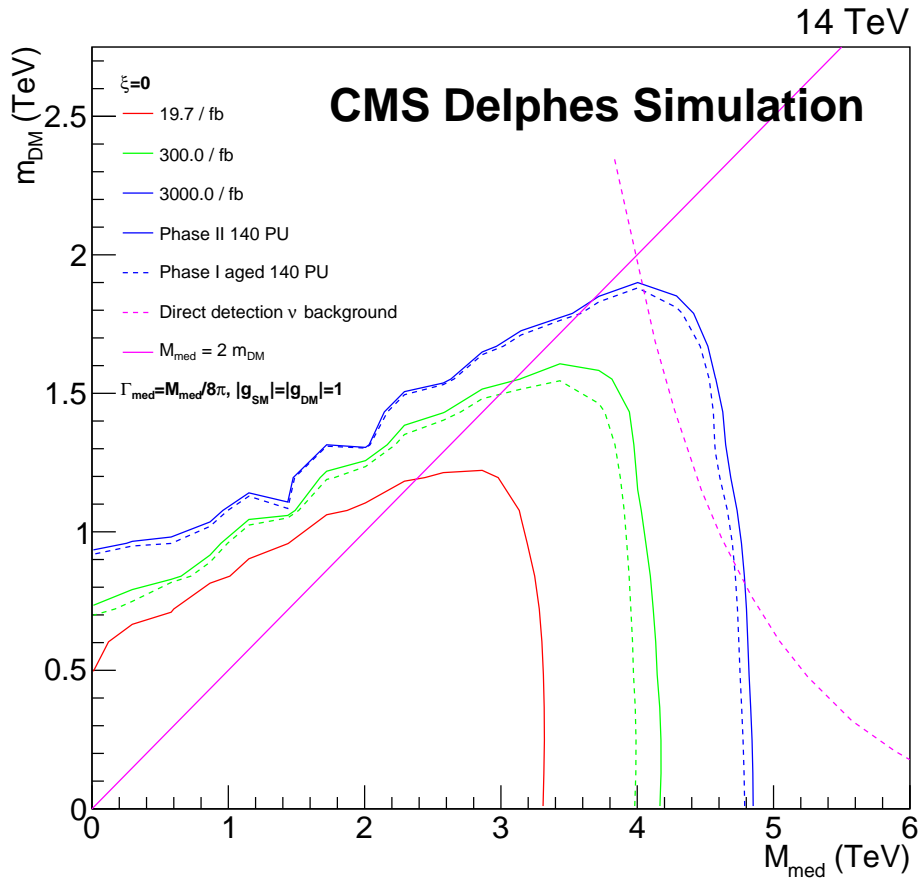


Figure 9.3: Production cross sections for grid pairs of $(M_{\text{med}}, m_{\text{DM}})$ determined from a simplified model for axial-vector coupling for $\xi = 0$. Contours indicate projected 95% CL limits derived by the EFT approach, of which solid contours represent Phase-II conditions and dashed contours indicate Phase-I “aged” conditions. The transition region between on- and off-shell mediator production is indicated as a solid magenta line. The neutrino background, also from [25], which is the irreducible background for direct-detection experiments, is shown as a dashed magenta curve.

Chapter 10

References

- [1] J. Navarro and S. D. White, “The structure of cold dark matter halos”, in *Symposium - International Astronomical Union*, vol. 171, pp. 255–258, Kluwer Academic Publishers Group. 1996.
- [2] J. Brownstein and J. Moffat, “The bullet cluster 1e0657-558 evidence shows modified gravity in the absence of dark matter”, *Monthly Notices of the Royal Astronomical Society* **382** no. 1, (2007) 29–47.
- [3] S. Rudaz and F. Stecker, “Cosmic-ray antiprotons, positrons, and gamma rays from halo dark matter annihilation”, *The Astrophysical Journal* **325** (1988) 16–25.
- [4] K. Garrett and G. Duda, “Dark Matter: A Primer”, *Advances in Astronomy* **2011** (2011) .
- [5] **CMS** Collaboration, V. Khachatryan *et al.*, “Search for physics beyond the standard model in final states with a lepton and missing transverse energy in proton-proton collisions at $\sqrt{s} = 8$ TeV”, *Phys. Rev.* **D91** no. 9, (2015) 092005, arXiv:1408.2745 [hep-ex].
- [6] G. Altarelli, B. Mele, and M. Ruiz-Altaba, “Searching for new heavy vector bosons in $p\bar{p}$ colliders”, *Zeitschrift für Physik C Particles and Fields* **45** no. 1, (1989) 109–121. <http://dx.doi.org/10.1007/BF01556677>.
- [7] **CMS** Collaboration, V. Khachatryan *et al.*, “Search for new resonances decaying via WZ to leptons in proton-proton collisions at $\sqrt{s} = 8$ TeV”, *Phys. Lett.* **B740** (2015) 83–104, arXiv:1407.3476 [hep-ex].
- [8] **CMS** Collaboration, “Search for massive resonances decaying into pairs of boosted W and Z bosons at $\sqrt{s} = 13$ TeV”, *CMS-PAS-EXO-15-002* (2015) . <https://cds.cern.ch/record/2117062>.
- [9] **Particle Data Group** Collaboration, K. A. Olive *et al.*, “Review of Particle Physics”, *Chin. Phys.* **C38** (2014) 090001.
- [10] **Planck** Collaboration, P. A. R. Ade *et al.*, “Planck 2015 results. XIII. Cosmological parameters”, arXiv:1502.01589 [astro-ph.CO].

CHAPTER 10. REFERENCES

- [11] T. Marrodán Undagoitia and L. Rauch, “Dark matter direct-detection experiments”, *J. Phys.* **G43** no. 1, (2016) 013001, arXiv:1509.08767 [physics.ins-det].
- [12] J. Lewin and P. Smith, “Review of mathematics, numerical factors, and corrections for dark matter experiments based on elastic nuclear recoil”, *Astroparticle Physics* **6** no. 1, (1996) 87 – 112.
<http://www.sciencedirect.com/science/article/pii/S0927650596000473>.
- [13] XENON100 Collaboration, E. Aprile *et al.*, “Search for Event Rate Modulation in XENON100 Electronic Recoil Data”, *Phys. Rev. Lett.* **115** no. 9, (2015) 091302, arXiv:1507.07748 [astro-ph.CO].
- [14] PICO Collaboration, C. Amole *et al.*, “Dark Matter Search Results from the PICO-2L C₃F₈ Bubble Chamber”, *Phys. Rev. Lett.* **114** no. 23, (2015) 231302, arXiv:1503.00008 [astro-ph.CO].
- [15] SuperCDMS Collaboration, R. Agnese *et al.*, “New Results from the Search for Low-Mass Weakly Interacting Massive Particles with the CDMS Low Ionization Threshold Experiment”, *Phys. Rev. Lett.* **116** no. 7, (2016) 071301, arXiv:1509.02448 [astro-ph.CO].
- [16] CRESST Collaboration, J. Schieck, “Direct Dark Matter Search with the CRESST-II Experiment”, in *Proceedings, 50th Rencontres de Moriond Electroweak interactions and unified theories*, pp. 445–450. 2015. arXiv:1505.03289 [astro-ph.CO].
<https://inspirehep.net/record/1369959/files/arXiv:1505.03289.pdf>.
- [17] G. Bertone, D. Hooper, and J. Silk, “Particle dark matter: Evidence, candidates and constraints”, *Phys. Rept.* **405** (2005) 279–390, arXiv:hep-ph/0404175 [hep-ph].
- [18] G. Busoni *et al.*, “Recommendations on presenting LHC searches for missing transverse energy signals using simplified *s*-channel models of dark matter”, arXiv:1603.04156 [hep-ex].
- [19] N. F. Bell, Y. Cai, J. B. Dent, R. K. Leane, and T. J. Weiler, “Dark matter at the LHC: Effective field theories and gauge invariance”, *Phys. Rev.* **D92** no. 5, (2015) 053008, arXiv:1503.07874 [hep-ph].
- [20] N. F. Bell, Y. Cai, and R. K. Leane, “Mono-W Dark Matter Signals at the LHC: Simplified Model Analysis”, *JCAP* **1601** no. 01, (2016) 051, arXiv:1512.00476 [hep-ph].
- [21] U. Haisch, F. Kahlhoefer, and T. M. P. Tait, “On Mono-W Signatures in Spin-1 Simplified Models”, arXiv:1603.01267 [hep-ph].
- [22] A. L. Fitzpatrick, W. Haxton, E. Katz, N. Lubbers, and Y. Xu, “The Effective Field Theory of Dark Matter Direct Detection”, *JCAP* **1302** (2013) 004, arXiv:1203.3542 [hep-ph].

- [23] **SuperCDMS** Collaboration, K. Schneck *et al.*, “Dark matter effective field theory scattering in direct detection experiments”, *Phys. Rev.* **D91** no. 9, (2015) 092004, arXiv:1503.03379 [astro-ph.CO].
- [24] P. Harris, V. V. Khoze, M. Spannowsky, and C. Williams, “Constraining Dark Sectors at Colliders: Beyond the Effective Theory Approach”, arXiv:1411.0535 [hep-ph].
- [25] O. Buchmueller, M. J. Dolan, S. A. Malik, and C. McCabe, “Characterising dark matter searches at colliders and direct detection experiments: Vector mediators”, *JHEP* **1501** (2015) 037, arXiv:1407.8257 [hep-ph].
- [26] Y. Bai and T. M. Tait, “Searches with Mono-Leptons”, *Phys.Lett.* **B723** (2013) 384–387, arXiv:1208.4361 [hep-ph].
- [27] W. Bernreuther, P. Gonzalez, and M. Wiebusch, “Pseudoscalar Higgs Boson Decays into W and Z Bosons Revisited”, arXiv:0909.3772 [hep-ph].
- [28] P. J. Fox, R. Harnik, J. Kopp, and Y. Tsai, “Missing Energy Signatures of Dark Matter at the LHC”, *Phys.Rev.* **D85** (2012) 056011, arXiv:1109.4398 [hep-ph].
- [29] V. Ilisie, “Higgs decay”, *Master thesis* (2011).
http://ific.uv.es/lhcpheno/PhDthesis/master_vilisie.pdf.
- [30] O. Buchmueller, M. J. Dolan, and C. McCabe, “Beyond Effective Field Theory for Dark Matter Searches at the LHC”, *JHEP* **1401** (2014) 025, arXiv:1308.6799 [hep-ph].
- [31] J. Abdallah *et al.*, “Simplified Models for Dark Matter and Missing Energy Searches at the LHC”, arXiv:1409.2893 [hep-ph].
- [32] J. Alwall, R. Frederix, S. Frixione, V. Hirschi, F. Maltoni, O. Mattelaer, H. S. Shao, T. Stelzer, P. Torrielli, and M. Zaro, “The automated computation of tree-level and next-to-leading order differential cross sections, and their matching to parton shower simulations”, *JHEP* **07** (2014) 079, arXiv:1405.0301 [hep-ph].
- [33] L. Basso, S. Moretti, and G. M. Pruna, “A Renormalisation Group Equation Study of the Scalar Sector of the Minimal B-L Extension of the Standard Model”, *Phys. Rev.* **D82** (2010) 055018, arXiv:1004.3039 [hep-ph].
- [34] P. J. Fox and C. Williams, “Next-to-Leading Order Predictions for Dark Matter Production at Hadron Colliders”, *Phys. Rev.* **D87** no. 5, (2013) 054030, arXiv:1211.6390 [hep-ph].
- [35] **CMS** Collaboration, “The CMS experiment at the CERN LHC”, *Journal of Instrumentation* **3** no. 08, (2008) S08004.
<http://stacks.iop.org/1748-0221/3/i=08/a=S08004>.
- [36] J. Nielsen, *Fundamentals of LHC Experiments*. 2011. arXiv:1106.2516 [hep-ex].
<https://inspirehep.net/record/913551/files/arXiv:1106.2516.pdf>.

CHAPTER 10. REFERENCES

- [37] E. James, Y. Maravin, M. Mulders, and N. Neumeister, “Muon identification in CMS”, *CERN-CMS-NOTE-2006-010* (2006) .
- [38] **CMS Collaboration** Collaboration, *The CMS muon project: Technical Design Report*. Technical Design Report CMS. CERN, Geneva, 1997.
<https://cds.cern.ch/record/343814>.
- [39] J. Alwall *et al.*, “A Standard format for Les Houches event files”, *Comput. Phys. Commun.* **176** (2007) 300–304, [arXiv:hep-ph/0609017](https://arxiv.org/abs/hep-ph/0609017) [hep-ph].
- [40] P. Nason, “A New method for combining NLO QCD with shower Monte Carlo algorithms”, *JHEP* **11** (2004) 040, [arXiv:hep-ph/0409146](https://arxiv.org/abs/hep-ph/0409146) [hep-ph].
- [41] S. Frixione, P. Nason, and C. Oleari, “Matching NLO QCD computations with Parton Shower simulations: the POWHEG method”, *JHEP* **11** (2007) 070, [arXiv:0709.2092](https://arxiv.org/abs/0709.2092) [hep-ph].
- [42] S. Alioli, P. Nason, C. Oleari, and E. Re, “A general framework for implementing NLO calculations in shower Monte Carlo programs: the POWHEG BOX”, *JHEP* **06** (2010) 043, [arXiv:1002.2581](https://arxiv.org/abs/1002.2581) [hep-ph].
- [43] T. Sjostrand, S. Mrenna, and P. Z. Skands, “A Brief Introduction to PYTHIA 8.1”, *Comput. Phys. Commun.* **178** (2008) 852–867, [arXiv:0710.3820](https://arxiv.org/abs/0710.3820) [hep-ph].
- [44] T. Sjostrand, S. Mrenna, and P. Z. Skands, “PYTHIA 6.4 Physics and Manual”, *JHEP* **05** (2006) 026, [arXiv:hep-ph/0603175](https://arxiv.org/abs/hep-ph/0603175) [hep-ph].
- [45] Y. Gao, A. V. Gritsan, Z. Guo, K. Melnikov, M. Schulze, and N. V. Tran, “Spin determination of single-produced resonances at hadron colliders”, *Phys. Rev.* **D81** (2010) 075022, [arXiv:1001.3396](https://arxiv.org/abs/1001.3396) [hep-ph].
- [46] **Geant4** Collaboration, S. A. et al, “Geant4—a simulation toolkit”, *Nuclear Instruments and Methods in Physics Research Section A: Accelerators, Spectrometers, Detectors and Associated Equipment* **506** no. 3, (2003) 250 – 303.
<http://www.sciencedirect.com/science/article/pii/S0168900203013688>.
- [47] **Delphes** Collaboration, J. Favereau, C. Delaere, P. Demin, A. Giammanco, V. Lemaître, A. Mertens, and M. Selvaggi, “Delphes 3: a modular framework for fast simulation of a generic collider experiment”, *Journal of High Energy Physics* **2014** no. 2, (2014) 1–26.
- [48] **Delphes** Collaboration, S. Oryn, X. Rouby, and V. Lemaitre, “DELPHES, a framework for fast simulation of a generic collider experiment”,
[arXiv:0903.2225](https://arxiv.org/abs/0903.2225) [hep-ph].
- [49] **CMS** Collaboration, “Search for SSM W' production, in the lepton+MET final state at a center-of-mass energy of 13 TeV”, *LHC End-Of-Year Jamboree* (2015) .
<https://cds.cern.ch/record/2114864>.
- [50] **CMS** Collaboration, “MiniAOD Analysis Documentation”, *TWiki page* (2016) .
<https://twiki.cern.ch/twiki/bin/view/CMSPublic/WorkBookMiniAOD2015>.

- [51] H. P. Bretz, M. Brodski, M. Erdmann, R. Fischer, A. Hinzmann, T. Klimkovich, D. Klingebiel, M. Komm, J. Lingemann, G. Müller, T. Münzer, M. Rieger, J. Steggemann, and T. Winchen, “A development environment for visual physics analysis”, *Journal of Instrumentation* **7** no. 08, (2012) T08005. <http://stacks.iop.org/1748-0221/7/i=08/a=T08005>.
- [52] Klaas Padeken, Mark Olschewski, Kerstin Hoepfner, “Cross section calculation for leptonically decaying W at NNLO QCD and NLO electroweak”, *CMS AN-2014-263* (2014). http://cms.cern.ch/iCMS/jsp/db_notes/noteInfo.jsp?cmsnoteid=CMS%20AN-2014/263.
- [53] S. G. Bondarenko and A. A. Sapronov, “NLO EW and QCD proton-proton cross section calculations with mcsanc-v1.01”, *Comput. Phys. Commun.* **184** (2013) 2343–2350, arXiv:1301.3687 [hep-ph].
- [54] R. Gavin, Y. Li, F. Petriello, and S. Quackenbush, “W Physics at the LHC with FEWZ 2.1”, *Comput. Phys. Commun.* **184** (2013) 208–214, arXiv:1201.5896 [hep-ph].
- [55] J. Butterworth *et al.*, “PDF4LHC recommendations for LHC Run II”, *J. Phys.* **G43** (2016) 023001, arXiv:1510.03865 [hep-ph].
- [56] B. Clerbaux *et al.*, “Dielectron resonance search in Run 2 at 13 TeV pp collisions”, *CMS AN-2015-222* (2015). http://cms.cern.ch/iCMS/jsp/db_notes/noteInfo.jsp?cmsnoteid=CMS%20AN-2015/222.
- [57] **CMS Collaboration**, “HEEP Electron ID and isolation”, *HEEPElectronIdentificationRun2 CMS TWiki page*. <https://twiki.cern.ch/twiki/bin/view/CMS/HEEPElectronIdentificationRun2>.
- [58] J. Alcaraz Maestre *et al.*, “Search for new physics, focused on Wprime production, in the single electron/muon plus missing-Et final states using pp collision data at 13 TeV”, http://cms.cern.ch/iCMS/jsp/db_notes/noteInfo.jsp?cmsnoteid=CMS%20AN-2015/226.
- [59] **CMS Collaboration**, F. Beaudette, “The CMS Particle Flow Algorithm”, in *Proceedings, International Conference on Calorimetry for the High Energy Frontier (CHEF 2013)*, pp. 295–304. 2013. arXiv:1401.8155 [hep-ex]. <https://inspirehep.net/record/1279774/files/arXiv:1401.8155.pdf>.
- [60] Gheorghe Lungu, “Missing Transverse Energy at CMS”, *JTERM3 contribution* (2009). http://indico.cern.ch/event/46651/contribution/18/attachments/950879/1%349271/Lungu-Jterm3_MET_011309.pdf.
- [61] **CMS Collaboration**, “Utilities for Accessing Pileup Information for Data”, *PileupJSONFileforData CMS TWiki page*. <https://twiki.cern.ch/twiki/bin/viewauth/CMS/PileupJSONFileforData>.
- [62] **CMS Collaboration**, V. Khachatryan *et al.*, “Search for W’ decaying to tau lepton and neutrino in proton-proton collisions at $\sqrt{s} = 8$ TeV”, *Phys. Lett.* **B755** (2016) 196–216, arXiv:1508.04308 [hep-ex].

CHAPTER 10. REFERENCES

- [63] A. L. Read, “Presentation of search results: the χ^2 technique”, *Journal of Physics G: Nuclear and Particle Physics* **28** no. 10, (2002) 2693. <http://stacks.iop.org/0954-3899/28/i=10/a=313>.
- [64] T. Junk, “Confidence level computation for combining searches with small statistics”, *Nucl. Instrum. Meth.* **A434** (1999) 435–443, arXiv:hep-ex/9902006 [hep-ex].
- [65] D. Abercrombie *et al.*, “Dark Matter Benchmark Models for Early LHC Run-2 Searches: Report of the ATLAS/CMS Dark Matter Forum”, arXiv:1507.00966 [hep-ex].
- [66] H. Acaroglu, “A Study of Simplified Models for Dark Matter Searches in pp Collisions”, *Bachelor thesis* (2015). https://web.physik.rwth-aachen.de/~hebbeker/theses/acaroglu_bachelor.pdf.
- [67] B. Kayser and R. E. Shrock, “Distinguishing between dirac and majorana neutrinos in neutral-current reactions”, *Physics Letters B* **112** no. 2, (1982) 137 – 142. <http://www.sciencedirect.com/science/article/pii/0370269382903148>.
- [68] **HERMES** Collaboration, A. Airapetian *et al.*, “Quark helicity distributions in the nucleon for up, down, and strange quarks from semi-inclusive deep-inelastic scattering”, *Phys. Rev.* **D71** (2005) 012003, arXiv:hep-ex/0407032 [hep-ex].
- [69] **CMS Collaboration** Collaboration, “The CMS phase 2: Technical proposal”, *CERN-LHCC 2014-xyz* (2014).
- [70] **CMS** Collaboration, “Technical proposal for the upgrade of the CMS detector through 2020”, Jun, 2011. <https://cds.cern.ch/record/1355706>.
- [71] M. Olschewski, “Search for new physics in proton-proton collision events with a lepton and missing transverse energy”, *doctoral thesis* (2015). https://web.physik.rwth-aachen.de/~hebbeker/theses/olschewski_phd.pdf.

Eigenständigkeitserklärung

Ich versichere, dass ich die Arbeit selbstständig verfasst und keine anderen als die angegebenen Quellen und Hilfsmittel benutzt sowie Zitate kenntlich gemacht habe.

Aachen, den

VIKTOR KUTZNER